# Theoretical Investigation and Optimization Approach for Triboelectric Nanogenerators

# 摩擦纳米发电机的理论研究与优化方法

A Thesis Submitted to

University of Liverpool

in Partial Fulfillment of the Requirements for

the Degree of Doctor of Philosophy

in the Department of Electrical Engineering and Electronics

2023

By:

**Xiaoping CHEN**

## ABSTRACT

With the rise of the fourth industrial revolution, distributed multifunctional sensor networks are becoming core nodes for exchanging information between intelligent devices and control terminals. To meet the power supply requirements of discrete sensors, self-powered technologies have been developed to fulfil sustainable and environmentally friendly strategies. Recently, triboelectric nanogenerator (TENG) emerged with a much-anticipated presence. Because of its flexible structures, environmental friendliness and high performance at low frequencies, TENG was expected as an alternative to mobile power sources. Nevertheless, TENG suffers from low charge density, poor stability and low energy conversion efficiency, significantly hindering its practical development and applications. To bridge the gap to actual utilization, the theoretical frameworks of TENG need to be further refined. Moreover, it still has plenty of room to find multi-dimensional optimization approaches, such as physical model, mathematical optimization, material engineering and electronic circuit design. In the thesis, I will systematically clarify the controlling and limiting factors that affect TENG output, and optimization methods for improving the performance of TENG from the perspectives of material engineering and circuit modulation.

Chapter 1 provided an overview of TENG including its working mechanism, theoretical frameworks and optimization methods. Meanwhile, challenges and problems that need to be solved subsequently were proposed.

Chapter 2 introduced a quasi-electrostatic three-dimensional (QETD) charge model to refine the theoretical modeling of TENGs. Finite element modeling (FEM) simulations were first provided to reveal the distribution of polarization vector ($P_z$), electric potential ($\boldsymbol{\varphi}$), electric field ($E_z$) and electric displacement ($D_z$). Furthermore, an optimized theoretical framework for contact-separation TENGs was established, and it was validated by different driving and structural variables. Besides, the intrinsic displacement current of TENGs was linked with the conduction current to deduce the output capability. Compared with previous works, this QETD model shows the most consistent trend with experimental results, providing accurate predicts for distinct TENGs' performance.

In chapter 3, the side effect of interfacial electric field was discussed, resulting in the charge recombination. To counter its effects, a MXene/$TiO_2$ hybrid film as an intermediate layer of TENG (MT-TENG) was prepared. The MXene/$TiO_2$ hybrid film could increase the capacitance and provide abundant electron trap sites for charge trapping and blocking. The optimal MT-TENG presents 128 μC/$m^2$ in charge density, 73.78 μW/$cm^3$ and 63.78 μW/g in average power density with an energy conversion efficiency of 34.81%. Under the charge decay model, the MT-TENG with an intermediate layer rapidly reaches a charge dynamic equilibrium with a charge density of 80 μC/$m^2$.

Chapter 4 was devoted to finding the TENG's theoretical boundary by considering the air breakdown effect. The limit equations of TENG's surface charge density were systematically analyzed. As the separation distance increases, the maximum surface

charge density ($\sigma_m$) of TENGs drops and keeps consistent after air breakdown. As for the structure design, thinner dielectric layers with higher relative permittivity are preferred to improve $\sigma_m$. Moreover, the maximized effective energy output ($E_{em}$) and figure of merit (FOM) of TENG were simulated with various structural and material parameters. The TENG with 10 μm silicone rubber shows 2.85 mC/m$^2$ of $\sigma_m$ and 1.12 mJ of $E_{em}$ at 2 cm separation distance.

Chapter 5 concentrated on controlling the electrical output of TENG through an analogue front-end (AFE) circuit to implement an integrated self-powered real-time pedometer system. In this system, a porous TENG was designed as a pressure sensor to generate electrical signals synchronized with users' footsteps. Then, the AFE circuit grabs the output from P-TENG and regulates for triggering with an ultrafast response time of 8 ms. Transferring via Bluetooth, a mobile phone APP would receive the signals and complete step counting in real-time. Ultimately, a mini press-to-spin type electromagnetic generator (EMG) and a supercapacitor guarantee the self-powered and self-sustained operation of the entire pedometer system, including signal generation, transduction, processing and wireless transmission.

In chapter 6 provided conclusions from my work and presented worthwhile work to be done in the future.

## 摘要

随着第四次工业革命的兴起，分布式多功能传感器网络已成为智能设备和控制终端之间交换信息的关键节点。为了满足离散式传感器的供电要求，自驱动技术不断发展，以迎合可持续发展和环境友好的战略需求。最近，摩擦纳米发电机（TENG）顺势而来，由于其结构灵活、环境友好性和低频下具有高性能等特性，有望成为移动电源的替代品。然而，TENG 仍然存在电荷密度低、稳定性差和能量转换效率低的问题，严重阻碍了其实际发展和应用。为了弥合到实际利用的差距，TENG 的理论框架还需要进一步完善，并且有很大的空间从多维度来探索其优化方法，包括物理模型、数学优化、材料工程和电子电路设计。在本论文中，我将系统地阐明 TENG 输出的控制和限制因素，以及从材料工程和电路调制的角度来优化 TENG 的输出性能的优化方法。

第一章对 TENG 进行概述介绍，包括其工作机制、理论框架和优化方法。同时，提出了亟待解决的挑战和问题。

第二章介绍了完善 TENG 理论框架的的准静电三维（QETD）电荷模型。有限元建模（FEM）计算结果首次揭示了极化矢量（$P_z$），电势（$\boldsymbol{\varphi}$），电场（$E_z$）和电位移矢量（$D_z$）的分布情况。随后，建立了一个优化的接触分离式 TENG 的理论模型，并以此验证了在不同驱动和结构变量下的实用性。此外，TENG 的本征位移电流与传导电流形成闭环推导出输出性能。与已报道的理论模型相比，QETD 模型显示出与实验结果最相近的趋势，可对 TENG 的输出性能进行预测。

第三章讨论了 TENG 界面电场的负效应，会导致 TENG 摩擦电荷复合。为了消除其影响，制备了一种 MXene/$TiO_2$ 复合膜作为 TENG 的中间层（MT-TENG）。

MXene/$TiO_2$ 复合膜可以增加电容，并提供丰富的电子陷阱对电荷进行捕获和阻挡。优化后的 MT-TENG 的电荷密度达到 128μC/$m^2$，平均功率密度达到 73.78μW/$cm^3$ 和 63.78μW/g，能量转换效率达到 34.81%。基于电荷衰减模型，带有中间层的 MT-TENG 迅速达到电荷动态平衡，电荷密度维持在 80 μC/$m^2$。

第四章试图基于空气击穿效应找到 TENG 的理论边界。通过系统地分析 TENG 的表面电荷密度的限制方程，发现随着分离距离的增加，TENG 的最大表面电荷密度（$\sigma_m$）不断减小，但在空气击穿后保持稳定。在结构设计方面，为提高$\sigma_m$，最好选择相对介电常数较高的更薄的电介质层。此外，模拟了 TENG 在不同的结构参数和材料参数下的最大有效能量输出（$E_{em}$）和品质因素（FOM）。根据仿真结果，带有 10 微米硅橡胶所制的 TENG 在 2 厘米的分离距离下展示出 2.85 mC/$m^2$ 的最大表面电荷密度和 1.12 mJ 的最大有效能量输出。

第五章致力于通过模拟前端（AFE）电路调控 TENG 的电输出，实现了集成化的自供电实时计步器系统。在这个系统中，设计了一个多孔的 TENG 作为压力传感器，产生与用户行走同步的电信号。然后，AFE 电路抓取 P-TENG 的输出信号，并对其进行调控和触发，响应时间为 8 毫秒。通过蓝牙传输，手机 APP 将接收出发信号并完成实时计步。最后，通过一个微型压转式电磁发生器（EMG）和超级电容器，保证了整个计步器系统的自供电和持续性运行，包括信号的产生、转换、处理和无线传输。

在第六章中，我对所有工作进行总结，并提出了未来值得深究的工作。

## ACKNOWLEDGEMENTS

As time flies, my Ph.D. life comes to the end. This thesis becomes the culmination of my long and arduous education journey. By means of the thesis, I want to express my gratitude for everything that happened and for everyone I have met in these four years. My deepest gratitude goes first and foremost to my mentor team. As my principal supervisor, Dr. Yina Liu provided me with a valuable full-award Ph.D. offer and an advanced laboratory platform, allowing me to carry out my research smoothly. Prof. Zhen Wen led me from a newcomer and provided me access to academic research. Dr. Chun Zhao and Dr. Kai Hoettges are my co-supervisors, and they always offered me feedbacks during my study. Prof. Xuhui Sun and Prof. Cezhou Zhao always gave me wise advice and trained my scientific mind and research spirit. I appreciate their constant encouragement and guidance in my life and studies. It’s a great honor to own such a strong team of mentors, so I have learned to multitask multiple complex projects and executive based on priority. This also made me possess the strong mental quality and efficient action force to fight the odds.

In XJTLU, I also met a group of friendly colleagues. I would like to thank my groupmates: Tianshi Zhao, Qihan Liu, Li Yin, Xinkai Xie, Yixin Cao, Qinan Wang, Haibin Wang, Lingjie Xie, Bohan Lu, Hao Lei and Junyan Li. We always maintain a positive and effortful research environment and help each other. Also, I would express my appreciation to other colleagues in IR520: Yi Sun, Ye Liang, Yuhao Zhu, Ang Li, Weisheng Wang, Pingyu Cao, Fan Li, Yuanlei Zhang, Xianwei Geng and Chao Wang.

Gathering and doing sports with them offer me plenty of inspiration and happiness. I will always remember the pleasant time working and living with them.

Fortunately, I have to thank some of my close friends. Ms. Jingya Liu has always been by my side and encouraged me. I don't feel alone anymore since we can grow up and move forward together, and face the unknowns and challenges of life side by side. Also, I must express my sincere thanks to Ms. Jiajia Gao, Ms. Jingjing Zhang, Ms. Chengmurong Ding and Mr. Zichu Qin. They have always supported me unconditionally and cheered me up when I doubted myself. Without their company, my research life would be full of bewilderment and frustration.

Last but not least, my cordial thanks go to my family members for their consistent education and support. My parents' strict discipline has cultivated me to be a self-motivated and independent person. I will benefit from it in my whole life.

As a late-bloomer, I have once been negated, underestimated and unrecognized. However, I am happy that my passion never fades, and I am continuously proving myself to win everyone's approval. As a final reflection on my Ph.D. career, and a vision for the future, I would like to end the thesis with a quote: "The sun himself is weak when he first rises, and gathers strength as the day gets on."

Xiaoping Chen

May, 2023

## LIST OF CONTENTS

## LIST OF FIGURES

## LIST OF TABLES

# CHAPTER 1 Introduction

## 1.1 Overview

The fourth industrial revolution brings blooming cutting-edge technologies, such as the Internet of Things, big data, robotics and artificial intelligence.[1] Production methods are gradually shifting from mass manufacturing to mass customisation through "intelligent connections" between factories and consumers.[2] Smart manufacturing based on wireless interconnection technology relies closely on distributed, multifunctional sensors. How to power the large number of discrete sensors has become a bottleneck in their development. The convenience of wireless sensor networks would be compromised by the transmission of power via cables, and inadequate power conversion in the transmission process would result in wasted energy. As for energy storage devices, such as batteries, need frequent replacement and maintenance problems, and the end-of-life of batteries will also put pressure on the environment. Therefore, finding a sustainable self-powered energy supply has become an effective strategy to meet the demand for mobility in smart manufacturing.

Since 2012, triboelectric nanogenerator (TENG) has attracted much attention as a new energy conversion device based on the coupling effect of contact triboelectrification and electrostatic induction.[3-4] With its advantages of wide selection of materials, flexible structure and low cost, TENGs are widely used to collect mechanical energy such as human motion, wind and ocean energy and convert into electrical energy.[5-7] In addition, as a self-powered sensor, TENGs show great potential in the field of big health

and human-machine interface.[8-10]

The working modes of TENGs can be divided into four categories, including vertical contact-separation mode, lateral sliding mode, single-electrode mode and freestanding triboelectric-layer mode, as demonstrated in **Figure 1.1**.[11] At the microscopic level, the essence of TENG can be described as charge generation, transfer and induction. Concerning the charge generation, the mechanism of triboelectrification has been always discussed, and explanations consisting of electron transfer, ion transfer, and material transfer were given.[12-14] The mainstream statement is electron cloud potential model.[15] Electron cloud potential model tells us when two materials contact, the overlapping electron clouds of two atoms would form, and reduce the energy barrier between two materials for electron transfer. As two materials separate, part of electrons transfer back, but the remain electrons constitute the triboelectric charges.[16]

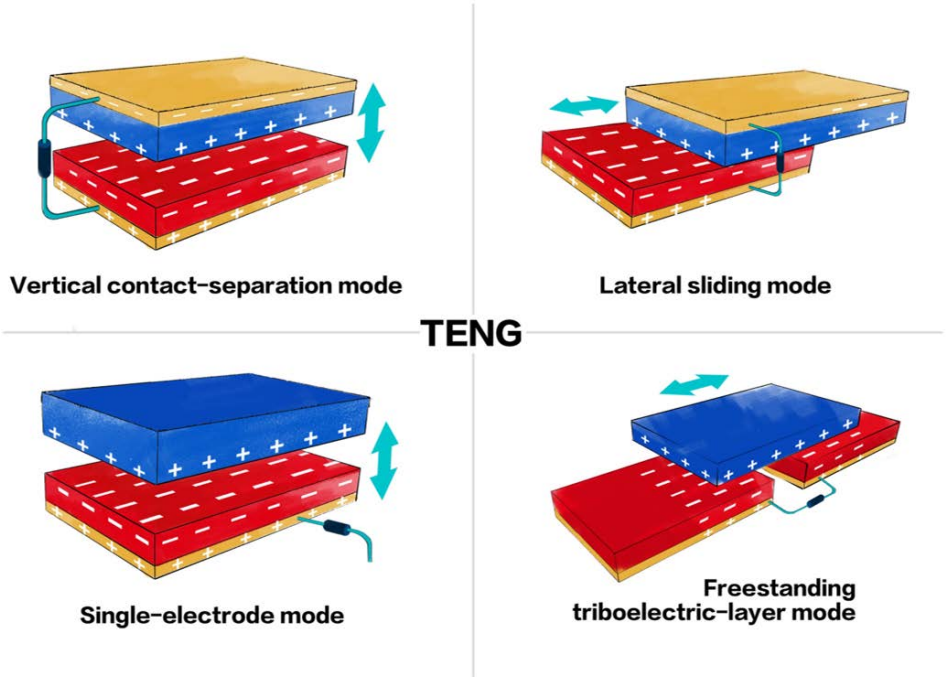


**Figure 1.1** Four working modes of TENGs.

## 1.2 Theoretical Investigation of TENG

### 1.2.1 Theory from Maxwell's Equations

The theoretical origin of TENG is derived from Maxwell's equations. Unlike electromagnetic generators driving by Lorentz force, the driving force for TENG to convert mechanical energy to electrical energy is Maxwell's displacement current. In 2017, Prof. Zhonglin Wang expanded the Maxwell's equations with an additional term $P_s$, called as Wang term:[17]

$$D = \varepsilon_0 E + P + P_s \tag{1-1}$$

$$J_D = \frac{\partial D}{\partial t} = \varepsilon \frac{\partial E}{\partial t} + \frac{\partial P_s}{\partial t} \tag{1-2}$$

Wang term told us the dielectric surface polarization could be produced by strain effect, such as piezoelectric effect and contact electrification, but not just electric field induction. Thus, Maxwell's equations were rewritten as:[17]

$$\varepsilon \nabla \cdot E = \rho - \nabla \cdot P_s \tag{1-3}$$

$$\nabla \cdot B = 0 \tag{1-4}$$

$$\nabla \times E = -\frac{\partial B}{\partial t} \tag{1-5}$$

$$\nabla \times H = J + \varepsilon \frac{\partial E}{\partial t} + \frac{\partial P_s}{\partial t} \tag{1-6}$$

The expended Maxwell's equations became the first principle theory of TENG. Meanwhile, TENG is regarded as another application of Maxwell's equations in addition to electromagnetic waves. According to four working modes, theoretical models were constructed to investigate and quantify the output characteristics of

TENGs, including formal physical model and equivalent electrical circuit model, as demonstrated in **Figure 1.2**.

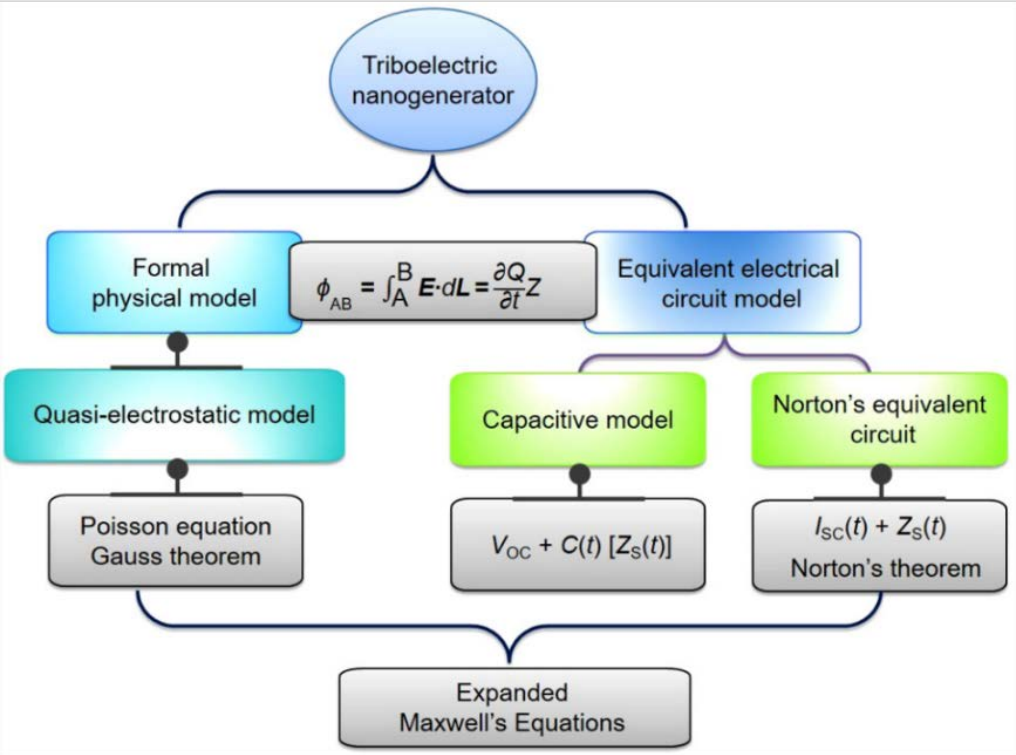


**Figure 1.2** Formal physical model and equivalent electrical circuit model for TENG.[18]

### 1.2.2 Formal Physical Model for TENG

After contact triboelectrification, triboelectric charges are produced on the surface of dielectric layers, leading to the electrostatic field. Once TENG is in the low-frequency movement, it enters the quasi-electrostatic state, which means the induced electric field would change. To quantify the varying electric field, Dr. Shao proposed the three-dimensional (3D) mathematical modeling for TENGs, as illustrated in **Figure 1.3**.[19-21]

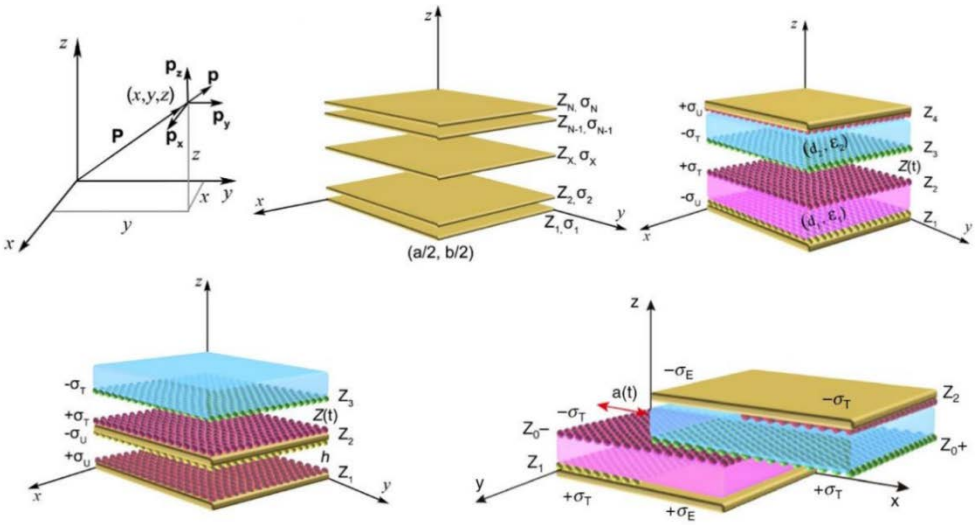


**Figure 1.3** 3D mathematical modeling for TENGs.[19-21]

The Maxwell–Poisson equation expresses:[18]

$$\nabla \cdot D = \rho(r) \tag{1-7}$$

in which $\rho$ is the charge density consisting of induced charges on electrodes and triboelectric charges on the dielectric layers. Assuming material $\alpha$ works as the dielectric, equation (1-7) can be figure out by integral as:

$$\emptyset(r) = \frac{1}{4\pi\varepsilon_\alpha}\int \frac{\rho(r')}{|r-r'|}dV \tag{1-8}$$

where $\varepsilon_\alpha$ means the relative permittivity of material $\alpha$. To solve this, each model is set into a Cartesian coordinate system (**Figure 1.3**). All the charged planes are centered at $(\mathrm{x},\mathrm{y}) = (0,0)$ with the position of $\mathrm{z}_i$. Then, for any point $(\mathrm{x},\mathrm{y},\mathrm{z})$ in this coordinate system, its electrical potential can be deduced as:[18]

$$\emptyset(x,y,z) = \sum_{i=1}^{N}\frac{\sigma_i}{4\pi\varepsilon_{(r)}}\int_{-\frac{a}{2}}^{\frac{a}{2}}\int_{-\frac{b}{2}}^{\frac{b}{2}}\frac{dx'dy'}{\sqrt{(x-x')^2+(y-y')^2+(z-\mathrm{z}_i')^2}} \tag{1-9}$$

Thus, the electric field of arbitrary point $(\mathrm{x},\mathrm{y},\mathrm{z})$ is given as:[18]

$$\mathrm{E}(x,y,z) = -\nabla\emptyset$$

$$= \sum_{i=1}^{N}\frac{\sigma_i}{4\pi\varepsilon_{(r)}}\int_{-\frac{a}{2}}^{\frac{a}{2}}\int_{-\frac{b}{2}}^{\frac{b}{2}}\frac{dx'dy'}{(x-x')^2+(y-y')^2+(z-\mathrm{z}_i')^2}\frac{(x-x',y-y',z-\mathrm{z}_i')}{\sqrt{(x-x')^2+(y-y')^2+(z-\mathrm{z}_i')^2}} \tag{1-10}$$

For vertical contact-separation mode and single mode TENGs, their movements follow $z$ axis. Due to the central symmetry around $(x, y) = (0,0)$, the components of the electric field on the x and y axes could cancel out. Then, the electric field in $z$ axis can be derived as:

$$E(x, y, z) = \sum_{i=1}^{N} \frac{\sigma_i (z - z_i')}{4\pi\varepsilon_{(r)}} \int_{-\frac{a}{2}}^{\frac{a}{2}} \int_{-\frac{b}{2}}^{\frac{b}{2}} \frac{dx'dy'}{[(x-x')^2+(y-y')^2+(z-z_i')^2]^{\frac{3}{2}}} \quad (1\text{-}11)$$

And this is the basis of distance-dependent electric field (DDEF) model, where the electric field is described as distance-varying.[22] As shown in **Figure 1.4**, DDEF model emphasizes the quantifiable electric field by considering discrete charges on the finite irregularly charged plane.[23]

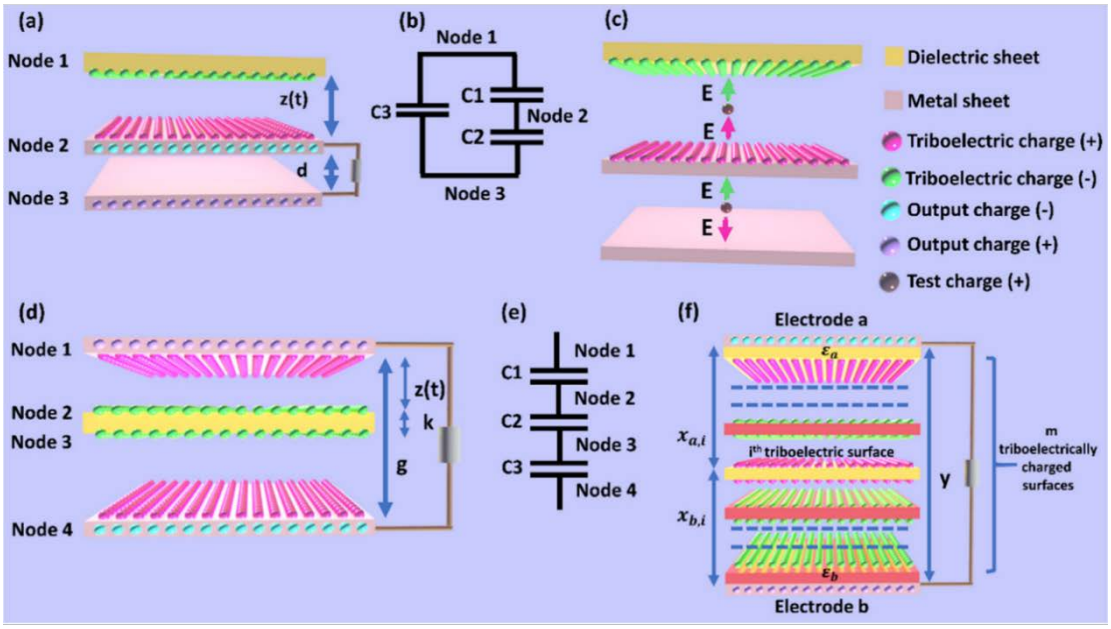


**Figure 1.4** Distance-dependent electric field (DDEF) model for TENGs. [23]

### 1.2.3 Equivalent Electrical Circuit Model for TENG

From the perspective of a circuit, the electrical potential difference of TENG includes polarized triboelectric charges and their contribution to the voltage ($V_{oc(x)}$), and the

already transferred charges $Q$.[22] The governing function of TENG can be written as:

$$V = -\frac{Q}{C(x)} + V_{oc(x)} \tag{1-12}$$

in which C represents the capacitance between the two electrodes, including the capacitance of device parts and the air gap. TENG here is treated as the parallel-plate capacitor model, and the electric field of the charged planes is expressed by Gauss law.[24] For different working modes of TENG, the capacitance would be calculated with various structural conditions.[25-26] The first-order lumped-parameter equivalent circuit model of TENG can be viewed as series connection of a voltage source and a capacitor, as schematically illustrated in **Figure 1.5**a.[27] Under the short-circuit condition, the electrical potential difference $V$ equals to 0. Then, the relationship between transferred charges $Q$, capacitor $C$ and open-circuit voltage $V_{oc}$ can be given by:

$$Q = C(x) \cdot V_{oc(x)} \tag{1-13}$$

Afterward, Dr. Zi et al. proposed a universal edge approximation based equivalent capacitance (EDAEC) method.[28] EDAEC methods consider the edge effect of the capacitance, including contact-separation movements and sliding movements, which make correction to the parallel-plate capacitor model.

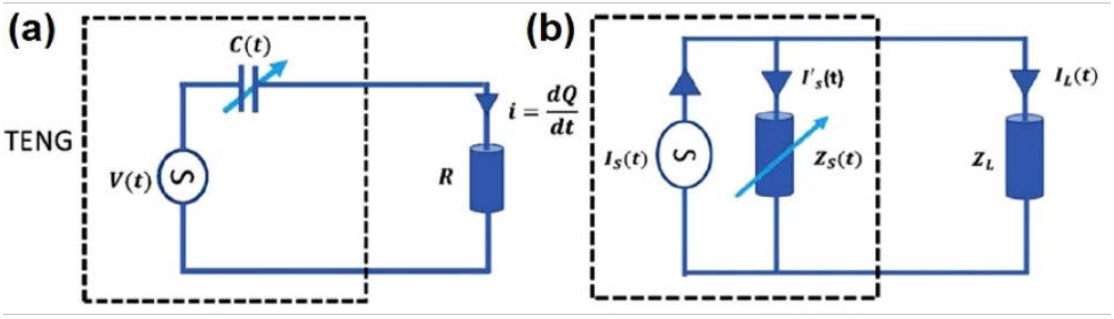


**Figure 1.5** Equivalent Electrical Circuit Model for TENGs. (a) Capacitor model; (b)

Norton's equivalent circuit model.[29]

In few cases, TENG is treated as a time-variant source $I_{S(t)}$ in parallel with the TENG internal impedance $Z_{S(t)}$, as **Figure 1.5**b presented, according to the Norton's theorem for a linear-two-terminal system.[29]

### 1.2.4 Relationship between Physical Model and Circuit Model

Maxwell's displacement current is the intrinsic essence of TENG, while the external manifestation of TENG is conduction current, as displayed in **Figure 1.6**.[30] In the circuit involving a TENG and a load, the displacement current and conduction current constitute a complete loop. Without leakage current, the displacement current is equal to the conduction current. So the connection between TENG's physical model and circuit model can be presented by:[30]

$$\emptyset_{AB} = \int_A^B E \cdot dL = \frac{\partial Q}{\partial t} R \tag{1-14}$$

Namely, from the view of current, the equation can be derived as:[31]

$$I_D = \int J_D \cdot ds = \int \frac{\partial D}{\partial t} \cdot ds = \frac{\partial}{\partial t} \int (\nabla \cdot D)\, dr = \frac{\partial}{\partial t} \int \rho dr = \frac{\partial Q}{\partial t} \tag{1-15}$$

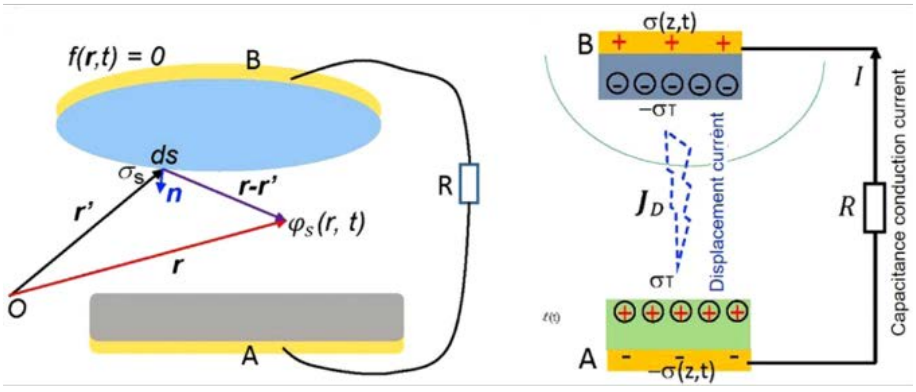


**Figure 1.6** A TENG displayed by displacement current and the conduction current.[30]

The theoretical investigations of TENG help us understand the working principle and physical mechanism of TENG.[32] To achieve high-efficient utilization of TENG, output

characteristics and relevant influencing parameters need be considered. Theoretical models of various practical TENG devices should be established to provide predictions for the output performance and give guidance for optimization.

## 1.3 Optimization Approaches for TENG

### 1.3.1 Methods of Surface Charge Density Enhancement

Energy output is a key indicator of energy converter, and the energy output of TENG is proportional to the square of its surface charge density after contact triboelectrification.[33] Methods of improving the surface charge density of TENG have been well studied for decades in engineering area.[34] The optimized methods include: selecting two triboelectric materials in a larger electronegativity range[35], chemically modifying the surface of the triboelectric material[36-37], designing the surface microstructure to increase the effective contact area[38], adding a charge trapping-blocking layer for charge regulation[39-40], using external techniques such as ion injection, corona methods, charge excitation[41-43], and subjecting TENG to vacuum or high breakdown atmospheres[44-45] etc.

**Figure 1.7** gives some typical examples. Hao et al. first proposed the idea of building an intermediate functional layer between the triboelectric layer and the electrode layer in 2016 (**Figure 1.7**a).[46] Through building a polystyrene composite carbon nanotube (PS+CNT) charge transport layer and a polystyrene (PS) charge storage layer between the triboelectric layer and the Al electrode layer, the surface charge density was increased by 11.2 times.[46] Sihong Wang et al. achieved a surface charge density of 630

μC/m$^2$ by using ion injection to enable the fluorinated ethylene propylene copolymer (FEP) surface to attach a saturated negative charge prior to contact-separation movement (**Figure 1.7**b).[41] Jie Wang's team achieved a maximum surface charge density of 1250 μC/m$^2$ by repeated charge accumulation of polyvinyl chloride (PVC) and copper (Cu) under vacuum conditions (5 x 10$^{-5}$ Pa) (**Figure 1.7**c).[45] Chenguo Hu's team used polyvinylidene fluoride composite film (PZT-PVDF) doped by high dielectric constant lead zirconate titanate (ZTO) as triboelectric layer, and prepared carbon silicone as soft contact electrode. Self-saturated polarization of PZT-PVDF triboelectric layer were achieved by charge excitation circuit, creating the highest record of surface charge density of 3.53 mC/m$^2$ (**Figure 1.7**d).[47]

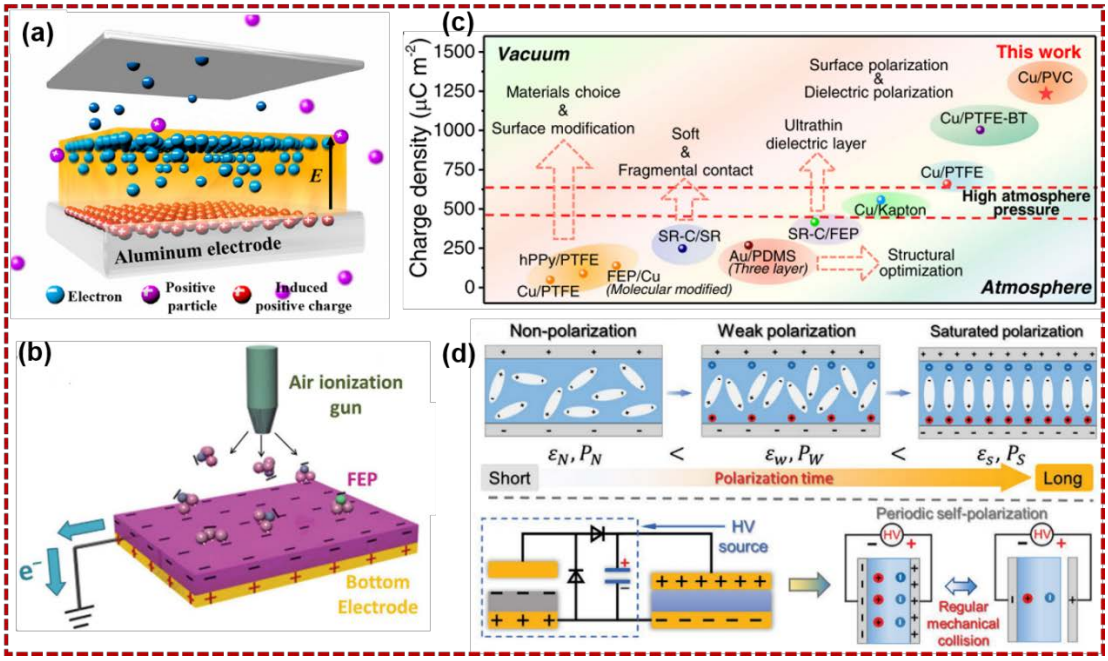


**Figure 1.7** Methods for enhancing the surface charge density of TENG. (a) Adding charge trapping-blocking layer.[46] (b) Ion injection for saturated charge density.[41] (c) Creating vacuum environment.[45] (d) Self-polarization effect by charge-excitation strategy.[47]

### 1.3.2 Theoretical Boundary for TENG

By means of engineering approaches, the surface charge density of TENG has indeed increased by orders of magnitude. Meanwhile, this begs the question: what is the theoretical boundary of TENG's surface charge density? Is there any limiting factors for continuous improvement of TENG's output?

In order to quantitatively evaluate the theoretical limit of TENG, Zhonglin Wang's team proposed the first method to calculate the maximum energy output in 2015. The maximum energy output can be obtained by measuring the voltage-transfer charge V-Q curve of TENG with an infinite resistance load. And the energy output is the integral area of the closing curve of V-Q, as demonstrated in **Figure 1.8**a.[48] In 2019, taking into account the breakdown effect which affects the effective maximum energy output, Yunlong Zi's team further divided the breakdown region and the non-breakdown region on the original V-Q curve of the maximum energy output. The non-breakdown region can be determined by designing experiments, and proposed a standardized experimental method to evaluate the maximum effective energy output of TENG (**Figure 1.8**b).[49] In the theoretical study of triboelectric charge density, Sihong Wang's team proposed that the extremely high electrostatic field formed between the electrode and the triboelectric layer, which greatly increases the possibility of air breakdown. Based on the air breakdown effect, the charge density limitation equations were obtained (**Figure 1.8**c).[50] Jie Wang's team deduced the limitation equation for the charge density based on Paschen's law and the comparison of the voltage drop across the air gap in the TENG.

Through the mathematical derivation of the limitation equation, the influence of the thickness of the dielectric layer ($d$) and the separation distance ($x$) on the maximum surface charge density ($\sigma_m$) was systematically and accurately analyzed. The quantitative relationships between $\sigma_m$ and $d$ and $x$ were obtained, and the theoretical boundary limitation of the surface charge density is derived as 1090 μC $m^{-2}$ by 6 μm Kapton film (**Figure 1.8**d).[51]

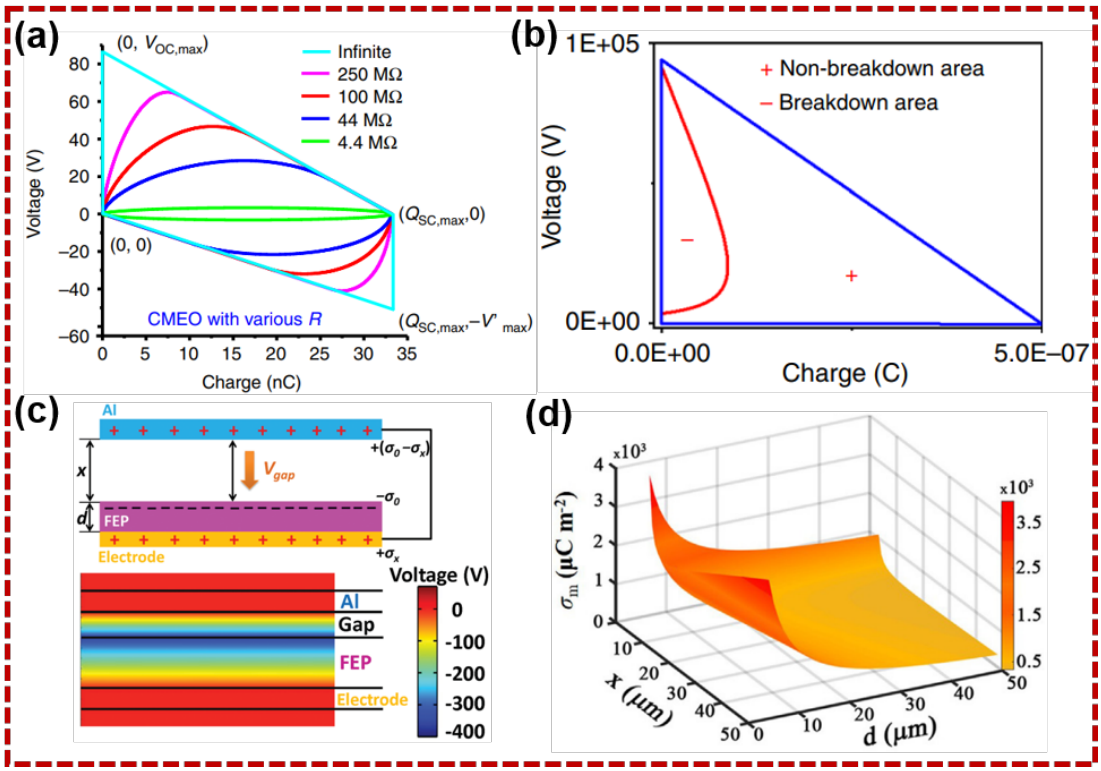


**Figure 1.8** Theoretical limitation assessment of TENG output. (a) Calculation of the maximum energy output V-Q curve.[48] (b) Delineation of breakdown and non-breakdown regions.[49] (c) Maximum surface charge density based on avalanche breakdown theory.[50] (d) Analysis of the effect of dielectric layer thickness and separation distance on the maximum charge density. [51]

## 1.4 Thesis Contribution

Through investigating the previous research, TENG, another branch of Maxwell's

equations, shows great potential to be an emerging energy converter facing technological revolution. However, TENG still suffers from low triboelectric charge density and poor stability. And its high-voltage, low-current output characteristics are difficult to utilize directly, which becomes a large gap in practical applications. To solve as-mentioned problems, this thesis starts with the theoretical model of TENG, clarifying the controlling equations and quantitative mathematical relationships that affect TENG's output. Afterwards, from a materials engineering perspective, TENG's charges are regulated by adding an intermediate layer to reduce the charge decay. Furthermore, the theoretical boundary of TENG's surface charge density was answered in accordance with air breakdown, which reveals what is the maximum value and how to obtain the maximized output. To address TENG's high-voltage and low-current output characteristics, electronic circuit design was combined to regulate its electrical signal, implementing an integrated self-powered real-time pedometer system. The specific works undertaken in this thesis are described below:

Chapter 2 introduces a formal physical framework of TENG based on quasi-electrostatic three-dimensional (QETD) charge model to understand the intrinsic mechanism of TENG. The electric field produced by a finite charged plan was examined with the finite element modelling (FEM) calculation. The results showed the electric field would vary with the separation distance, and electric field lines form closed loops between two electrodes but not vertically. As TENG is in low-frequency movement, it enters a quasi-electrostatic state. Under this state, the distance-varying

electric field was constructed by modelling a three-dimensional spatial charge model. Furthermore, an optimized theoretical framework for contact-separation TENG was established and validated by different driving and structural variables. Besides, the intrinsic displacement current of TENG was linked with its conduction current to deduce the output capability. This QETD model shows the most consistent trend with experimental results, providing accurate predicts for distinct TENGs' performance.

Chapter 3 proposes a MXene/$TiO_2$ hybrid film through partial oxidation of MXene in a contact-separate mode TENG (MT-TENG) as an intermediate layer between negative tribo-material and bottom electrode. It demonstrates the electric outputs of 128 $\mu C/m^2$ in charge density, 73.78 $\mu W/cm^3$ and 63.78 $\mu W/g$ in average power density with an energy conversion efficiency of 34.81%. The surface terminals in MXene nanosheets and the oxygen vacancies in $TiO_2$ nanoparticles provide abundant electron trap sites. Moreover, the energy band bending resulting from the polarization effect of the hybrid film could further hinder the free electrons' drift to the bottom electrode, and consequently prevent the charge recombination. With the synergetic effect of electron storage and polarization, the MT-TENG with an intermediate layer rapidly reaches a charge dynamic equilibrium with a charge density of 80 $\mu C/m^2$. It is expected to provide new insights into material science and structure design from the perspective of charge regulation to improve the output performance of TENGs.

Chapter 4 develops the mathematical derivations to derive the theoretical boundary under the air breakdown restriction for contact-separation mode TENGs. Through the

optimization of limitation equations, mathematical relations were deduced between the output evaluation metrics and TENGs' design, including the structural and material factors. In addition, methodologies for output performance enhancement were proposed. An optimized model possessing 10 μm silicone rubber as the dielectric layer exhibits 2.85 $mC/m^2$ in surface charge density and 1.12 mJ in energy output under 2 cm separation distance. This chapter provides systematical analysis and comprehensive predicts for the theoretical boundary of TENGs' capability, which gives guidance on the design and optimization for high-performance TENGs.

Chapter 5 demonstrates an integrated self-powered real-time pedometer system. The highly integrated system contains a porous triboelectric nanogenerator (P-TENG), a data acquisition and processing (DAQP) module and a mobile phone APP. The P-TENG works as a pressure sensor that generates electrical signals synchronized with users' footsteps. Combining it with the analogue front-end (AFE) circuit yields an ultrafast response time of 8 ms. Moreover, a mini press-to-spin type electromagnetic generator (EMG) and a supercapacitor enable the self-powered and self-sustained operation of the entire pedometer system. This chapter implements the regulation of TENG signals by electronic circuit design and proposes a highly integrated system. The improved reliability and practicality provide more possibilities for wearable self-powered electronic devices.

Chapter 6 summarizes the conclusions of all works and provides perspectives for future studies.

# CHAPTER 2 A Quasi-electrostatic Three-dimensional Charge Model

## 2.1 Background

Maxwell's equations are regarded as a great innovation in physics, which provide a theoretical basis for the conversion of mechanical energy into electrical energy.[52] In 2012, triboelectric nanogenerator (TENG) was invented based on Maxwell's displacement current.[17, 53] The structural design is typically dielectric sandwiched by two electrodes, and the output performance of TENGs has been discussed with the material, geometry, motion and environment parameters.[3-4] For decades, TENG has become the energy harvesting bloomer in various fields, such as wearable electronics, blue energy, self-powered sensors, etc.[2, 32, 54-55]

The working principle of TENG is the coupling effect of contact electrification and electrostatic induction.[16, 56] The essence is the generation, transfer and induction of charges, which belongs to classical electrodynamics.[18] Researchers tried to establish theoretical models for TENG to forecast the output behaviors of TENG, which can be classified into two aspects. The first is the parallel plate capacitor (CA) model proposed in 2013, which is the most used model.[24] CA model treats TENGs as a combination of capacitor and power source in the equivalent electrical circuit.[27] The charged layers in TENG are regarded as infinitely large, uniformly charged plates. The electric field is therefore constant with distance and perpendicular to the charged planes according to Gauss's law. The other is TENG's quasi-electrostatic model, put forward in 2017.[22] A distance-dependent electric field (DDEF) concept was introduced by considering the

charges on the finite charged plane to construct a three-dimensional space-charge model.[23] After that, the Gaussian surface was redefined according to the DDEF model, and the mechanism of Maxwell's displacement current ($I_D$) generation was further discussed.[31] In the DDEF model, the electric field components on the x and y axis can cancel each other in z axis due to the symmetry of the plane, but the electric field components on the z axis are non-cancellable, which causes the electric fields at the same height above the plane to be unequal. Based on this phenomenon, if only the electric field on the z axis rather than entire plane is considered, the accuracy of TENG's theoretical model would be reduced. Therefore, it is important to dig deeper into the working principle and behavioural mechanism of TENG, and establish a more accurate theoretical framework for TENG that meets the conditions of classical physics.

This work aims to develop a theoretical framework for TENG based on a quasi-electrostatic three-dimensional (QETD) charge model. Through finite element modeling (FEM) calculation of TENG, the distribution conditions of the polarization vector ($P_z$), electric potential ($\boldsymbol{\varphi}$), electric field ($E_z$) and electric displacement ($D_z$) were presented. Then, the physical model of TENG based on Maxwell's equations was reconstructed by optimizing the charge model of the finite charged plane. TENG's intrinsic output characteristics and external power expenditure were eventually linked to connect the formal physical model and the equivalent circuit. The variation pattern of the output performance of TENG with each parameter variable was quantified, providing prediction and guidance for the development and utilization of TENG.

## 2.2 Experiments and Methods

Some parameters for device designs and experimental schemes were illustrated in **Table 2.1**.

**Table 2.1** Parameters for device designs and experimental schemes

| **Parameter** | **Value** |
|---|---|
| Relative permittivity of the negative triboelectric layer $\varepsilon_{r1}$ | 2 |
| Length of the triboelectric layer $L$ | 20/30/50 mm |
| Width of the triboelectric layer $W$ | 20/30/50 mm |
| Thickness of the negative triboelectric layer $d_1$ | 0.25/0.35/0.5 mm |
| Separation distance $x$ | 1-100 mm |
| Mechanical excitation frequency $f$ | 0.5-5 Hz |
| Surface charge density $\sigma_n$ | 61 μC/m$^2$ |

### 2.2.1 Finite element method (FEM) simulation

The simulation process is under open-circuit condition by COMSOL electrostatic modules. A 50*50*50 mm$^3$ cube with air was constructed as the boundary. Inside, A CS-TENG (30*30 mm$^2$) was established with ITO (as electrodes) and PTFE (as the dielectric layer). The surface charge density of the triboelectric layers was set as 61 μC/m$^2$. The upper part of CS-TENG was driven in a sinusoidal motion. The z-component of polarization vector ($P_z$), electric potential ($\boldsymbol{\varphi}$), electric field ($E_z$) and electric displacement ($D_z$) were obtained by FEM calculations.

### 2.2.2 Fabrication of CS-TENG

The single-sided adhesive PTFE worked as the dielectric layer. A same-sized ITO was attached to the PTFE as the bottom electrode. Another same-sized ITO was prepared as the positive tribo-layer and the top electrode.

### 2.2.3 Electrical measurement

The electrical output performance of the CS-TENGs is conducted by a programmable electrometer (Keithley model 6514 and Trek 344), driven by a linear motor (LINMOT E1100-RS-HC).

## 2.3 Results and Discussion

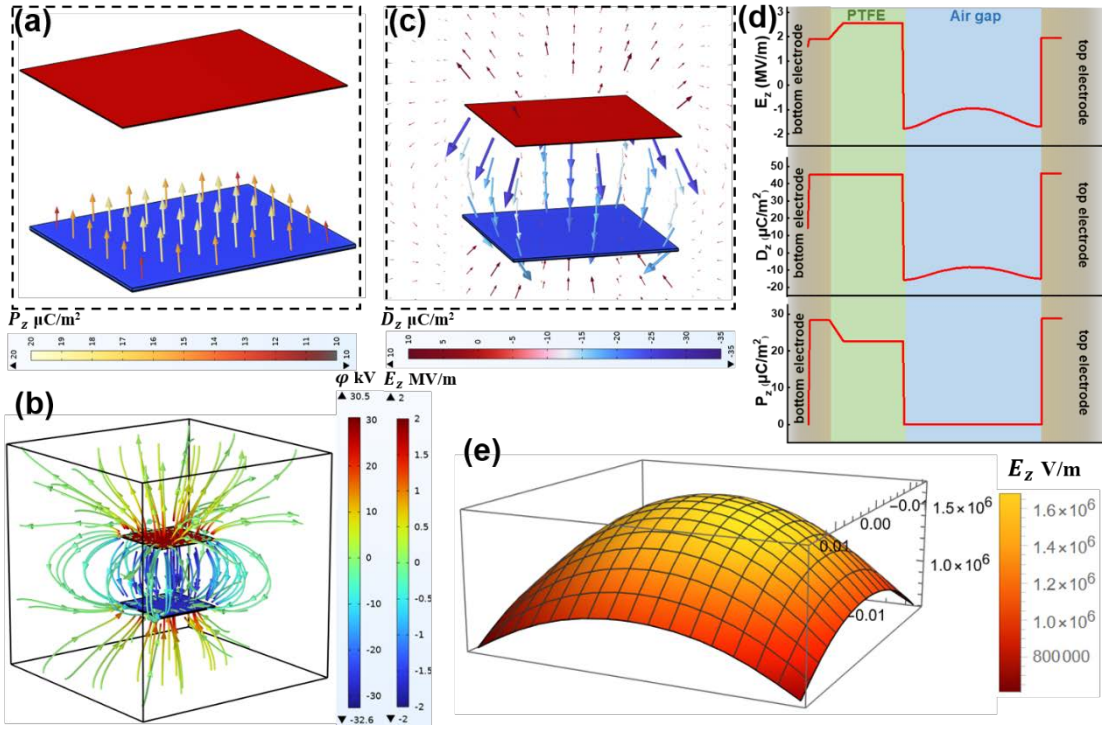


**Figure 2.1** Finite element modeling (FEM) simulation of a CS-TENG. Finite element simulation for z-component of (a) polarization vector ($P_z$), (b) electric potential ($\boldsymbol{\varphi}$) and electric field ($E_z$), (c) electric displacement ($D_z$). (d) The overlapping area changes of $E_z$, $D_z$, and $P_z$ throughout a CS-TENG. (e) The electric field distribution of an

identified position above a finite charged plane.

### 2.3.1 FEM simulation at open-circuit condition

To explore the working mechanism of the TENG from the first principle of classical electrodynamics, finite element modeling was performed by COMSOL Multiphysics, as shown in **Figure 2.1**. A finite size (30 cm*30 cm) of CS-TENG model was placed in the air environment with the Cartesian coordinate system. From the addition term ($P_s$) of Maxwell's equations, known as the Wang term, the surface of the dielectric medium would be polarized due to contact electrification.[30] **Figure 2.1a** shows the z-component of the polarization vector ($P_z$) of the finite dielectric layer, and triboelectric charges would remain on the dielectric surface after contact electrification. The distribution of electric potential ($\boldsymbol{\varphi}$) and electric field ($E_z$) was presented in **Figure 2.1b**. It is worth noting the distribution and the numerical variation of electric field lines. For one thing, the direction of electric field lines is not always perpendicular to the planes. For another, the electric field intensity changes along with distance. Combing electric field and polarization vector ($D_z = \varepsilon_0 E_z + P_z$), the electric displacement vector ($D_z$) was formed, as shown in **Figure 2.1c**, which is the origin of displacement current ($I_D$). An intersecting line was drawn to discuss the charge generation, transfer and induction throughout a CS-TENG. **Figure 2.1d** illustrates the changes of $E_z$, $D_z$, and $P_z$ from the bottom electrode to the top electrode. The great changes at the interface between air and PTFE were caused by the surface triboelectric charges. Throughout the air gap, the polarization vector ($P_z$) stabilized at zero, while the electric field ($E_z$) and the electric

displacement ($D_z$) changed with the separation distance. Then, the top electrode shielded all the electric field lines, resulting in a dramatic upswing in **Figure 2.1d**. These FEM results reveal the inapplicability of the parallel plate capacitor model (the electric field is uniform and always perpendicular to charged planes), and bring us to construct a more accurate and comprehensive model for TENGs. Based on the DDEF model, the electric field intensity distribution of a finite charged plane could be simulated in **Figure 2.1e**. It is probably not surprising that the electric field intensity at an identified position ($Z_0$) over a finite charged plane is not uniform. This begs the question: how to obtain the average electric field strength ($E_{Z_{avg}}$) of an arbitrary position over the finite charged planes and construct a new theoretical framework for CS-TENGs.

### 2.3.2 Derivation of the theoretical framework

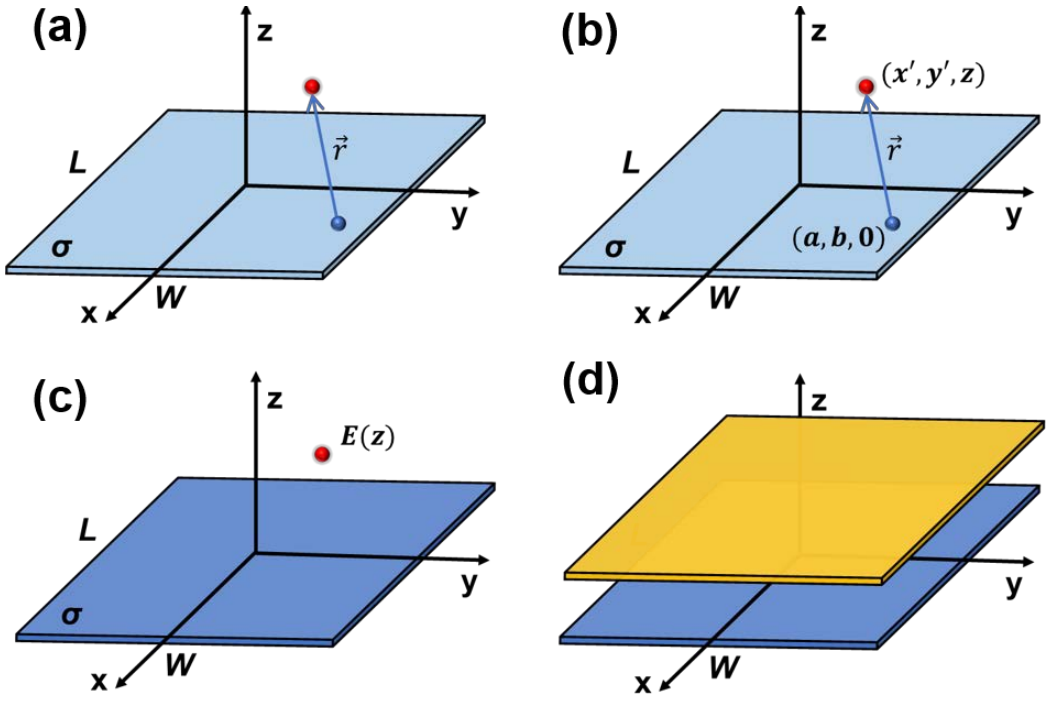


**Figure 2.2** 3D Charge model for finite charged plane. (a) The interacting electric field

$E$ produced by one charged particle to a single space charge $q$. (b) Any point in the space influenced by a point on the charged plane. (c) Arbitrary point over a finite charged plane. (d) The average electric field strength of a defined position over a finite charged plane.

The main target of this work is to optimize the construction of CS-TENG's formal physical model. After contact-triboelectrification, tribocharges exist on the surface of the dielectric layers, resulting in an electrostatic field.[19, 57] Once the CS-TENG is in constant and relatively slow movement, it could be regarded as the quasi-electrostatic model.[18] Attention should be paid to the distance-dependent/time-varying electric field. To include the complexity of geometries and surface topographies, the tribocharges would be treated as the point charges based on Coulomb's Law. Basically, for two charged particles with same charge magnitude $q$ and a distance of $r$, based on Coulomb's Law, the interacting electric field $E$ can be expressed as (**Figure 2.2a**):

$$E = \frac{F}{q} = \frac{q}{4\pi\varepsilon_0 r^2}\overrightarrow{r_u} = \frac{q}{4\pi\varepsilon_0 r^3}\vec{r} \tag{2-1}$$

in which $\overrightarrow{r_u}$ is the unit vector, and $\vec{r}$ is the vector between two charges. Therefore, when it comes to a charged plane with charge density $\sigma_n$ to a single charge $q$, the interacting electric field $E$ can be expressed as:

$$E = \frac{\sigma_n S}{4\pi\varepsilon_0 r^3}\vec{r} = \frac{\sigma_n}{4\pi\varepsilon_0}\oiint \frac{\vec{r}}{|r|^3}\,dr \tag{2-2}$$

For the electric field on a uniform charged $\sigma_n$ finite plane (size of $L \times W$), based on the 3D Cartesian coordinates on the central point of this plane, suppose any point $(x', y', z)$ in the space influenced by a point $(a, b, 0)$ on the charged plane, the overall electric field strength can be expressed as (**Figure 2.2b**):

$$E = \frac{\sigma_n}{4\pi\varepsilon_0}\int_{-\frac{L}{2}}^{\frac{L}{2}}\int_{-\frac{W}{2}}^{\frac{W}{2}}\frac{(x\prime-a,y\prime-b,z)}{((x\prime-a)^2+(y\prime-b)^2+z^2)^{\frac{3}{2}}}dx'dy' \quad (2\text{-}3)$$

Let $x = x' - a$, $y = y' - b$, then it is demonstrable that $dx = dx'$ and $dy = dy'$. Therefore, considering that the electric field strength $E(z)$ over a uniformly charged plane at a $z$ distance (**Figure 2.2c**):

$$E_z = \frac{\sigma_n}{4\pi\varepsilon_0}\int_{-\frac{L}{2}-b}^{\frac{L}{2}-b}\int_{-\frac{W}{2}-a}^{\frac{W}{2}-a}\frac{z}{(x^2+y^2+z^2)^{\frac{3}{2}}}dxdy \quad (2\text{-}4)$$

Therefore, the electric field is non-uniform at the entire plane and the central electric field strength is the maxima, as demonstrated in **Figure 2.1e**. Previously proposed model is insufficient on the discussion of the electric field $E_z$ approximation as only the strength on the central of the plane is taken into consideration. In this work, the projection transformation method was utilized to approximate the average value of the electric field strength $E_{z_{avg}}$. First, the integral electric field of the curved plane and its projection plane is determined as:

$$E_{total} = \frac{\sigma_n}{4\pi\epsilon_0}\int_0^{\frac{L}{2}}\int_0^{\frac{W}{2}}\int_{-\frac{L}{2}-b}^{\frac{L}{2}-b}\int_{-\frac{W}{2}-a}^{\frac{W}{2}-a}\frac{z}{(x^2+y^2+z^2)^{\frac{3}{2}}}dxdydadb \quad (2\text{-}5)$$

The projection area is like:

$$A = \frac{LW}{4} \quad (2\text{-}6)$$

According to this, the average electric field strength ($E_{z_{avg}}$) of the plane at any position over a finite charged plate (size of $L \times W$) could be determined as:

$$E_{z_{avg}} = \frac{\sigma_n}{\pi\varepsilon_0 LW}\int_0^{\frac{L}{2}}\int_0^{\frac{W}{2}}\int_{-\frac{L}{2}-b}^{\frac{L}{2}-b}\int_{-\frac{W}{2}-a}^{\frac{W}{2}-a}\frac{z}{(x^2+y^2+z^2)^{\frac{3}{2}}}dxdydadb = \frac{\sigma_n}{\pi\varepsilon_0 LW}f(z) \quad (2\text{-}7)$$

Here, $\sigma_n$ is the triboelectric charge density on the charged plane, and $\varepsilon_0$ is the vacuum

dielectric constant. For the metal-dielectric mode CS-TENG, as illustrated in **Figure 2.3**, the electric potential difference $\Delta V_E$ can be expressed based on the electric potential of two electrodes, in which:

$$\Delta V_E = \varphi_{\mathrm{a}} - \varphi_b \tag{2-8}$$

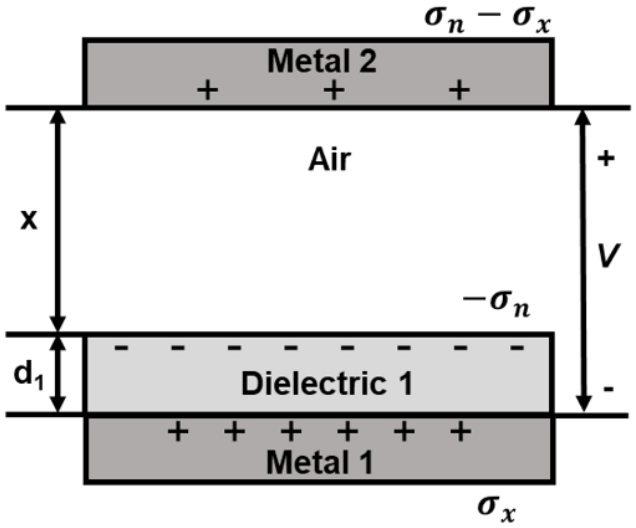


**Figure 2.3** A theoretical model for metal-dielectric CS-TENG.

According to equation (2-7), the potential of two parts of the CS-TENG can be expressed as:

$$\varphi_{\mathrm{a}} = \frac{\sigma_n - \sigma_x}{\pi\varepsilon_0 LW}\int_0^{+\infty} f(z)dz - \frac{\sigma_n}{\pi\varepsilon_0 LW}\int_x^{+\infty} f(z)dz + \frac{\sigma_x}{\pi\varepsilon_0 LW}\int_{x+d_1}^{+\infty} f(z)dz$$

$$= \frac{\sigma_n}{\pi\varepsilon_0 LW}\int_0^{x} f(z)dz - \frac{\sigma_x}{\pi\varepsilon_0 LW}\int_0^{x+d_1} f(z)dz \tag{2-9}$$

and

$$\varepsilon_{r1}\varphi_b = \frac{\sigma_x}{\pi\varepsilon_0 LW}\int_0^{+\infty} f(z)dz - \frac{\sigma_n}{\pi\varepsilon_0 LW}\int_{d_1}^{+\infty} f(z)dz + \frac{\sigma_n - \sigma_x}{\pi\varepsilon_0 LW}\int_{x+d_1}^{+\infty} f(z)dz$$

$$= \frac{\sigma_x}{\pi\varepsilon_0 LW}\int_0^{x+d_1} f(z)dz - \frac{\sigma_n}{\pi\varepsilon_0 LW}\int_{d_1}^{x+d_1} f(z)dz \tag{2-10}$$

Therefore, electric potential difference $\Delta V_E$ can be expressed as:

$$\Delta V_E = \frac{\sigma_n}{\pi\varepsilon_0 LW}\int_0^{x} f(z)dz - \frac{\sigma_x}{\pi\varepsilon_0 LW}\int_0^{x+d_1} f(z)dz$$

$$-\frac{1}{\varepsilon_{r1}}\left(\frac{\sigma_x}{\pi\varepsilon_0 LW}\int_0^{x+d_1} f(z)dz - \frac{\sigma_n}{\pi\varepsilon_0 LW}\int_{d_1}^{x+d_1} f(z)dz\right) \tag{2-11}$$

For the open circuit voltage $V_{OC}$, namely when $\sigma_x = 0$, it can be derived as:

$$V_{OC} = \frac{\sigma_n}{\pi\varepsilon_0 LW}\int_0^{x} f(z)dz + \frac{1}{\varepsilon_{r1}}\frac{\sigma_n}{\pi\varepsilon_0 LW}\int_{d_1}^{x+d_1} f(z)dz \tag{2-12}$$

Similarly, for the short circuit current $I_{SC}$, namely when $\Delta V_E = 0$, it can be derived as:

$$\sigma_{x_{sc}} = \frac{\sigma_n\left(\int_0^{x} f(z)dz + \frac{1}{\varepsilon_{r1}}\int_{d_1}^{x+d_1} f(z)dz\right)}{\int_0^{x+d_1} f(z)dz + \frac{1}{\varepsilon_{r1}}\int_0^{x+d_1} f(z)dz} \tag{2-13}$$

Therefore,

$$Q_{SC} = S\sigma_{x_{SC}} \tag{2-14}$$

$$I_{SC} = S\frac{d\sigma_{x_{SC}}}{dt} \tag{2-15}$$

in which $S$ is the contact surface area.

### 2.3.3 Numerical implementation

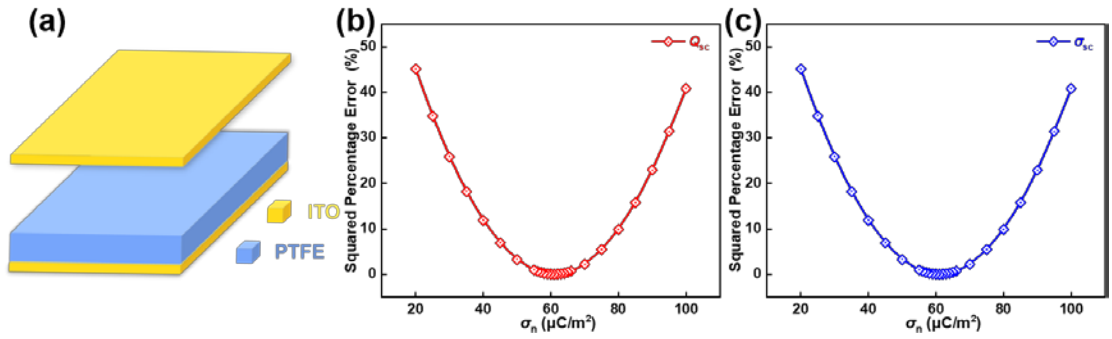


**Figure 2.4** Experimental design and tests. (a) Schematic for a CS-TENG for experiments. Sum of the squared percentage error of (b) transferred charges and (c) transferred charge density between the experimental and the 3D spatial charge model.

To testify the practicality of the QETD model, this quasi-electrostatic model was utilized to conduct predictions of experimental results. A metal-dielectric mode CE-TENG was fabricated with ITO and Polytetrafluoroethylene (PTFE) film, as illustrated in **Figure 2.4a**. Before all the theoretical simulation, the value of triboelectric charge

density $\sigma_n$ was determined by the squared percentage error calculation. In **Figure 2.4b-c**, it is noted that 61 μC/m$^2$ of $\sigma_n$ created the smallest squared percentage error between the experimental and theoretical results. Therefore, $\sigma_n$ was set as 61 μC/m$^2$ in all the following simulations.

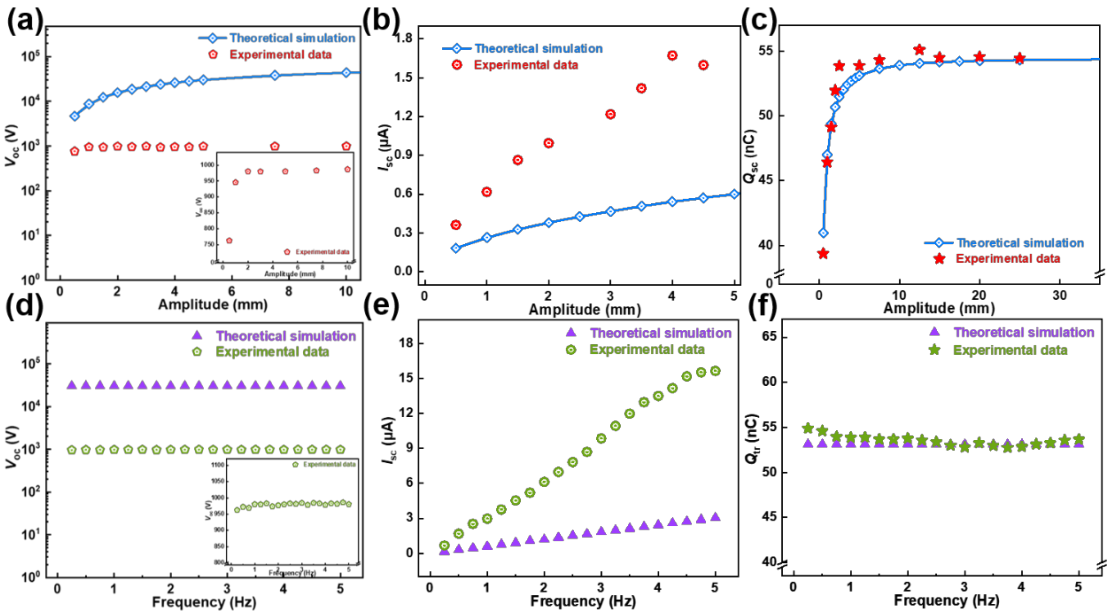


**Figure 2.5** Experimental data versus theoretical simulation under different external driving conditions. (a) Open-circuit voltage ($V_{oc}$), (b) short-circuit current ($I_{sc}$) and (c) transferred charge ($Q_{sc}$) under different amplitudes. (d) Open-circuit voltage ($V_{oc}$), (e) short-circuit current ($I_{sc}$) and (f) transferred charge ($Q_{sc}$) under different frequencies.

**Figure 2.5** shows the output performance of the as-fabricated CS-TENG under different external driving conditions, including the simulated and experimental results. **Figure 2.5a-c** reveal the output performance of CS-TENG under different separation distances. Open-circuit voltage ($V_{oc}$) and short-circuit current ($I_{sc}$) enhance with the increasing amplitude, while transferred charge ($Q_{sc}$) increases before stabilizing. The output performance under various frequencies can be found in **Figure 2.5d-f**. The drive

frequency does not affect open-circuit voltage ($V_{oc}$) and transferred charge ($Q_{sc}$), but the short-circuit current ($I_{sc}$) presents a trend of growth as frequency elevates. The experimental and theoretical results show the same changing tendency and regularity, but there are deviations in the values. The reasons for these deviations could be discussed in two aspects. First, the QETD model, according to the quasi-electrostatic model, is based on vacuum conditions. Air breakdown would occur at the air gap of the CS-TENG in the practical air environment, which would greatly reduce experimental output, especially for the voltage.[41, 45] Second, the testing data is not accurate enough due to the impedance mismatch between CS-TENG and the electrometer. **Figure 2.6** displays the influence of device constructions, including the thickness and size of the dielectric layer. All the electrical outputs reduce as the thickness of PTFE becomes thicker (**Figure 2.6a-c**). As for the device's size, a larger area produces a higher output performance of CS-TENG (**Figure 2.6d-f**). Both the theoretical simulation and the experimental data follow the rules.

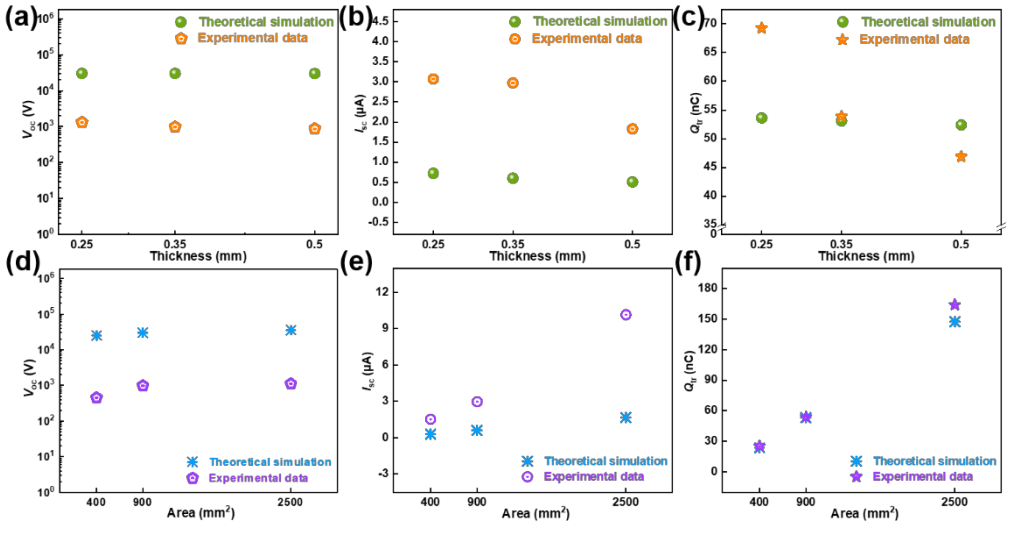


**Figure 2.6** Experimental data versus theoretical simulation with different device

constructions. (a) open-circuit voltage ($V_{oc}$), (b) short-circuit current ($I_{sc}$) and (c) transferred charge ($Q_{sc}$) with different thicknesses of PTFE. (d) open-circuit voltage ($V_{oc}$), (e) short-circuit current ($I_{sc}$) and (f) transferred charge ($Q_{sc}$) with different sizes of PTFE.

### 2.3.4 Power generation from the conduction current

Maxwell's displacement current is the internal driving force of CS-TENG, and CS-TENG's external expression is the conduction current (**Figure 2.7a**).[58] Suppose the CS-TENG is directly connected with a resistor $R$, based on Kirchhoff's Law, the entire circuit can be expressed as:

$$-RS\frac{d\sigma_x}{dt} = \Delta V_E \tag{2-16}$$

Namely,

$$RS\frac{d\sigma_x}{dt} + \frac{\sigma_n}{\pi\varepsilon_0 LW}\int_0^x f(z)dz - \frac{\sigma_x}{\pi\varepsilon_0 LW}\int_0^{x+d_1} f(z)dz - \frac{1}{\varepsilon_{r1}}\left(\frac{\sigma_x}{\pi\varepsilon_0 LW}\int_0^{x+d_1} f(z)dz - \frac{\sigma_n}{\pi\varepsilon_0 LW}\int_{d_1}^{x+d_1} f(z)dz\right) = 0 \tag{2-17}$$

Define $x$ as a function of time ($x = H\sin(2\pi ft + \frac{3}{2}\pi) + H$), equation (9) can be solved and $\sigma_x$ can be evaluated. Therefore, the output power of the CS-TENG, namely the power dissipated on the resistor $R$, can be evaluated as:

$$P_{out} = I^2(t)R = R\left(S\frac{d\sigma_x}{dt}\right)^2 \tag{2-18}$$

and the output energy can be evaluated:

$$E_{out} = \int P(t)dt \tag{2-19}$$

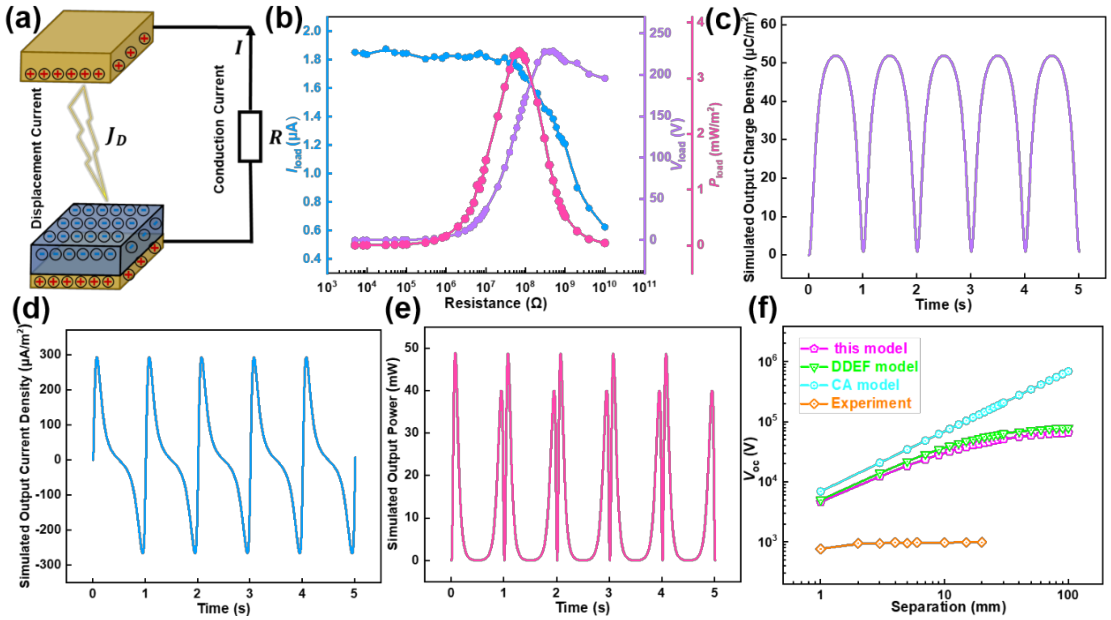


**Figure 2.7** Experimental data versus theoretical simulation with different load resistors. (a) Schematic for a CS-TENG with internal displacement current and external capacitive conduction current. (b) Peak values of the output performance with various resistors. The theoretical output (c) charge density, (d) current density and (e) power density along with time through predictions with a resistor of 70 MΩ. (f) Comparison between all theoretical models and experimental data about Voc.

**Figure 2.7b** shows the load outputs of the as-fabricated CS-TENG when connected with varying load resistors. The peak load current decreases with the increasing resistors, but the voltage of the load upgrades. The peak power reaches the highest value of 3.49 mW/m$^2$ with a load of 70 MΩ. **Figure 2.7c-e** provide the simulated time-varying output of the load resistor at 70 MΩ through equation (2-16) according to the quasi-electrostatic model. The simulated outcomes demonstrate the charge density of 52 μC/m$^2$, current density of 290 μA/m$^2$ and peak power of 48 mW at 1 Hz. From above, the internal circuit and external circuit of CS-TENG were linked to form a complete closed loop from Maxwell's displacement current to conduction current.

### 2.3.5 Comparison among existing models

The open-circuit voltage ($V_{oc}$) is the key parameter for comparative analysis. **Figure 2.7**f displays the predictions of $V_{oc}$ within all the previously published models. The first category is the equivalent electrical circuit model, containing the CA model and Norton's equivalent circuit model.[27] In this model, $V_{oc}$ is linearly proportional to the separation distance. This work further optimizes the DDEF model, and they belong to the formal physical model (quasi-electrostatic model).[22] In the quasi-electrostatic model, $V_{oc}$ improves with longer separation distance, accompanied by a decreasing gradient, and ultimately remains constant. This could be explained that the electric field would dissipate along with the separation distance, while the electric field is uniform in CA model. This work is slightly lower than DDEF model, and the deviations result from the different approximation methods for average electric field strength ($E_{z_{avg}}$) as mentioned above. The experimental $V_{oc}$ presents the same tendency as the quasi-electrostatic model, but stabilizes at a smaller value and reaches the plateau earlier. Therefore, this work provides a better correction of the formal physical model for CS-TENG, which helps make predictions of CS-TENG's output performance.

## 2.4 Conclusion

This paper establishes a quasi-electrostatic model in a Cartesian coordinate system for CS-TENG to reveal the intrinsic working mechanism of TENGs. Starting from classical electrodynamics, the distribution of polarization vector ($P_z$), electric potential ($\boldsymbol{\varphi}$), electric field ($E_z$) and electric displacement ($D_z$) over each layer was presented by the

FEM simulation. The FEM results bring us that the electric field value is changeable along with the distance, and the electric field direction is not always perpendicular to the charged plane. Therefore, the electric field of a finite charged plane was reconstructed, where the triboelectric charges were regarded as point charges according to Coulomb's Law. Then, the theoretical framework of CS-TENG was set up, containing the fundamental output performance and power output with a resistor. For each variable, both experimental data and predictions from the quasi-electrostatic model were compared to justify this QETD model. The consistent trends present that TENGs' output enhances with longer separation distances in tiny ranges, but the magnitude of the change eventually stabilizes. $I_{sc}$ increases with higher frequencies, while $V_{oc}$ and $Q_{sc}$ are independent of frequency. As for the structural design, the output performance reduces as the dielectric layer becomes thicker, but ascends with the increasing sizes. Nevertheless, TENGs' testing methodology should be further developed and advanced to present more realistic and relevant experimental results to eliminate deviations. The differences among all the previous theoretical models were given, with the results that the output trend of QETD model is most consistent with experimental data. This QETD model bridges the gap between the theoretical model and the experimental results, making a better correction for TENG's output performance predictions. It will contribute to a deeper understanding of the working mechanism of TENGs and provide theoretical support for further development and design of TENGs.

# CHAPTER 3 Charge Regulation Enabled by MXene/TiO2 Intermediate Layer

## 3.1 Background

Since 2012, triboelectric nanogenerator (TENG) has been considered promising energy converters based on the coupling effect of contact electrification and electrostatic induction.[4] It shows great potential to function as energy harvesters and self-powered sensors.[59-62] For an energy harvester, power output and energy conversion efficiency are essential criteria to evaluate one's performance.[33, 48] For self-powered sensors, stability and repeatability should be ensured to obtain reliable sensitivity, linearity, and response.[63-67] Theoretically, these factors depend on triboelectric charges.[3, 11, 27, 53, 68-69] The working principle of TENG could be regarded as charges separation by triboelectrification and electrostatic induction on the electrode to obtain electrical output.[27, 69] To achieve stable and high-performance output, the improvement strategies could be divided into two directions: charge generation and charge storage.[34] To generate more triboelectric charges, classic methods were introduced, such as surface functionalization, ion injection and spontaneous polarization, *etc.*[33, 37, 41, 70-74] They are feasible to implement the performance enhancement. However, the triboelectric charges would dissipate. Due to triboelectrification, there would be negative triboelectric charges on the negative tribo-material surface.[75] An electron concentration gradient forms from the surface to the tribo-material interior.[46] Besides, the bottom electrode would induce positive charges resulting from the negative charges on the negative tribo-material surface. Consequently, an interfacial electric field would form

between the bottom electrode and negative tribo-material, causing the electrons to be easy to diffuse into the negative tribo-material and cancel out with the induced positive charges.[39, 76-77] Besides, the free positive particles in the air gap would neutralize with triboelectric charges on the surface.[77] Overall, the electrons diffuse into the air or the tribo-material could result in charge decay, making triboelectric charge density decline. That is the root reason for the poor performance and low stability and repeatability of TENGs. Therefore, charge storage is significant for reducing triboelectric charges, and could be realized by adding charge trap sites and increasing dielectric constant.[34]

MXene ($Ti_3C_2T_x$) is a kind of two-dimensional conductive nanosheet.[78] There are abundant surface terminations that could attract and trap electrons, and the free electrons could move freely on the nanosheets.[79-82] MXene could be converted to $TiO_2$ by an in-situ oxidation reaction.[83-85] $TiO_2$ acts as a kind of high permittivity material with a relative permittivity of 80, which could play the role of dielectric constant regulation and polarization enhancement.[79, 81] In addition, in the MXene/$TiO_2$ hybrid system, the adjacent stacked MXene flakes could disperse $TiO_2$ nanoparticles and establish additional conductive channels to transport electrons to the deep part of the hybrid material, so that the triboelectric charge could be trapped and stored to the greatest extent.[86-88]

This chapter proposed an intermediate layer made by MXene/$TiO_2$ hybrid film, located between the negative tribo-material and the bottom electrode. Through partial oxidation of the MXene, a MXene/$TiO_2$ hybrid community could be prepared for the MXene/$TiO_2$

based TENG (MT-TENG). With the coupling effect of electron trapping & blocking and polarization effect, the electrons on tribo-material could be firmly captured and prevented from diffusion. Theoretical simulations, physical characterizations and electrical measurements were conducted to make comparisons and validate enhancements. A metal-oxidized MXene-semiconductor (MOS) structured device was also designed to evaluate the charge storage property and acquire the dielectric constant. Moreover, a charge decay test was performed to verify the charge blocking capacity.

## 3.2 Experiments and Methods

### 3.2.1 MXene Synthesis

The synthesis process is shown in the **Figure 3.1**. MXene was etching from MAX ($Ti_3AlC_2$, 400 mesh) by hydrofluoric acid. First, 40 ml hydrochloric acid and 2 g Lithium fluoride were added in a Teflon beaker to mix for 30 min with a rotating speed of 400 rpm to form hydrofluoric acid. Second, 2 g $Ti_3AlC_2$ was added to the beaker slowly and the temperature was heating up to 35℃. Third, after keeping stirring for 24 h, the as-obtained multi-layered $Ti_3C_2T_x$ solution was repeated sonication and centrifugation 5 times until the PH value reached 5. Forth, to obtain low-layered $Ti_3AlC_2$, ethanol was added to delaminate the multi-layered $Ti_3AlC_2$ by sonication for 1.5 h. Fifth, ethanol was removed by centrifugation (10000 rpm, 10 min) and 80 ml deionized water was added to disperse the MXene nanosheet (3500 rpm, 3 min). The MXene dispersion was conserved with argon at low temperature (1-10℃).


**Figure 3.1** Schematic illustration of the low-layered MXene nanosheet synthesis process.

### 3.2.2 Fabrication of MT-TENG

The as-synthesized MXene solution was adapted into 3 mg/ml and kept stirring at 50℃ in the air. Different degrees of oxidation of MXene solution would be obtained by mixing for different duration (6 h, 9 h, 12 h). The MXene/$TiO_2$ hybrid films were prepared by suction filtration with MCE filter membranes and dried in a vacuum oven (50℃, 10 h).

The filtered MCE (50 μm pore size) and MXene/$TiO_2$ hybrid film worked as the triboelectric and intermediate layers, respectively. A same-sized Cu foil was attached to the other side of the MXene/$TiO_2$ hybrid film. Another Cu foil with a sponge substrate worked as the positive tribo-layer. The total effective size is 2.8 cm in side length.

### 3.2.3 Fabrication of MOS Devices

The different oxidized MXene solution was first diluted to 2 mg/ml. Then, the diluted solution was dropped onto the heavily doped n-type silicon substrates at 2000 rpm for 20 s. After that, the samples were oxidized at 50 °C for 1 min on a hotplate in air condition. Finally, a shadow mask with d = 0.3 mm diameter circulars was used to deposit aluminium (Al) on the samples by thermal evaporation as the metal layer of the MOS devices.

### 3.2.4 Characterization and Measurement

Scanning electron microscopy (SEM, Carl Zeiss Supra 55) was used to display the morphology of MXene/$TiO_2$ hybrid film and MCE membrane. The chemical states of different oxidized degrees of MXene were determined by X-ray diffraction (XRD, Empyrean), X-ray photoelectron spectroscopy (XPS) and Ultraviolet photoelectron spectroscopy (UPS) measurements (Kratos AXIS UltraDLD) with Al Kα radiation (1486 eV) as a probe. Contact potential difference (CPD) analysis was performed by the atomic force microscope with scanning Kevin probe (AFM-SKP, Cypher S).

The electrical output performance of the MT-TENGs is conducted by a programmable electrometer (Keithley model 6514) and driven by a linear motor (LINMOT E1100-RS-HC). The C-V and C-F characteristics test of the MOS device were revealed utilizing a semiconductor analyzer (Keysight, B1500 A).

## 3.3 Results and Discussion

### 3.3.1 Structure Design of MT-TENG with an intermediate layer

The MXene/$TiO_2$ hybrid film as the intermediate layer between the mixed cellulose esters (MCE) membrane and Cu electrode is put forward, as shown in **Figure 3.2**. The MXene/$TiO_2$ layer plays the role of electron trapping and blocking to prevent the electron generated on the negative tribo-material to screen out. Apart from this, the $TiO_2$ nanoparticles in the MXene/$TiO_2$ hybrid film show high permittivity, resulting in a synergetic effect of controlling the dielectric constant and inducing polarization, which enhance triboelectric surface charges.[80]

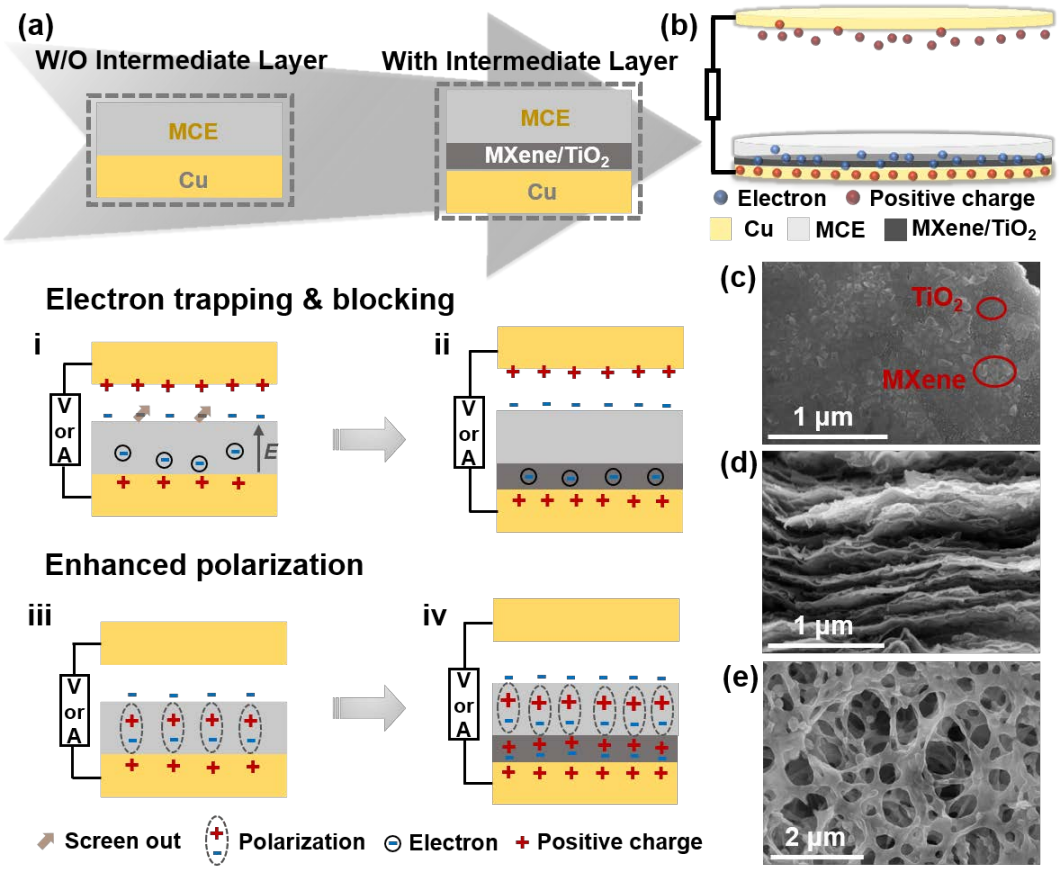


**Figure 3.2** Structure design of MT-TENG and morphology characterization of MXene/TiO2 hybrid film. (a) Schematic illustration of coupling effects of the electron trapping & blocking and polarization to enhance the surface charge density. (b) Schematic diagram of the MT-TENG. SEM images of (c) the surface of MXene/TiO2 hybrid film, (d) the cross-section of MXene/TiO2 hybrid film, (e) the surface of the mixed cellulose esters (MCE) membrane.

The classic model of TENG is schematically shown in **Figure 3.2**a(i). Upon physical contact between the top Cu electrode and the MCE membrane, oppositely charged surfaces are produced. Along with the separation of the Cu electrode, positive charges would be induced at the bottom Cu electrode as a result of the transferred charges through the external circuit. Therefore, an upward interfacial electric field would form at the MCE medium, which would cause a portion of electric field-induced drift

electrons to recombine with the positive charges on the bottom electrode.[77, 89] In the intermediate layer, the MXene nanosheets work as the electron trapping site with physical defects and chemical defects. The $TiO_2$ nanoparticles act as the blocking effect to screen the combination of electrons and positive charges.[79] Therefore, as shown in **Figure 3.2**a(ii), the portion of electrons would store in the intermediate layer but not neutralize with the induced positive charges on the Cu electrode. Moreover, the formed $TiO_2$ improves the dielectric property, controlling the capacitance and strengthening the polarization effect. The polarization effect factually plays a significant role in the alignment of the dipoles on both sides of the intermediate layer, as shown in **Figure 3.2**a(iv), causing more induced charges on the Cu electrode. **Figure 3.2**b shows a schematic illustration of the vertical contact-separate mode MT-TENG. The commercial MCE membrane functions as the negative triboelectric layer with Cu foil as the bottom electrostatic induction electrode. By contrast, another Cu foil is employed as both positive triboelectric layer and the top electrode.

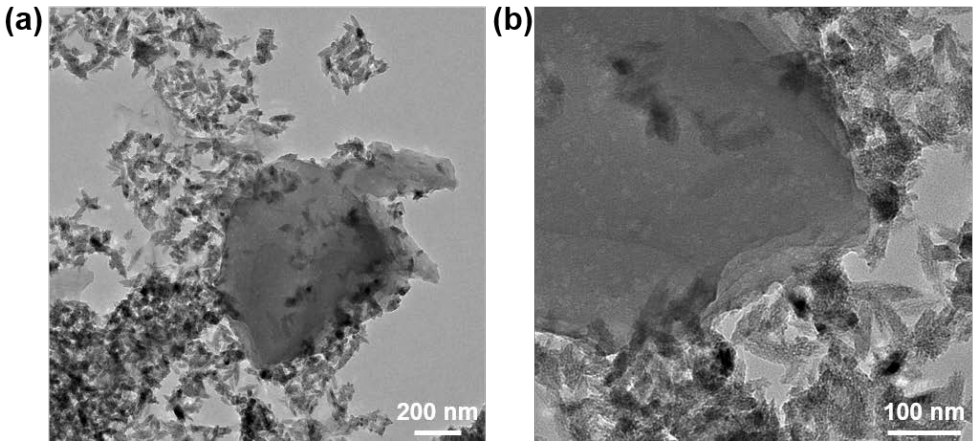


**Figure 3.3** (a) TEM images of the interaction between and $TiO_2$. (b) Detailed morphology of the MXene nanosheet edges.

The MXene/$TiO_2$ hybrid film was fabricated attached to the MCE membrane (**Figure 3.2**e) by suction filtration. **Figure 3.2**c illustrates the SEM morphology image of the MXene/$TiO_2$ hybrid film. A hybrid film consisting of MXene nanosheets and $TiO_2$ nanoparticles are formed. It could be noted that the flaked MXene nanosheets have a size of ~600 nm and $TiO_2$ nanoparticles roughly present size of ~10 nm. The detailed morphology of the interaction between the MXene and $TiO_2$ was presented in **Figure 3.3,** $TiO_2$ nanoparticles were observed to load on the substrates and at the edges of MXene nanosheets, which is in accordance with the in situ oxidation mechanism of MXene.[88] The MXene/$TiO_2$ hybrid film holds a thickness of ~10 μm (Figure 1d). It is confirmed that the MXene could successfully form $TiO_2$ by in situ reaction, which could construct a MXene/$TiO_2$ hybrid film as the intermediate layer.

### 3.3.2 Characterization of Different Oxidation Degrees of MXene

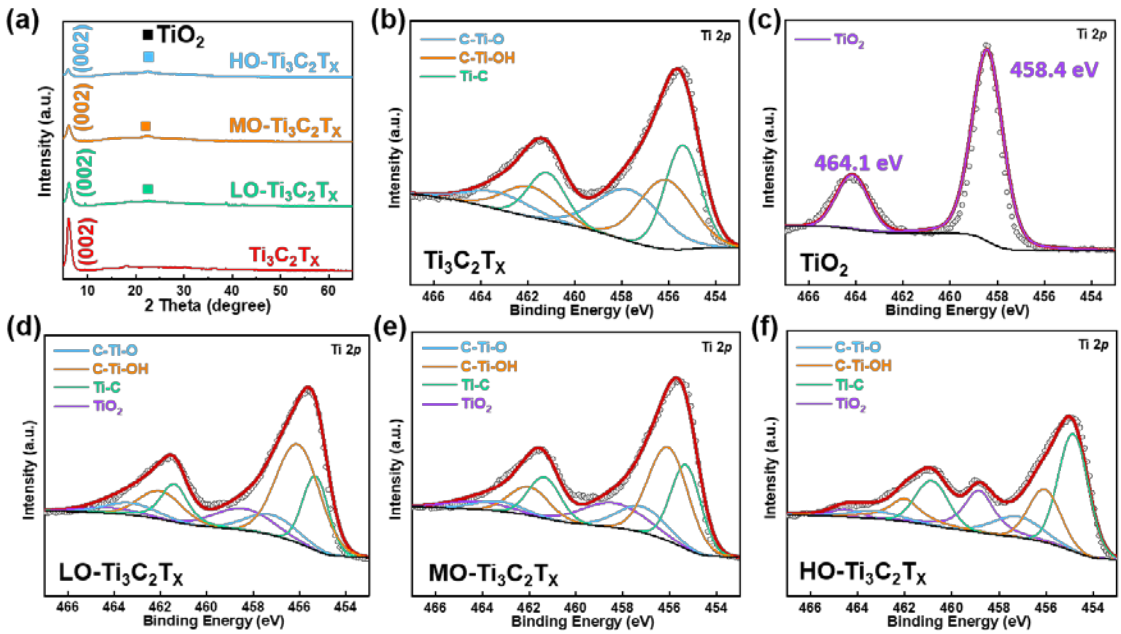


**Figure 3.4** Characterizations of different oxidation degrees of MXene. (a) XRD patterns of different oxidized MXene. XPS spectra of (b) $Ti_3C_2T_x$, (c) pure $TiO_2$, (d)

LO-$Ti_3C_2T_x$, (e) MO-$Ti_3C_2T_x$ and (f) HO-$Ti_3C_2T_x$.

To achieve the optimal composition of the MXene/$TiO_2$ hybrid community, different oxidation degrees of MXene were prepared and utilized to fabricate the MT-TENGs. Specific characterizations of pure MXene ($Ti_3C_2T_x$), lightly oxidized MXene (LO-$Ti_3C_2T_x$), moderately oxidized MXene (MO-$Ti_3C_2T_x$) and heavily oxidized MXene (HO-$Ti_3C_2T_x$) are demonstrated in **Figure 3.4**. As shown in **Figure 3.4**a, a prominent intense peak (002) appears at 7° for the $Ti_3C_2T_x$, indicating $Ti_3C_2T_x$ was successfully etched from $Ti_3AlC_2$. With the increasing oxidation degree of $Ti_3C_2T_x$, the (002) peak gradually shifts from 7° to 6° with a decreasing peak intensity.[79, 90] A new peak at about 24.7° corresponding anatase $TiO_2$ could be found in oxidized MXene, presenting part of MXene's conversion to $TiO_2$.[79]

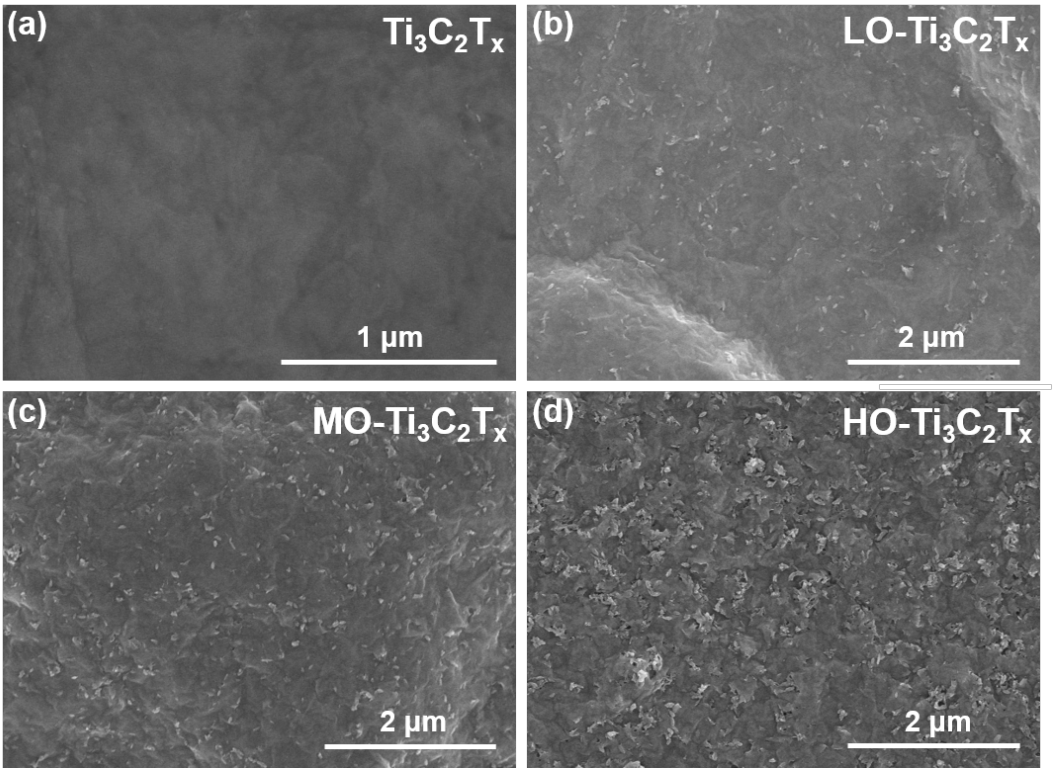


**Figure 3.5** SEM images of the morphology surface of (a) pure $Ti_3C_2T_x$, (b) LO-$Ti_3C_2T_x$,

(c) MO-$Ti_3C_2T_x$ and HO-$Ti_3C_2T_x$.

The SEM images in **Figure 3.5** show the morphology surface, and more nanoparticles are presented with increasing oxidation degree of $Ti_3C_2T_x$ on the films. To further determine the chemical changes and bonding reorganization of MXene oxidation, X-ray photoelectron spectroscopy (XPS) analysis of different oxidation degrees of MXene was performed and the Ti 2*p* spectra (Ti $2p_{3/2}$ and Ti $2p_{1/2}$) were presented in **Figure 3.4**b-f. The doublet at 455.2 and 461.2 eV represents the Ti–C bond, while the signals at 457.2 and 463.3 eV result from C–Ti–O bond and the doublet at 456.06 and 462.0 eV stands for C–Ti–OH bond.[79-80, 91] As shown in **Figure 3.4**d-f, with the increasing oxidation, the Ti–C bond signals gradually strengthen, and the signals of C–Ti–O and C–Ti–OH bond show a declining trend, which means part of surface terminations of MXene nanosheets were reacted and oxidized. Compared with the signals of pure anatase $TiO_2$ in **Figure 3.4**c, the doublet of the Ti–O bond occurs at 458.4 and 464.1 eV. It is noted from **Figure 3.4**d-f that the purple peak at 458.4 eV enhances with the increasing degree of oxidation, and the peak at 464.1 eV (Ti $2p_{1/2}$) obviously appears in the HO-$Ti_3C_2T_x$ sample (**Figure 3.4**f). The results indicate the transformation from MXene surface terminations into $TiO_2$. It is meaningful to regard that a community containing both MXene and $TiO_2$ was formed due to the in-situ oxidation of MXene.

### 3.3.3 Electrical measurement of MT-TENGs

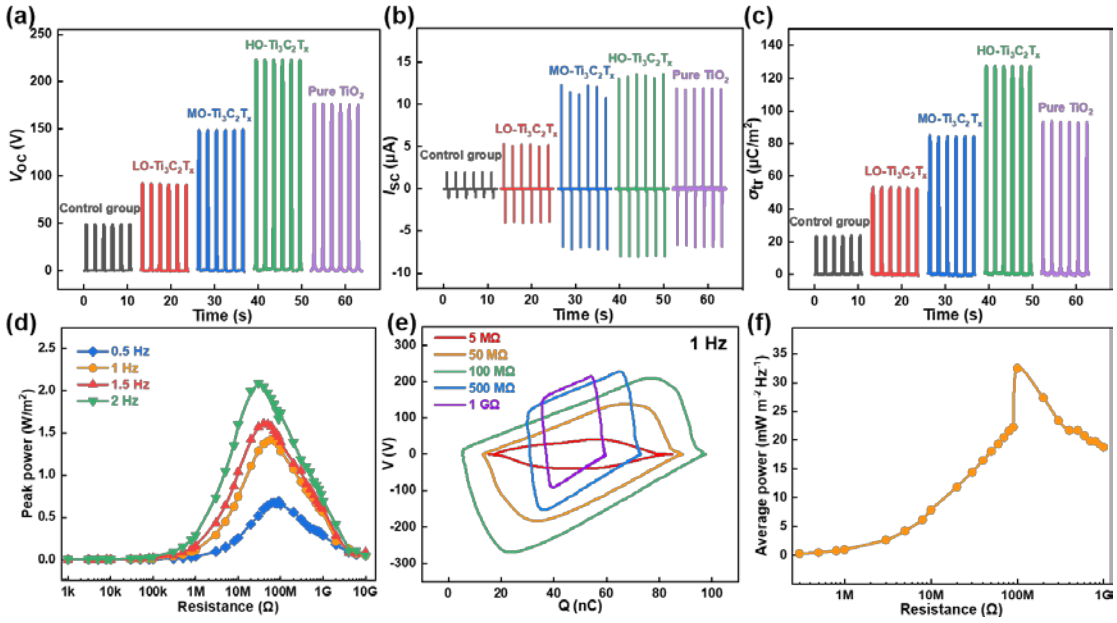


**Figure 3.6** Electrical output performance of MT-TENGs. (a) Open-circuit voltage ($V_{oc}$), (b) short-circuit current ($I_{sc}$), (c) transferred charge density ($\sigma_{tr}$) of MT-TENGs with different degrees of oxidation. (d) Peak power density of MT-TENG versus load resistance under different frequencies. (e) V-Q plots with various load resistances at 1 Hz. (f) Average power density of MT-TENG with various load resistances at 1 Hz.

**Figure 3.6** plots the electrical output performance of the MT-TENGs with the intermediate layer composed of MXene with different degrees of oxidation. A linear motor was utilized to drive all the MT-TENGs. **Figure 3.6**a-c shows the pristine TENG in control group (TENG without the intermediate layers) performs a peak open-circuit voltage ($V_{oc}$) of ~50 V; a peak short-circuit current ($I_{sc}$) of ~0.2 μA and total transferred charges ($Q_{tr}$) of ~19 nC with a peak charge density ($\sigma_{tr}$) of ~23.8 μC/m$^2$. Relatively, the MT-TENGs with intermediate layers show varying fold improvement. From LO-$Ti_3C_2T_x$ to HO-$Ti_3C_2T_x$, the electrical output performance is promoted gradually as the increasing oxidation. The MT-TENG with HO-$Ti_3C_2T_x$ intermediate layer presents the

optimal output performance. The $V_{oc}$ increases to 224 V and the $\sigma_{tr}$ could reach 128 μC/m$^2$, which exhibited a 5-fold enhancement of the pristine TENG. It could be confirmed that the MXene/$TiO_2$ hybrid layers take an outstanding role as an intermediate layer to facilitate the electrical output of TENGs. Furthermore, to verify the function of both MXene and $TiO_2$, but not only the $TiO_2$, a MT-TENG with pure $TiO_2$ as the intermediate layer was fabricated and tested for comparison. The charge density of pure $TiO_2$ based TENG is 94 μC/m$^2$, indicating a certain distance from the HO-$Ti_3C_2T_x$ layer. The $TiO_2$ from the in situ oxidization of MXene could prevent $TiO_2$ agglomeration and establish additional conductive channels to transport electrons to the deep part of the composites, so that the triboelectric charge could be trapped and stored to the greatest extent. Therefore, the coupling effect of electron trapping-blocking and polarization effects resulting from both MXene nanosheets and $TiO_2$ nanoparticles is indispensable for enhancing TENG output performance.

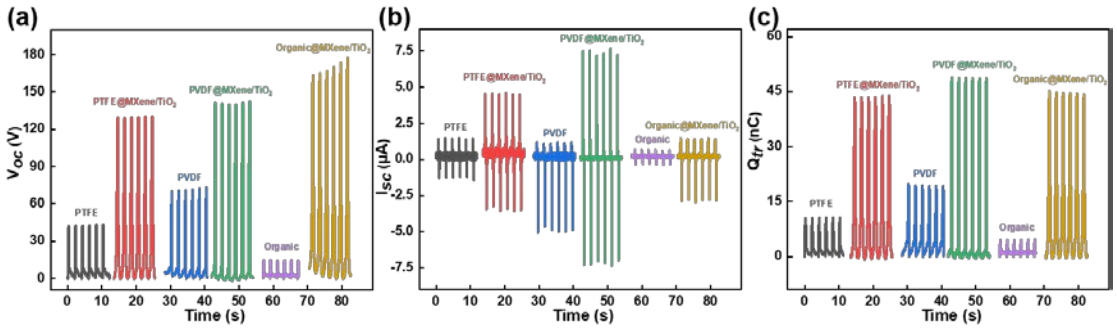


**Figure 3.7** (a) Open-circuit voltage ($V_{oc}$), (b) Short-circuit current ($I_{sc}$), (c) Transferred charge ($Q_{tr}$) of MT-TENGs with different triboelectric layers with and without MXene/$TiO_2$ layer.

Furthermore, TENGs with different triboelectric layers, including PTFE (Polytetrafluoroethylene), PVDF (Polyvinylidene fluoride) and MO (membrane for the

filtration of organic solution) were fabricated into another three comparison groups with and without the MXene/$TiO_2$ layers. As displayed in **Figure 3.7**, all the MT-TENGs exhibit significant enhancement in terms of $V_{oc}$, $I_{sc}$ and $Q_{tr}$ compared with the pristine TENGs. The power output of the optimal MT-TENG with HO-$Ti_3C_2T_x$ was measured with various load resistances. **Figure 3.6**d shows the peak power of the MT-TENG and indicates that the highest peak power could reach 2.09 W $m^{-2}$ with a 100 MΩ load resistance at 2 Hz. The V-Q plots with several chosen load resistances in **Figure 3.6**e provide the energy output at each cycle by calculating the encircled area of the closed loops. The energy output at 100 MΩ outplays with 25.48 μJ for each cycle. **Figure 3.6**f lists the average power density versus different load resistances, which could also be obtained the optimal matching resistance of 100 MΩ and the highest average power output of 32.5 mW $m^{-2}$ at 1 Hz.

**Table 3.1** Parameters of the MT-TENG.

| **Parameter** | **Value** |
|---|---|
| Mass of the device $m_{TENG}$ | 0.3995 g |
| Volume of the device $V_{TENG}$ | 0.3454 $cm^3$ |
| Mass of the top layer $m_{top}$ | 0.0747 g |
| Maximum separation distance $x_{max}$ | 5 cm |
| Thickness of the triboelectric layer $d_1$ | 0.145 mm |
| Thickness of the intermediate layer $d_2$ | 0.01 mm |

| | |
|---|---|
| Relative permittivity of the triboelectric layer $\varepsilon_{r1}$ | 4 |
| Relative permittivity of the intermediate layer $\varepsilon_{r2}$ | 12 |
| Effective thickness of the dielectric layer $d_0 = {}^{d_1}/_{\varepsilon_{r1}} + {}^{d_2}/_{\varepsilon_{r2}}$ | 0.037 mm |
| Surface triboelectric charge $Q$ | 100.2 nC |
| Area size of the triboelectric layer $S$ | 7.84 $cm^2$ |
| Electric energy per cycle $E_{electric}$ | 25.4809 μJ |

Combined with the volume and the mass of the as-fabricated MT-TENG (parameters given in **Table 3.1**), the volumetric power density and the gravimetric power density are 73.78 μW $cm^{-3}$ and 63.78 μW $g^{-1}$, respectively, as summarized in **Table 3.2**.

**Table 3.2** Output performance of the MT-TENG.

| **Figure-of-merit** | **Value** |
|---|---|
| Peak power density $P_{peak}$ | 2.09 W $m^{-2}$ |
| Average power density $P_{ave}$ | 32.5 mW $m^{-2}$ $Hz^{-1}$ |
| Gravimetric power density $P_m$ | 63.78 μW $g^{-1}$ |
| Volumetric power density $P_v$ | 73.78 μW $cm^{-3}$ |
| Energy conversion efficiency $\eta$ | 34.81% |

Accordingly, the energy conversion efficiency of the MT-TENG was discussed. We defined energy conversion efficiency as the ratio between the electric energy output with load and the input mechanical energy.

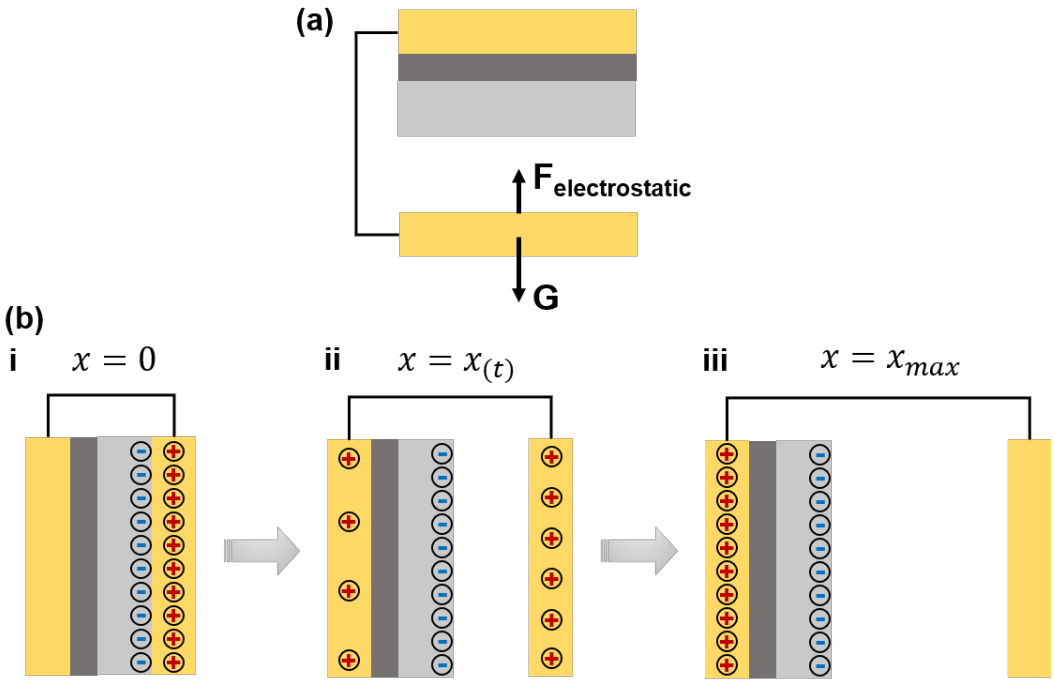


**Figure 3.8** Schematic diagrams of force state and charge transfer process during the contact-separation process. (a) Force analysis of separated electrode part. (b) Dynamic charge transfer process during the separation process.

Based on the "dynamic charge model" (**Figure 3.8**), the interfacial electrostatic force was first evaluated as:

$$F_{electrostatic\ force} = \frac{(Qd_0)^2}{2S\varepsilon_0[d_0+x]^2} \tag{3-1}$$

where $Q$ is the total transferred charges and $S$ is the surface area of electrodes. $d_0$ is defined as the effective thickness of the dielectric layer. $x$ represents the separation distance. If considering a half-cycle, taking the separation movement for an example, the whole external mechanical energy is gravitational and electrostatic potential energy. Consequently, the energy conversion efficiency ($\eta = {E_{electricity}}/{E_{mechanical}}$) could be obtained as a value of 34.81% with all the parameters listed in **Table 3.1**.

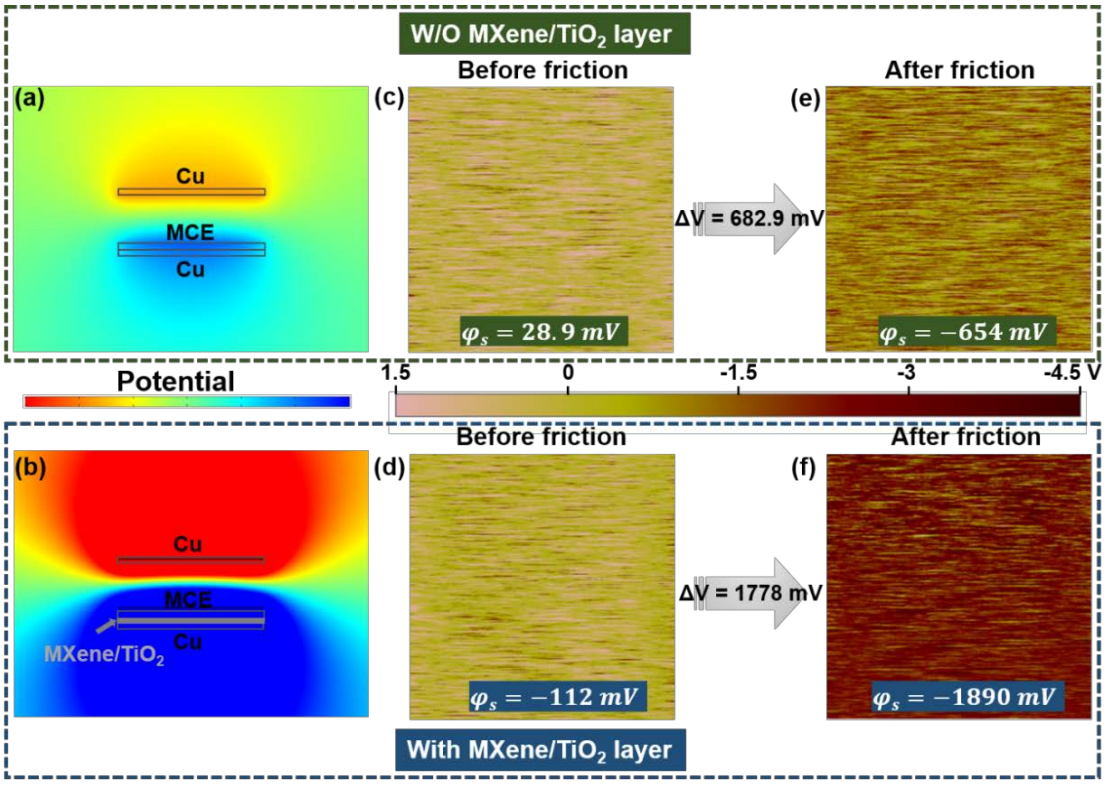


**Figure 3.9** Surface charge distribution simulation and characterization of triboelectric layers. COMSOL Multiphysics simulation results of (a) pristine TENG, (b) MT-TENG. The surface potential of MCE membrane (c) without and (d) with MXene/$TiO_2$ layer before triboelectrification. The surface potential of MCE membrane (e) without and (f) with MXene/$TiO_2$ layer after friction.

To further theoretically and systematically analyze the enhancement effect, direct surface potential simulation and testing were performed in **Figure 3.9**. In **Figure 3.9**a-b, the finite element simulation by COMSOL Multiphysics shows the potential comparison of the TENGs with or without the MXene/$TiO_2$ hybrid layer. The MT-TENG demonstrates a noticeable improvement of triboelectric potential than the pristine TENG, consistent with experimental outcomes. To further confirm TENG output enhancement by the intermediate layer, the MCE membranes without or with the MXene/$TiO_2$ hybrid layer were probed by contact potential difference (CPD)

analysis which collected KPFM images using a Ti/Pt coated silicon tip, as shown in **Figure 3.9**c-f. The CPD analysis method help measure the different contact potentials induced on the material surface.[92] **Figure 3.9**c-d illustrate the surface potential values of the MCE membranes with a size of 1*1 $cm^2$ without or with MXene/$TiO_2$ layer, presenting 28.9 and -112 mV, respectively. It could be said that before friction, the MCE membranes are approaching 0. Still, the intermediate layer makes the MCE membranes more negatively charged because the MXene/$TiO_2$ hybrid layer could cancel out the electrons' decay. After three times friction by the top Cu electrode, the surface potential values of the MCE membranes are listed in **Figure 3.9**e-f. Since the MCE membrane has greater triboelectricity than Cu, the MCE membrane would be negatively charged. The pristine MCE shows -654 mV, while the MCE membrane with the MXene/$TiO_2$ hybrid layer is almost three times larger (-1890 mV). The significant decrease of the surface potential presents that the negative charge density is promoted on the surface of the MCE membrane.

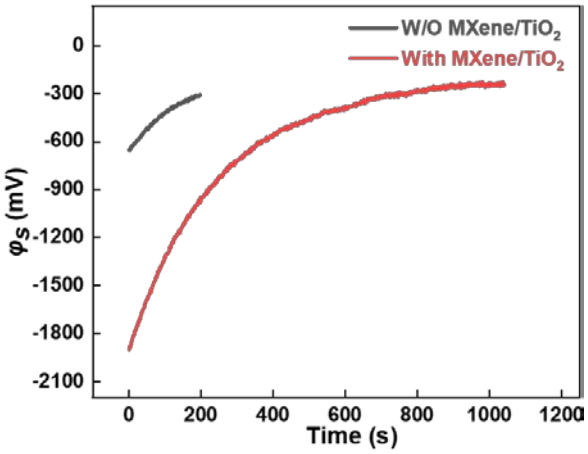


**Figure 3.10** The surface potential of MCE membranes without and with MXene/$TiO_2$ layer along with time.

The changes of MCE membranes' surface potential along with time were provided in **Figure 3.10**. The surface potential of MCE membrane with the MXene/$TiO_2$ hybrid layer spent 1042 s dropping from -1890 mV to -245 mV, and tended to a steady state. Relatively, in the case without the MXene/$TiO_2$ hybrid layer, the surface potential declined from -654 mV to -307 mV within 198 s. That could be attributed to the coupling effect of trapping and blocking impact due to the MXene/$TiO_2$ hybrid layer. The MCE membranes with intermediate layer could reach higher surface potential, and could extend the charge decay time result from the charge regulation of MXene/$TiO_2$ layer.

### 3.3.4 Enhanced Mechanism of MT-TENG

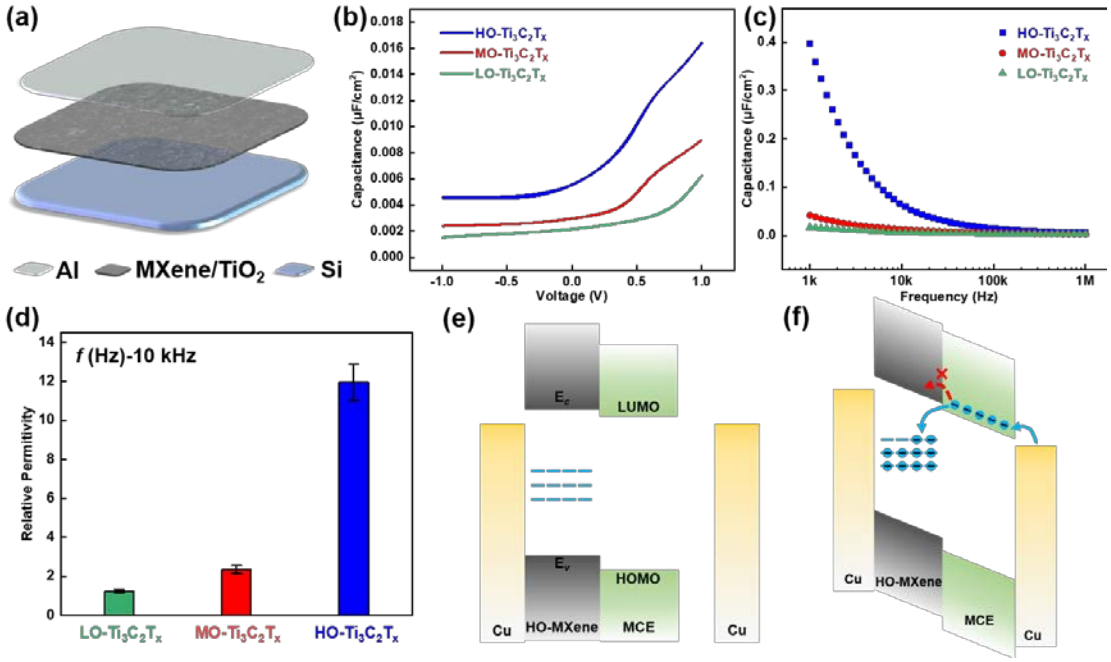


**Figure 3.11** Mechanism analysis of the electron trapping & blocking and polarization effects of the MXene/$TiO_2$ layer. (a) Illustration of the MOS device for C-V measurements. (b) C-V and (c) C-F curves of MOS devices with different oxidation degrees of MXene as the insulator layer. (d) Relative permittivity of different oxidation

degrees of MXene. Schematic energy band diagram for the MT-TENG (e) before and (f) after contact.

To further experimentally discuss the electron trapping & blocking and polarization effects in MXene/$TiO_2$ layer, a metal-oxidized MXene-semiconductor (MOS) structured device was fabricated, as shown in **Figure 3.11**. The schematic structure is in **Figure 3.11**a, where the MXene/$TiO_2$ layer works as the electron trapping & blocking layer. The electron trapping & blocking effect could be demonstrated by measuring the capacitance of the MOS device. The C-V plots with various oxidized degrees of MXene are presented in **Figure 3.11**b under dual voltage sweeps from -1 V to 1 V. The increased capacitance of MOS devices with the oxidation degree of the MXene layer illustrates the charge storage capability of $TiO_2$.[93-95] From C-F curves in **Figure 3.11**c, the capacitances show a high but gradually decreasing tendency from 1 kHz to 1 MHz, which certify the polarization effect resulting from the MXene/$TiO_2$ layer.[96-97] With the increasing oxidation degree of the MXene, the composition of $TiO_2$ gradually upgrades, thereby, increasing the relative permittivity of the hybrid layer. In theory, the increase of relative permittivity would lead to the promotion of polarization charge density according to the equation:

$$(1 - \frac{\varepsilon_0}{\varepsilon})\rho_f = -\rho_p \quad (3\text{-}2)$$

where the $\rho_f$ is free charge density and $\rho_p$ is polarized charge density. $\varepsilon_0$ and $\varepsilon$ are the relative permittivity of the air and dielectric layer, respectively. The capacitance values at 10 kHz were chosen to calculate the relative permittivity of LO-$Ti_3C_2T_x$, MO-

$Ti_3C_2T_x$ and HO-$Ti_3C_2T_x$, as depicted in **Figure 3.11**d. The relative permittivity of HO-$Ti_3C_2T_x$ is 12, also proving its high dielectric property and polarization characteristic.[77]

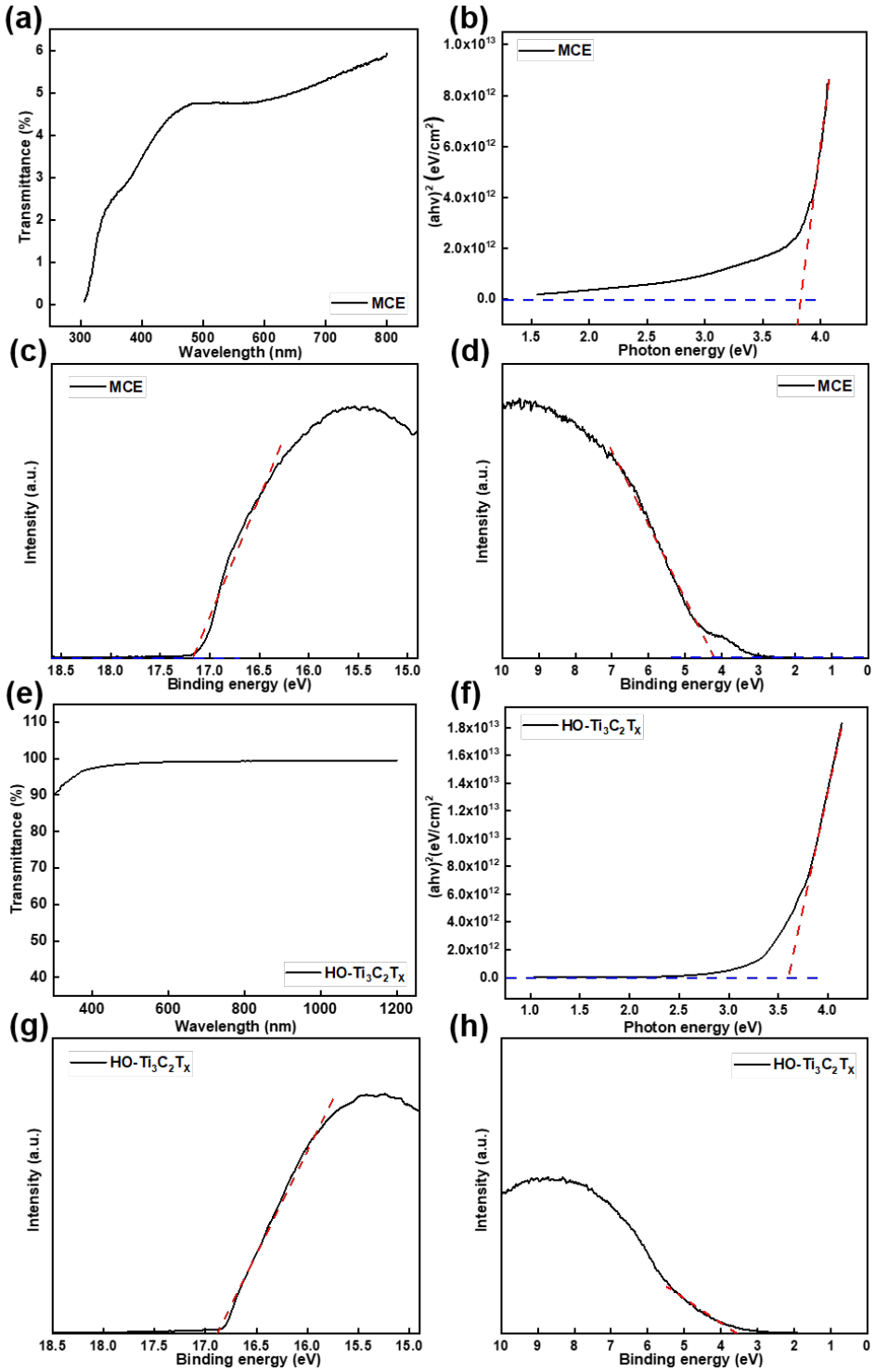


**Figure 3.12** (a) Transmittance spectra of the MCE membrane. (b) Evaluation of the $(ahv)^2$ versus $hv$ curve of the MCE membrane. (c, d) Ultraviolet photoelectron spectra

of MCE membrane. (e) Transmittance spectra of HO-$Ti_3C_2T_x$. (f) Evaluation of the $(ahv)^2$ versus $hv$ curve of HO-$Ti_3C_2T_x$. (g, h) Ultraviolet photoelectron spectra of HO-$Ti_3C_2T_x$.

Two schematic energy band diagrams before and after contact were demonstrated to further clarify the working mechanism of the performance enhancement of the surface charges, in which the positions of conduction band and valence band of the MCE and HO-$Ti_3C_2T_x$ were obtained by ultraviolet photoelectron spectra (UPS) and UV-vis tests as provided in **Figure 3.12**. As illustrated in **Figure 3.11**e, there are a large quantity of electron trap sites in the HO-$Ti_3C_2T_x$ layer due to the abundant surface terminals of the MXene and the oxygen vacancies in the $TiO_2$ nanoparticles.[96-97] After contact, as displayed in **Figure 3.11**f, two main charge migration processes would take place: (i) The interfacial electric field through the dielectric medium could cause the polarization of HO-$Ti_3C_2T_x$ layer, resulting in energy band bending, which further hinder the free electrons in HO-$Ti_3C_2T_x$ to drift to the bottom copper electrode and consequently prevent the charge recombination. (ii) The deep charge traps in HO-$Ti_3C_2T_x$ layer could capture free electrons from the MCE layer and store them inside HO-$Ti_3C_2T_x$ layer, blocking the charges from moving into the bottom Cu electrode. Therefore, the synergetic effect produced by the intermediate layer helped storing and maintaining more triboelectric charges, reducing the charge decay.

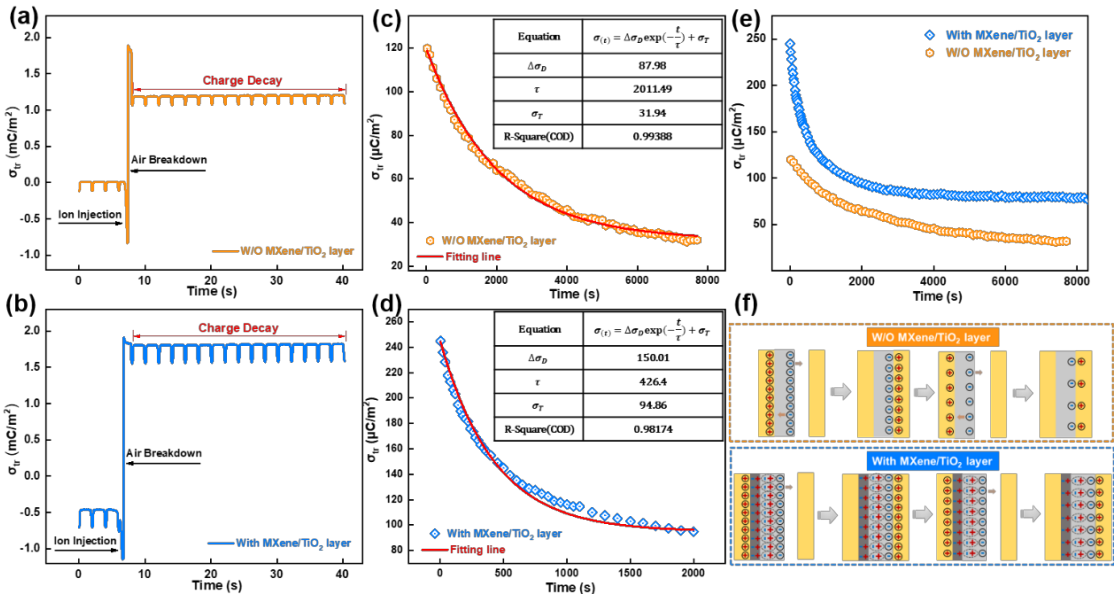


**Figure 3.13** Charge decay process comparison and charge recombination model. Surface charge density of MT-TENGs (a) without and (b) with MXene/$TiO_2$ layer showing the air breakdown occurrence by ion injection. Charge decay process and model fitting of MT-TENGs (c) without and (d) with MXene/$TiO_2$ layer after air breakdown. (e) Charge decay process comparison versus time. (f) Schematic diagram of the charge recombination model.

To compare the charge decay condition, a long-time test was conducted, and a charge recombination model was constructed, as shown in **Figure 3.13**. First of all, the surface charge density was raised to maximum saturation by ion injection method (**Figure 3.13**a-b). After the air breakdown, the surface charges on both MCE membranes would recombine with the oppositely charged particles in the air, resulting in charge decay. **Figure 3.13**c-d reveals that the beginning charge decay takes an exponential form. To clarify the attenuation characteristics, a decay equation was utilized to simulate the experimental results. It is noted that at the beginning decay process, the decayed charges are abundant and charges produced by triboelectrification could be ignored. Until

triboelectrification needs to be considered, the amount of the surface charges is defined as $Q_T$. According to the differential equation, the surface charge at a time $Q_{(t)}$ could be derived as:[33]

$$Q_{(t)} = \Delta Q_D \exp\left(-\frac{t}{\tau}\right) + Q_T \quad (3\text{-}3)$$

Here, $Q_I$ means the amount of the initial charges after air breakdown. Then, the total decayed charges from $Q_I$ to $Q_T$ is defined as $\Delta Q_D$. $\tau$ is the lifetime of the surface charges, and $1/\tau$ stands for the charge combination per unit time. Accordingly, considering the surface area, the decay equation could be expressed in the form of charge density as:

$$\sigma_{(t)} = \Delta\sigma_D \exp\left(-\frac{t}{\tau}\right) + \sigma_T \quad (3\text{-}4)$$

Therefore, this decay equation was used to simulate the experimental curves in **Figure 3.13**c-d, showing the fit linearity of over 98%. The values of $\Delta\sigma_D$, $\tau$ and $\sigma_T$ could be obtained in the control groups, as listed in Tables inset. The most notable values of $\sigma_T$ present the reserved charge density after the beginning rapid charge decay. The MCE membrane with MXene/$TiO_2$ layer exhibits three times greater remained charge density than that of the pristine TENG. **Figure 3.13**e demonstrates the charge decay in around 8000 s test, in which the pristine TENG presents a continuous decay tendency from 120 to 32 μC/$m^2$. By contrast, the charge density of MT-TENG reaches 245 μC/$m^2$ initially, and gives a sharp decline at the beginning. Then the charge density remains at 80 μC/$m^2$, which could be concerned as reaching a dynamic equilibrium. A schematic charge recombination model was illustrated in **Figure 3.13**f. When abundant charges

exist on the MCE surfaces, these charges would diffuse into the air or recombine with the induced charges on the electrode. If the MXene/$TiO_2$ layer is introduced, the triboelectric charges would be trapped and blocked, consequently cutting back the charge loss.

## 3.4 Conclusion

In summary, a high-performance TENG was developed with the structural design of an intermediate layer. The intermediate layer consists of MXene/$TiO_2$ hybrid film, which functions as an electron trapping & blocking layer with a polarization effect. Through the synergetic effect, the triboelectric charges are regulated to store in the dielectric part and also produce more induced charges on electrode. The as-fabricated MT-TENG shows noticeable performance (128 $\mu C/m^2$, 73.78 $\mu W/m^3$, 63.78 $\mu W/g$) with enhancement mechanism investigations including theoretical simulations, physical characterizations and electrical measurements. Besides, a method of calculating the energy conversion efficiency was introduced to consider efficient mechanical energy input and electricity output, with a result of 34.81%. Furthermore, through the charge regulation, the triboelectric charges present an extended residence time and remain at 80 $\mu C/m^2$ on the tribo-material surface. It paves a new approach to reduce the charge diffusion, and provide a promising way to promote the stability and repeatability of TENGs' output performance for energy harvesting and self-powered sensing.

# CHAPTER 4 Theoretical Boundary and Optimization Methodology

## 4.1 Background

With the advent of Internet of Things (IoTs), the distributed multi-functional sensing network, known as a crucial node for the exchange of information between intelligent equipment and control terminals, is becoming the basis of the fourth intelligent industrial revolution.[55, 98] Considering the mobility power supply requirements of enormous discrete sensors, developing self-powered methods succeeds a critical strategy.[99-100] Triboelectric nanogenerators (TENGs) show unique advantages in collecting irregular mechanical energy in environments, such as mechanical vibration, human motion and ocean waves, hence attracting widespread attention regarding their applications in wearable electronics and wireless sensors.[3-4, 68]

As energy harvesters, energy output and energy conversion efficiency of TENGs are generating widespread interests.[101-102] Theoretically, energy output is quadratically related to the surface charge density.[48] Therefore, tons of works focus on enhancing the surface charge density of TENGs, including surface functionalization[34], surface polarization[70, 72] and intermediate layer addition[40, 46]. And the saturated charge density could be achieved through corona discharging[103-104], ionized air injection[33, 41], charge pumping[105-106], and external/self-charge excitation strategies[47, 107] in experiments. Nevertheless, the theoretical boundary of surface charge density and energy output is still ambiguous so that the limitation of enhancement is still insufficient. In previous work, Wang *et al*. discussed analytical mathematical derivation for the maximum

surface charge density of contact-separation TENGs with single dielectric layer.[33] Zi *et al*. proposed the theoretical and experimental methods of achieving maximum effective energy output of TENGs based on the *V-Q* curves.[48-49, 108] Therefore, comprehensive and systematic theoretical calculation methods of maximum surface charge density and effective energy output deserve to be provided for contact-separation TENGs containing all different structures.

In this chapter, the theoretical boundary of surface charge density and energy output of contact-separation TENGs have been mathematically derived and analyzed. Firstly, an optimization model of surface charge density was set up by considering Maxwell's equations and Paschen's law. Through the derivation of the limitation equation, the theoretical mathematical relations of surface charge density were deduced with respect to structural and material factors of TENGs. Secondly, a mathematical calculation method of maximum effective energy output of TENGs was proposed on the basis of *V-Q* curves from the previous work. Furthermore, theoretical simulation was developed about the maximum surface charge density, maximum effective energy output and figure of merit to evaluate the TENG's performance. Here, the structural parameters (separation distance, device size) and material parameters (dielectric layer thickness, relative permittivity) were thoroughly evaluated.

## 4.2 Simulation Methods

The simulation process includes open-circuit and short-circuit conditions by COMSOL electrostatic modules. The parameters for model construction were given in **Table 4.1**

and **Table 4.2**.

**Table 4.1** COMSOL multiphysics simulation parameters for TENGs with different thickness of dielectric layers.

| | | | | | |
|---|---|---|---|---|---|
| Maximum separation distance $x_{max}$ (cm) | | | | | 2 |
| Area size of the triboelectric layer $S$ ($mm^2$) | | | | | 5*5 |
| Relative permittivity of silicone rubber $\varepsilon_{r1}$ | | | | | 11.7 |
| Relative permittivity of nylon $\varepsilon_{r2}$ | | | | | 4 |
| Thickness $d_i$ (μm) | 10 | 20 | 40 | 80 | 160 |
| Maximum charge density $\sigma_m$ ($\mu C/m^2$) | 880.48 | 529.61 | 341.72 | 235.88 | 172.67 |

In open-circuit condition, the floating potential of two electrodes should be set as 0. Surface electric potential distribution could be achieved and line average values of electric potential could be exported. In short-circuit condition, the floating potential of electrodes should be disabled and two electrodes were both set to ground. The data of transferred charges could be obtained by the line integration of the surface charge density of one electrode.

**Table 4.2** COMSOL multiphysics simulation parameters for TENGs with different relative permittivity of dielectric layers.

| | |
|---|---|
| Maximum separation distance $x_{max}$ (cm) | 2 |
| Area size of the triboelectric layer $S$ ($mm^2$) | 5*5 |

| | | | | | |
|---|---|---|---|---|---|
| Thickness of the negative triboelectric layer $d_1$ (μm) | | | | | 10 |
| Thickness of the positive triboelectric layer $d_2$ (μm) | | | | | 0 |
| Relative permittivity $\varepsilon_{r1}$ | 2.1 (FEP) | 3.5 (PET) | 4 (Kapton) | 7 (PVDF) | 11.7 (Silicone) |
| Maximum charge density $\sigma_m$ (μC/m$^2$) | 675.19 | 999.93 | 1114.32 | 1793.85 | 2849.95 |

## 4.3 Results and Discussion

### 4.3.1 Limiting Factors for Surface Charge Density

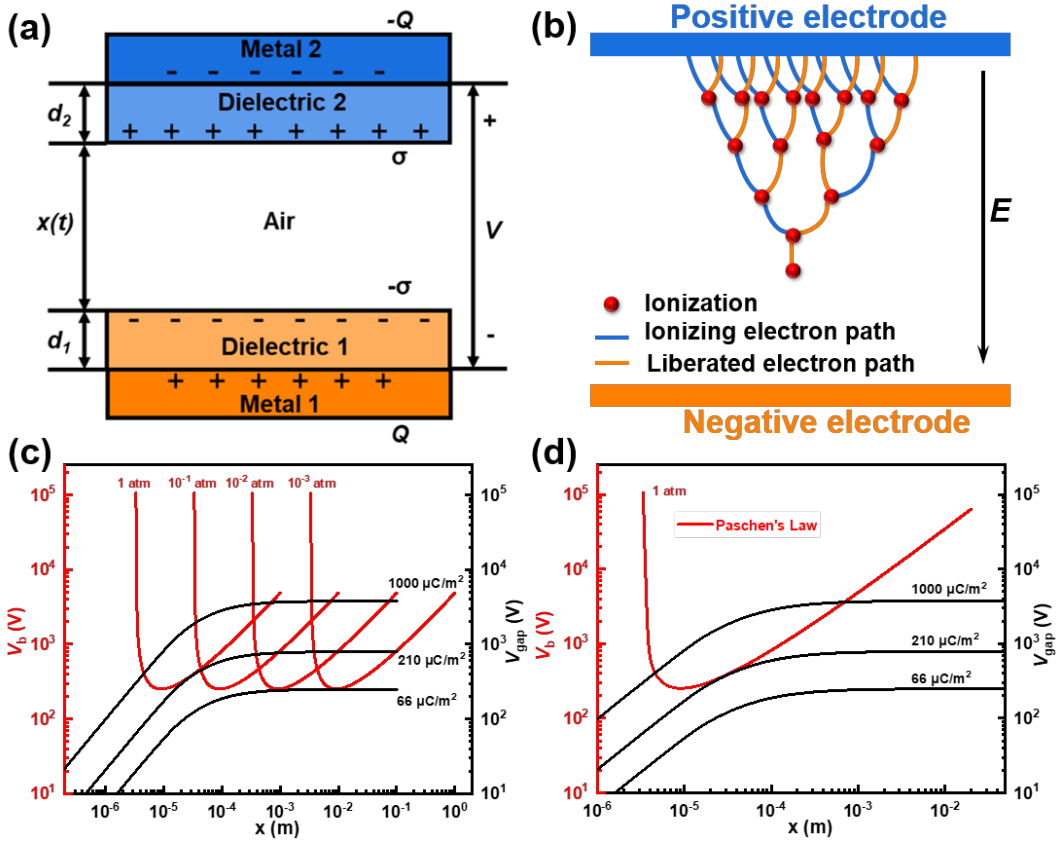


**Figure 4.1** Limiting factors for surface charge density. (a) Theoretical model for dielectric-dielectric contact-separation mode TENG. (b) Schematic diagram of Townsend discharge caused by avalanche breakdown. (c) Air breakdown voltage based on the Paschen's law under distinct atmospheric pressure and the gap voltages of TENGs with various surface charge densities. (d) Comparison between air breakdown voltage under 1 atm and gap voltages of TENGs with various surface charge densities

versus separation distance.

According to the triboelectric pairs, the contact-separation mode TENGs could be categorized into conductor-dielectric mode and dielectric-dielectric mode.[27] To universally and comprehensively analyze the contact-separation mode TENGs, a theoretical model for dielectric-dielectric mode TENGs was built, as illustrated in Figure 4.1a. Two dielectric materials were utilized as the triboelectric layers, with the thickness of $d_1$ and $d_2$ and relative permittivity of $\varepsilon_1$ and $\varepsilon_2$, respectively.[24] Therefrom, the conductor-dielectric mode could be included, supposing that the thickness of upper dielectric layer is set to 0. Based on coupling effect of contact electrification and electrostatic induction, equivalent heterogeneous charge density ($-\sigma$ and $\sigma$) would be distributed on the surface of the triboelectric pair, and thus induced charges would occur on the corresponding electrodes ($Q$ and $-Q$). The separation distance ($x$) changes with the movement of TENG in the air. As the size of the triboelectric pair is several orders of magnitude larger than the thickness of dielectrics in experiments, it is reasonable to regard the triboelectric layers as infinitely large plates. Under the premise of reasonably ignoring edge effect, the $V-Q-x$ relationship could be unified as the following equation based on the classical electrodynamics:

$$\Delta V_E = -\frac{\sigma_x}{\varepsilon_0}\left(\frac{d_1}{\varepsilon_{r1}} + \frac{d_2}{\varepsilon_{r2}} + x\right) + \frac{\sigma_0 x}{\varepsilon_0} \tag{4-1}$$

where $\sigma_0$ is the surface charge density of dielectric layer; $\sigma_x$ is the induced charge density on the electrodes and $\varepsilon_0$ presents the vacuum permittivity ($8.85 \times 10^{-12}$ F m$^{-1}$). In the short-circuit condition, the voltage of the air gap could be derived as followed:

$$V_{gap} = \frac{\sigma_0 d_0}{\varepsilon_0 (x + d_0)} x \quad (4\text{-}2)$$

where $d_0$ represents the effective thickness constant and could be expressed as $d_0 = \frac{d_1}{\varepsilon_{r1}} + \frac{d_2}{\varepsilon_{r2}}$. There are several discharging effects that limit the TENGs' performance, including air breakdown, electrons drift, diffusion and charge recombination.[46, 105, 108-110] Unlike the relatively long time of other effects, air breakdown results in immediate discharging and sharply decreasing the surface charge of TENGs. It would occur once the voltage of the air gap between the two electrodes is large enough. This air breakdown follows Paschen's law based on the Townsend discharge, which is a phenomenon where the avalanche breakdown of air leads to the occurrence of ionic conductance in air.[41] Avalanche breakdown could be demonstrated as shown in **Figure 4.1**b, where free electrons are accelerated in an electrostatic field and collide with air molecules, resulting in a chain effect of additional free electrons.[111-112] The red lines in **Figure 4.1**c present the air breakdown voltage threshold based on Paschen's law under different atmospheric pressure. With the decreasing atmospheric pressure, the curves exhibit a right shift arising, which means higher performance could be achieved under lower atmospheric pressure. Considering most of TENGs work at standard atmospheric pressure, Paschen curve under 1 atm and the air gap voltages (black lines) with various surface charge density are provided in **Figure 4.1**d. The air gap voltage is enhanced with the increasing surface charge density. Provided that the air gap voltages exceed the red line, air breakdown would be bound to occur in the air gap.

### 4.3.2 Theoretical Boundary of Maximum Surface Charge Density

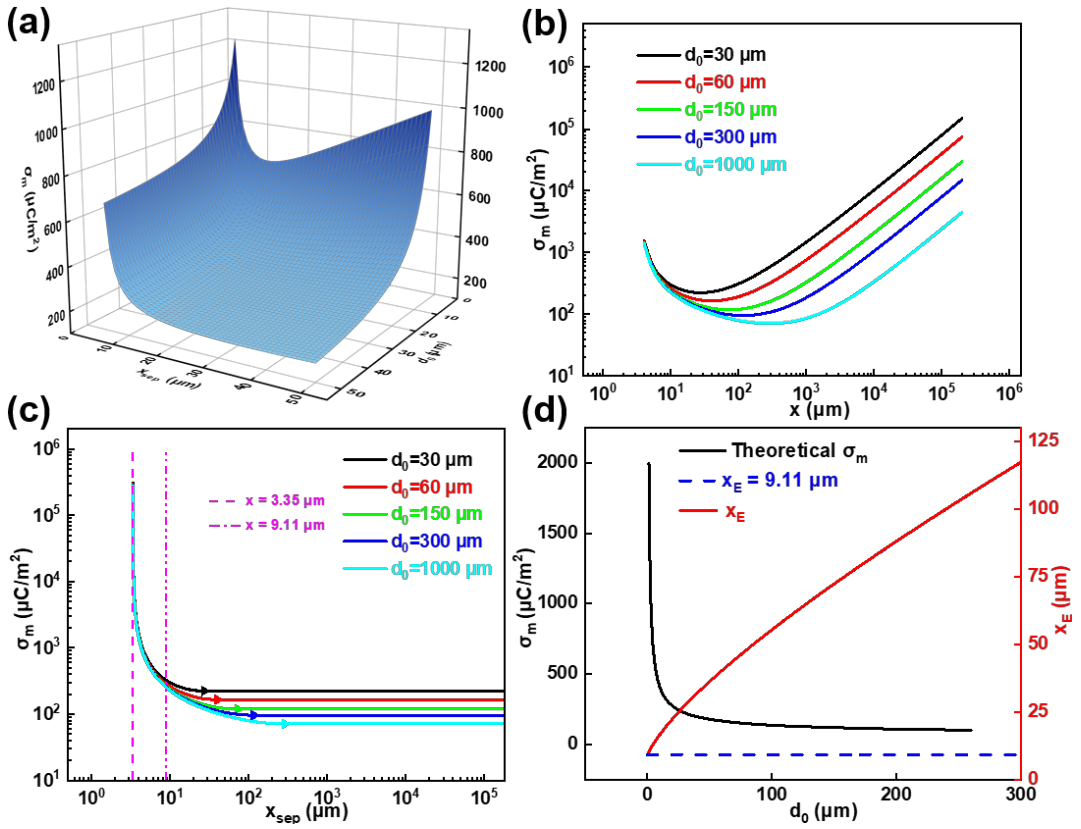


**Figure 4.2** Theoretical analysis of maximum surface charge density. (a) Relationship among maximum surface charge density, separation distance and effective thickness constant of dielectric layers. Theoretical maximum surface charge density with various effective thickness constant versus separation distance (b) without air breakdown or (c) considering air breakdown. (d) Theoretical maximum surface charge density and inflection point value along with the effective thickness constant.

Taken the Paschen's law as the theoretical boundary, the limitation equation of surface charge density could be achieved as:

$$\sigma_{0max} = \left[\frac{BP\varepsilon_0(x+d_0)}{(\ln(Px)+C)d_0}\right]_{min} \tag{4-3}$$

where $P$ is the standard atmospheric pressure of 101325 Pa and constants $B$ and $C$ equal to 273.78 V $Pa^{-1}$ $m^{-1}$ and 1.08, respectively, both of which depend on the air

composition and pressure.[112] The domain area of $x$ should be larger than 3.35 μm, considering the separation distance under 3.35 μm is smaller than the electron mean free path, which is insufficient for avalanche breakdown, hence inapplicable for Paschen's Law. Therefore, some distance should be provided for free electrons acceleration and the chain reaction as illustrated in **Figure 4.1**b. From the limitation equation (3), the maximum surface charge density is affected by the separation distance and effective thickness constant of dielectric layers. **Figure 4.2a** reveals the three-dimension diagram about the $\sigma_m - d_0 - x$ relationship. The tendency initially indicates that shorter separation distance and smaller effective thickness constant would contribute to a higher surface charge density. **Figure 4.2**b shows smaller $d_0$ could help achieve higher surface charge density, in which five distinct values of $d_0$ were specified. It also demonstrates that the surface charge density decreases with the separation distance, followed by an increasing trend, which means the minimum value of the right function part of the equation (3) exists. To ascertain the maximum charge density theoretically, the variable part of the limitation equation was defined as a function $f(x, d_1, d_2)$:

$$f(x, d_1, d_2) = \frac{x + \frac{d_1}{\varepsilon_{r1}} + \frac{d_2}{\varepsilon_{r2}}}{\left(\frac{d_1}{\varepsilon_{r1}} + \frac{d_2}{\varepsilon_{r2}}\right)[\ln(Px) + C]} \tag{4-4}$$

Thus, $\sigma_m = BP\varepsilon_0 f(x, d_1, d_2)_{min}$

Take the partial derivatives for $x$:

$$\frac{\partial f}{\partial x} = \frac{[\ln(Px) + C] - \frac{1}{x}\left(x + \frac{d_1}{\varepsilon_{r1}} + \frac{d_2}{\varepsilon_{r2}}\right)}{\left(\frac{d_1}{\varepsilon_{r1}} + \frac{d_2}{\varepsilon_{r2}}\right)[\ln(Px) + C]^2} \tag{4-5}$$

Let $\frac{\partial f}{\partial x} = 0$,

then $$[\ln(Px) + C] - \frac{1}{x}(x + \frac{d_1}{\varepsilon_{r1}} + \frac{d_2}{\varepsilon_{r2}}) = 0 \quad (4\text{-}6)$$

If $x = x_E$ implies $\frac{\partial f}{\partial x} = 0$,

then $$d_0 = x_E[\ln(Px_E) + C - 1] \quad (4\text{-}7)$$

Since $d_0 > 0$ and $x_E > \frac{e^{1-C}}{P} = 9.11\ \mu m$,

We have $$f(x)_{min} = \begin{cases} f(x), & x \in (3.34,\ 9.11) \\ f(x_E), & x \in (9.11,\ \infty) \end{cases} \quad (4\text{-}8)$$

Note that the separation distance $x$ is at cm scale. Thus $f(x)_{min} = f(x_E)$.

Therefore, $d_0 = x_E[\ln(Px_E) + C - 1]$ implies $\ln(Px) + C = \frac{d_0}{x_E} + 1$.

Thus, $$\sigma_{0max} = \left\{\frac{BP\varepsilon_0(x+d_0)}{(\ln(Px)+C)d_0}\right\} min = \frac{BP\varepsilon_0(x_E+d_0)}{(\frac{d_0}{x_E}+1)d_0} = \frac{BP\varepsilon_0}{d_0/x_E} = \frac{BP\varepsilon_0}{\ln(Px_E)+C-1} \quad (4\text{-}9)$$

Through investigating the partial differentiation and derivation for $x$, $d_1$ and $d_2$ respectively, the relationship between the $x_{sep}$ and the $\sigma_m$ could be concluded as:

$$\sigma_m = \begin{cases} \frac{BP\varepsilon_0(x_{sep}+d_0)}{(\ln(Px_{sep})+C)d_0}, & x_{sep} \in (3.35\ \mu m,\ x_E) \\ \frac{BP\varepsilon_0}{\ln(Px_E)+C-1}, & x_{sep} \in (x_E,\ \infty) \end{cases} \quad (4\text{-}10)$$

$x_E$ in equation (4-10) is the critical separation distance at which air breakdown begins to occur, and its value depends on the effective thickness constant of the dielectric layers. The mathematical expressions reveal that when the separation distance is between 3.35 μm and $x_E$, the maximum charge density rests with the value of separation distance. As soon as the separation distance exceeds $x_E$, the maximum charge density would reach a constant depending on $x_E$ due to the air breakdown. As shown in **Figure 4.2**c, when separation distance is large while close to 3.35 μm, the value of $\sigma_m$ is large as the breakdown voltage is considerable for gap voltage $V_{gap}$ to acquire at that time.

Besides, the theoretical tendency of $\sigma_m$ with various effective thickness constant also reflect the conclusion of equation (4-10). The dotted line means $d_0$ could be meaningful ($d_0 > 0$), only if $x_E > 9.11\ \mu m$. Triangle symbols in **Figure 4.2**c indicate the threshold separation distances $x_E$ of air breakdown, namely when the minimum values of maximum charge density $\sigma_m$ are firstly reached. Before the critical points, the values of $\sigma_m$ reduce with the gradually increasing $x_{sep}$. After the critical points, $\sigma_m$ reaches a saturated value which could be calculated by equation (4-10), and that constant is the theoretical boundary of surface charge density under the specific structural models. In addition, take the partial derivatives for $d_1$ and $d_2$ respectively:

$$\frac{\partial f}{\partial d_1} = -\frac{1}{\varepsilon_{r1}} \frac{x}{(\frac{d_1}{\varepsilon_{r2}} + \frac{d_2}{\varepsilon_{r2}})^2 [\ln(Px) + C]} \tag{4-11}$$

$$\frac{\partial f}{\partial d_2} = -\frac{1}{\varepsilon_{r2}} \frac{x}{(\frac{d_1}{\varepsilon_{r2}} + \frac{d_2}{\varepsilon_{r2}})^2 [\ln(Px) + C]} \tag{4-12}$$

Since the partial derivatives for $d_1$ and $d_2$ are both negative, it indicates the function $f(x, d_1, d_2)$ monotonically decreases with $d_0$.

If $x = x_E$ implies $\frac{\partial f}{\partial x} = 0$, we have $d_0 = x_E[\ln(Px_E) + C - 1]$.

From equation (4-9), we get $\sigma_m = \frac{BP\varepsilon_0}{\ln(Px_E) + C - 1}$

So, $$\ln(Px_E) = \frac{BP\varepsilon_0}{\sigma_m} + 1 - C \tag{4-13}$$

Namely, $$x_E = \frac{1}{P} \exp\left(\frac{BP\varepsilon_0}{\sigma_m} + 1 - C\right) \tag{4-14}$$

Take it into the formula $d_0 = x_E[\ln(Px_E) + C - 1]$,

and the relationship between $d_0$ and $\sigma_m$ could be derived as:

$$d_0 = \exp(\frac{BP\varepsilon_0}{\sigma_m} + \ln\frac{B\varepsilon_0}{\sigma_m} + 1 - C) \tag{4-15}$$

From this equation, $\sigma_m$ is signified to be monotonically decreasing with $d_0$. It is also

remarkable in **Figure 4.2**d that larger $d_0$ would bring about a lower $\sigma_m$. Moreover, the value of $x_E$ could be clarified with the determined $d_0$, as the red line shown in **Figure 4.2**d. This critical separation distance is usually in the micrometer range, which is much smaller than the separation distance in the practical experiments. To be brief, through the derivation of the limitation equation, the theoretical boundary of $\sigma_m$ was deduced, which reveals the mathematical relations between $\sigma_m$ with $x_{sep}$ and $d_0$ of TENGs. It also provides a theory-based optimization for the enhancement of TENGs' performance, namely reducing $d_0$ as much as possible on the premise that breakdown is supposed to be avoided.

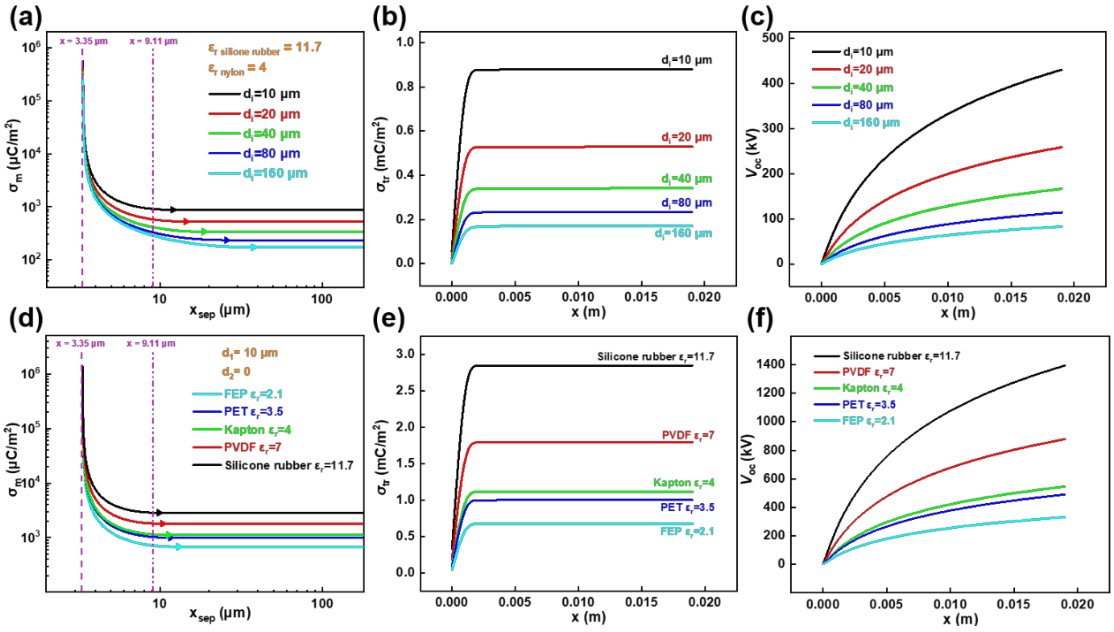


**Figure 4.3** Theoretical analysis of effective thickness constant. (a) Relationship between maximum surface charge density and the thickness of dielectric layers. The calculated output characteristics with different thicknesses of dielectric layers about (b) real-time transferred charge density–time curves and (c) real-time open-circuit voltage–time curves by COMSOL Multiphysics simulation. (d) Relationship between maximum surface charge density and the relative permittivity of dielectric layers. The calculated

output characteristics with different relative permittivity of dielectric layers about (e) real-time transferred charge density–time curves and (f) real-time open-circuit voltage–time curves by COMSOL multiphysics simulation.

To further prospect the relationship between the maximum surface charge density and effective thickness constant theoretically, the parameters including thickness and relative permittivity of the dielectric layers were discussed, as illustrated in **Figure 4.3**. First of all, silicone rubber ($\varepsilon_{r1} = 11.7$) and nylon ($\varepsilon_{r2} = 4$) were utilized as the triboelectric pair to construct the TENG simulation models. The thickness of both the triboelectric pair was regulated from 10 μm to 160 μm to testify the effect of thickness on the maximum surface charge density. **Figure 4.3**a reveals that the thinner dielectric layer leads to a higher surface charge density. COMSOL Multiphysics was utilized to simulate the surface potential distribution, real-time transferred charge–time and open-circuit voltage–time characteristic curves. The TENG simulation models were set up with maximum separation distance $x_{max}$ of 2 cm and area size of the triboelectric layer $S$ of 5×5 mm$^2$. For all the models, the stipulated values of surface charge density on the triboelectric layers are the calculated maximum surface charge density by equation (4-10), as provided in **Table 4.1**. From the derivatives of COMSOL outcomes, the charge density–time curves (**Figure 4.3**) show that smaller thickness of dielectric layer brings higher surface charge density. Moreover, it is obvious that most of the charges finish transferring as the separation distance reaches about $10d_0$.

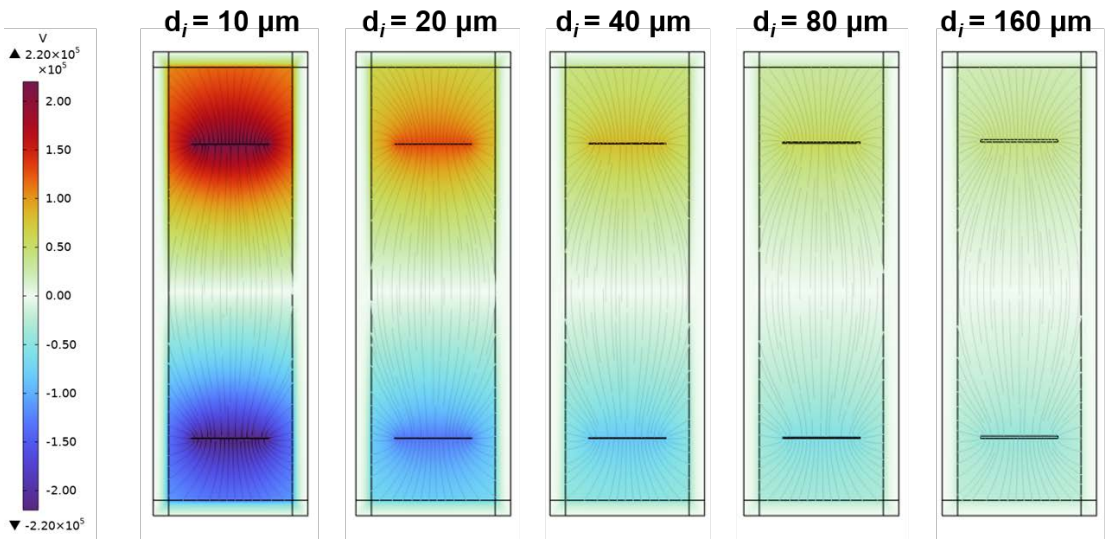


**Figure 4.4** Surface potential distribution simulation by COMSOL multiphysics simulation with different thicknesses of dielectric layers.

From the surface potential distribution outcomes in **Figure 4.4** of all the models, it notes that model with thinner dielectric layers presents higher surface potential. Equally, the real-time open-circuit voltage–time curves also indicate the model with 10 μm achieves the superior open-circuit voltage output. As the optimization methodology for enhancement of maximum surface charge density is thickness reduction, the optimal way is to make $d_2$ equal to 0, which becomes a conductor-dielectric mode. Therefore, simplified TENG simulation models with $d_1$ and $d_2$ equal to 10 μm and 0, respectively were constructed. To analyze the effect of the dielectric layer's material factor (relative permittivity), five common dielectric layers including fluorinated ethylene propylene (FEP), polyethylene glycol terephthalate (PET), Kapton, polyvinylidene difluoride (PVDF) and silicone rubber were utilized for simulation. **Figure 4.3**d demonstrates the theoretical values of the maximum surface charge density of these five models by equation (4). It reveals dielectric material with higher relative

permittivity could make contributions to an enhanced maximized surface charge density. The TENG model with 10 μm silicone rubber presents the highest maximum surface charge density of 2.85 mC/m$^2$. As such, based on the parameters in Table S2, the transferred charges simulated by COMSOL in **Figure 4.3**e also testify higher relative permittivity is preferable.

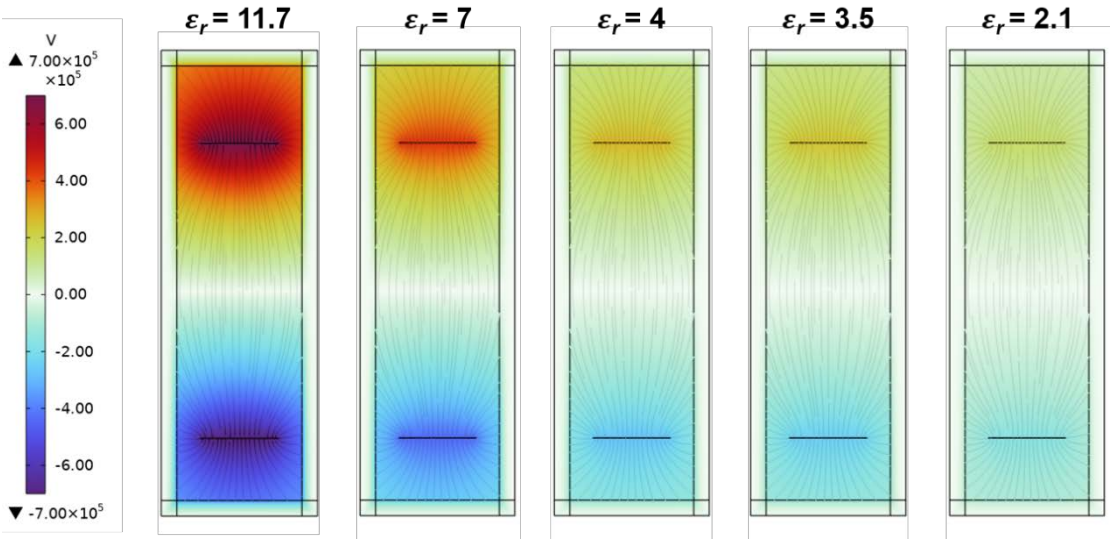


**Figure 4.5** Surface potential distribution simulation by COMSOL multiphysics simulation with different relative permittivity of dielectric layers.

Moreover, **Figure 4.5** and **Figure 4.3**f illustrate the comparison of surface potential distribution and real-time voltage–time curves. Both of them indicate that silicone rubber shows an advantage among others due to its highest relative permittivity. Therefore, to achieve higher surface charge density, the thickness of dielectric layers should be reduced without causing material breakdown, and it is better to utilized one electrode to work as the positively triboelectric layer. Besides, the relative permittivity of dielectric layer should be increased, which could be accomplished by preparing dielectric layer with high permittivity or doping with high dielectric constant particles.

### 4.3.3 Theoretical Boundary of Maximum Energy Output

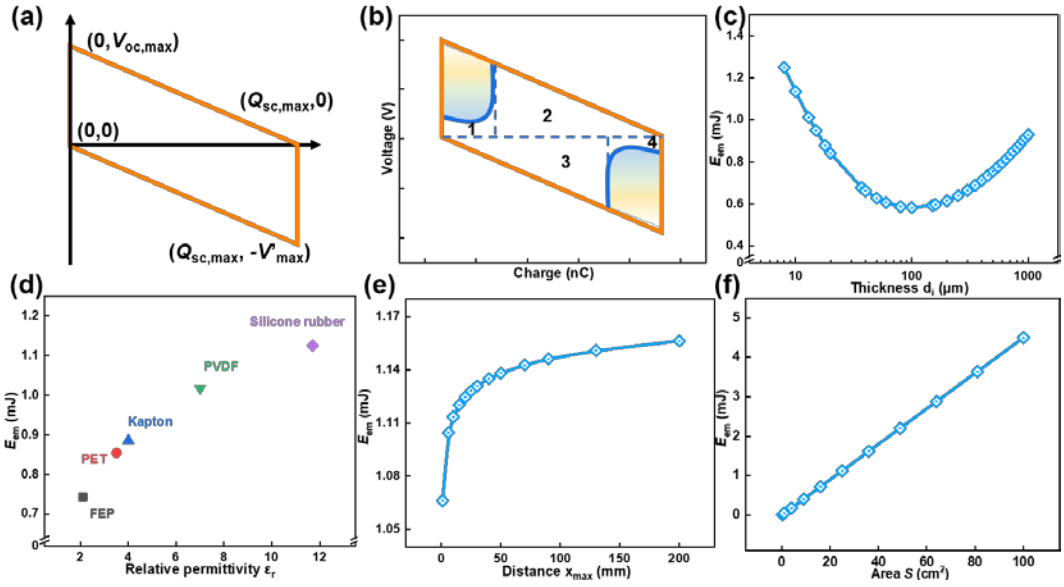


**Figure 4.6** Theoretical analysis of the effective maximized energy output. Schematic diagram of a maximized energy output cycle (a) without air breakdown, (b) considering air breakdown. The effective maximized energy output $E_{em}$ versus (c) thickness of dielectric layers, (d) relative permittivity of dielectric layers, (e) maximized separation distance, and (f) area size of the dielectric layers.

**Figure 4.6**a illustrates the V-Q relationship for a whole contact and separation cycle with four definite vertex coordinates without air breakdown consideration, where the energy output could be calculated by the integral area of V-Q closed curves.[48] Once the restriction by the air breakdown voltage is taken into consideration, namely the color gradient sections specified in **Figure 4.6**b, the maximized effective energy per cycle will be shrunk into the labelled region 1, 2, 3 and 4.[28, 49] The analytical expression for the maximized effective energy output of the first separation process $E_{em,upper}$, namely the labelled region 1 and 2, can be derived as:

$$E_{em,upper} = \int_{Q_{ori\_p}}^{Q_{sc1}} \left( \frac{BP\frac{d_0 Q_{sc}}{S\sigma - Q_{sc}}}{\ln(P\frac{d_0 Q_{sc}}{S\sigma - Q_{sc}}) + C} \right) dQ_{sc} + \int_{Q_{sc1}}^{Q_{sc,max}} \left( -\frac{V_{oc,max}}{Q_{sc,max}} Q_{sc} + V_{oc,max} \right) dQ_{sc} \quad (4\text{-}16)$$

in which constants $B$, $P$ and $C$ have been assigned their corresponding values in **equation (4-3)**. $Q_{\mathrm{ori\_p}}$ represents the transfer charge at initial displacement which is equal to 3.35 μm. $Q_{\mathrm{sc1}}$ is the horizontal coordinate of the intersection point between the air breakdown voltage and declined line, which can be derived based on the following equation:

$$\frac{BP\frac{d_0 Q_{\mathrm{sc}}}{S\sigma - Q_{\mathrm{sc}}}}{\ln(P\frac{d_0 Q_{\mathrm{sc}}}{S\sigma - Q_{\mathrm{sc}}})+C} = -\frac{V_{\mathrm{oc,max}}}{Q_{\mathrm{sc,max}}} Q_{\mathrm{sc}} + V_{\mathrm{oc,max}} \tag{4-17}$$

Therefore, to further investigate relationship between $E_{em,upper}$ and separation distance $x$, based on the relation between $Q_{\mathrm{sc}}$ and $x$, the $E_{em,upper}$ can be expressed as:

$$E_{em,upper} = \int_{x_{ori\_p}}^{x_1} \left(\frac{BPx}{\ln(Px)+C}\right)\left(\frac{S\sigma d_0}{(d_0+x)^2}\right) dx + \int_{x_1}^{x_{max}} \left(-\frac{V_{\mathrm{oc,max}}}{Q_{\mathrm{sc,max}}}\left(\frac{S\sigma x}{d_0+x}\right) + V_{\mathrm{oc,max}}\right)\left(\frac{S\sigma d_0}{(d_0+x)^2}\right) dx \tag{4-18}$$

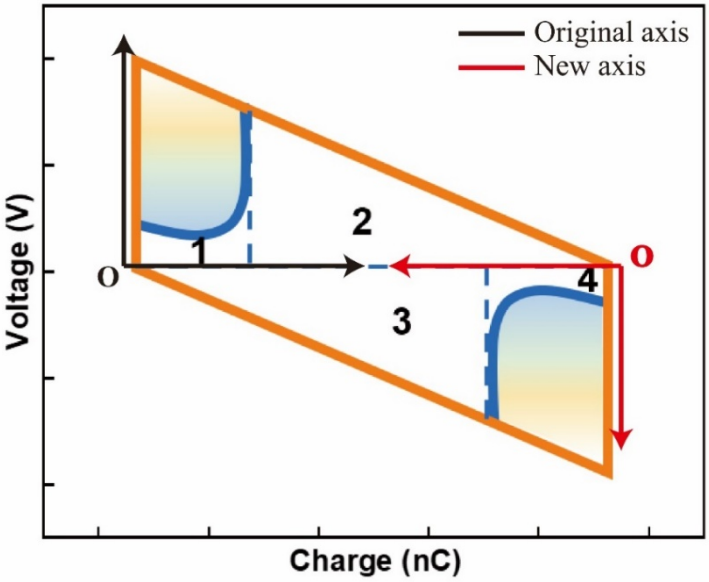


**Figure 4.7** Original and new axis generated for the convenience of evaluating upper restricted area and lower restricted area accordingly.

Similarly, for the maximized effective energy output of the first returning process $E_{em,below}$, namely the labelled region 3 and 4, a new coordinate (**Figure 4.7**) was rebuilt

with reversed coordinates direction and varied origin, then the $E_{em,below}$ can be derived as:

$$E_{em,below} = \int_{x_{ori\_p}}^{x_2} \left(\frac{BPx}{\ln(Px)+C}\right)\left(\frac{S\sigma \mathrm{d}_0}{(\mathrm{d}_0+x)^2}\right)dx + \int_{x_2}^{x_{max}} \left(-\frac{V'_{\max}}{Q_{\mathrm{sc,max}}}\left(\frac{S\sigma x}{\mathrm{d}_0+x}\right) + V'_{\max}\right)\left(\frac{S\sigma \mathrm{d}_0}{(\mathrm{d}_0+x)^2}\right)dx \quad (4\text{-}19)$$

Therefore, the total maximum effective energy output $E_{em}$ can be expressed as:

$$E_{em} = E_{em,upper} + E_{em,below} \quad (4\text{-}20)$$

Once the expression for the maximized effective energy output $E_{em}$ is determined, the theoretical relationship between the maximized effective energy output and the thickness of dielectric layers, the materials' internal parameter relative permittivity, the maximum separation distance and the contact area could be further explored, as demonstrated in **Figure 4.6**c-f. **Figure 4.6**c reveals the theoretical tendency of first decreasing and then increasing of the maximized effective energy output $E_{em}$ by varying the thickness $d_i$ from 8 to 1000 μm. From four definite vertex coordinates of $E_{em}$, $V_{\mathrm{oc,max}}$ and $Q_{\mathrm{sc,max}}$ would decrease with the increasing thickness $d_i$, but $V'_{\max}$ depends. Albeit a thicker thickness may lead to superior maximized effective energy output performance, thicker dielectric layers would reduce the triboelectric charge density due to charge recombination with the intrinsic carriers in materials.[46] Accordingly, a thinner thickness is preferred, but it still should be considered for the material breakdown.[46] To analyze the effect of the dielectric layer's material factor (relative permittivity $\varepsilon_{ri}$), five common dielectric layers including FEP, PET, Kapton, PVDF and silicone rubber were applied for the comparison. As illustrated in **Figure 4.6**d, it is explicit that a higher relative permittivity would result in an improved

maximized effective energy output performance up to 1.12 mJ in silicone rubber ($\varepsilon_r = 11.7$) condition. Furthermore, **Figure 4.6**e demonstrates that increment in the maximum separation distance would contribute to a first increase then decrease growth rate, which reveals that a reasonably higher maximum separation distance could promote the energy output performance significantly. **Figure 4.6**f illustrates a positive linearity between the $E_{em}$ and the contact surface area $S$. To sum up, thinner thickness, higher relative permittivity, longer maximum separation distance and larger contact surface area would contribute to an enhanced maximized effective energy output, based on simulation of equation (4-20).

### 4.3.4 Theoretical Analysis of Figure of Merits

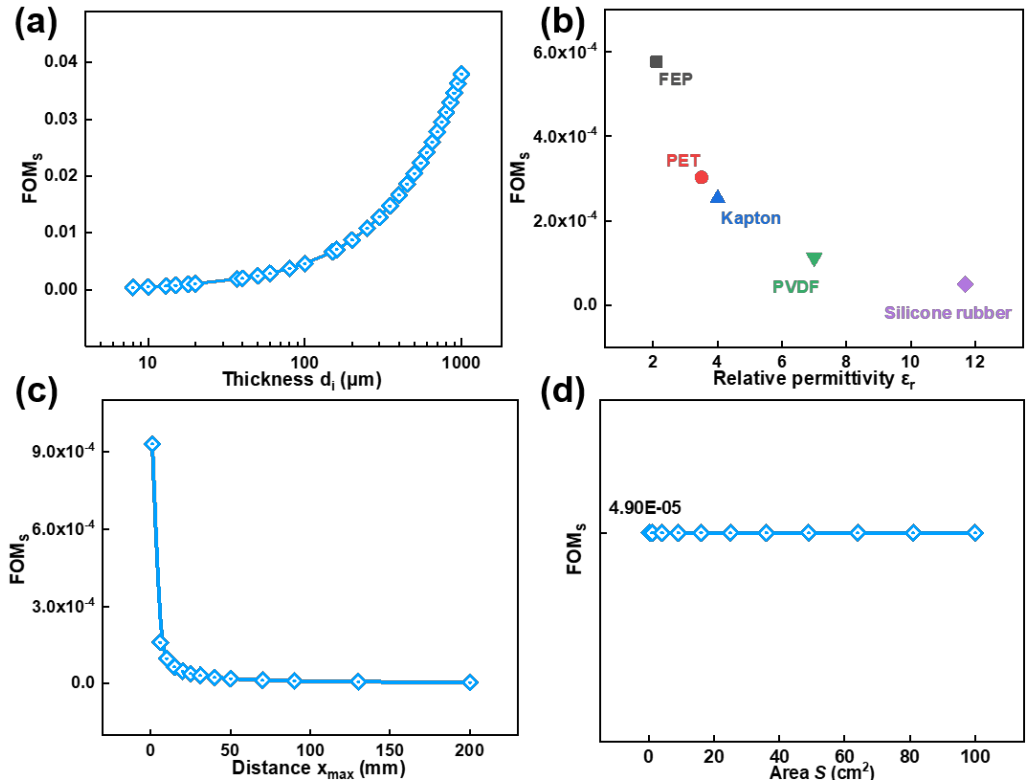


**Figure 4.8** Theoretical analysis of the structure figure of merit $FOM_S$. The structure figure of merit $FOM_S$ versus (a) thickness of dielectric layers, (b) relative permittivity

of dielectric layers, (c) maximized separation distance, and (d) area size of the dielectric layers.

Further investigation regarding the structure figure of merit $FOM_S$, which can be considered as the criteria of TENG's performance, was conducted, in which the $FOM_S$ can be expressed as:[49]

$$FOM_s = \frac{2\varepsilon_0}{\sigma^2}\frac{E_{em}}{Sx_{max}} \quad (4\text{-}21)$$

**Figure 4.8**a demonstrates a positive correlation between $FOM_S$ and the thickness of the dielectric layer, by varying the thickness $d_i$ from 8 to 1000 μm. Besides, **Figure 4.8**b and 5c both reveal that larger relative permittivity or maximized separation distance will contribute to a significant drop of $FOM_S$ at the beginning, then will not make an observable difference. The size of dielectric's contact area will have no effect on the $FOM_S$ based on the result in **Figure 4.8**d, which can also be observed from the expression of $FOM_S$ as the S in $E_{em}$ will be offset by the S in the denominator. Therefore, to enhance the performance of CS-TENG, a higher thickness of dielectric layers, lower maximized separation distance and relative permittivity of the dielectric layers may be reasonable, and the contact area size can be designed without limitation. Material FOM ($FOM_M$) is the evaluation standard of surface charge density, which depends on the triboelectrification of materials contact.[48] The theoretical definition is given by the following equation:[49]

$$FOM_M = \sigma^2 \quad (4\text{-}22)$$

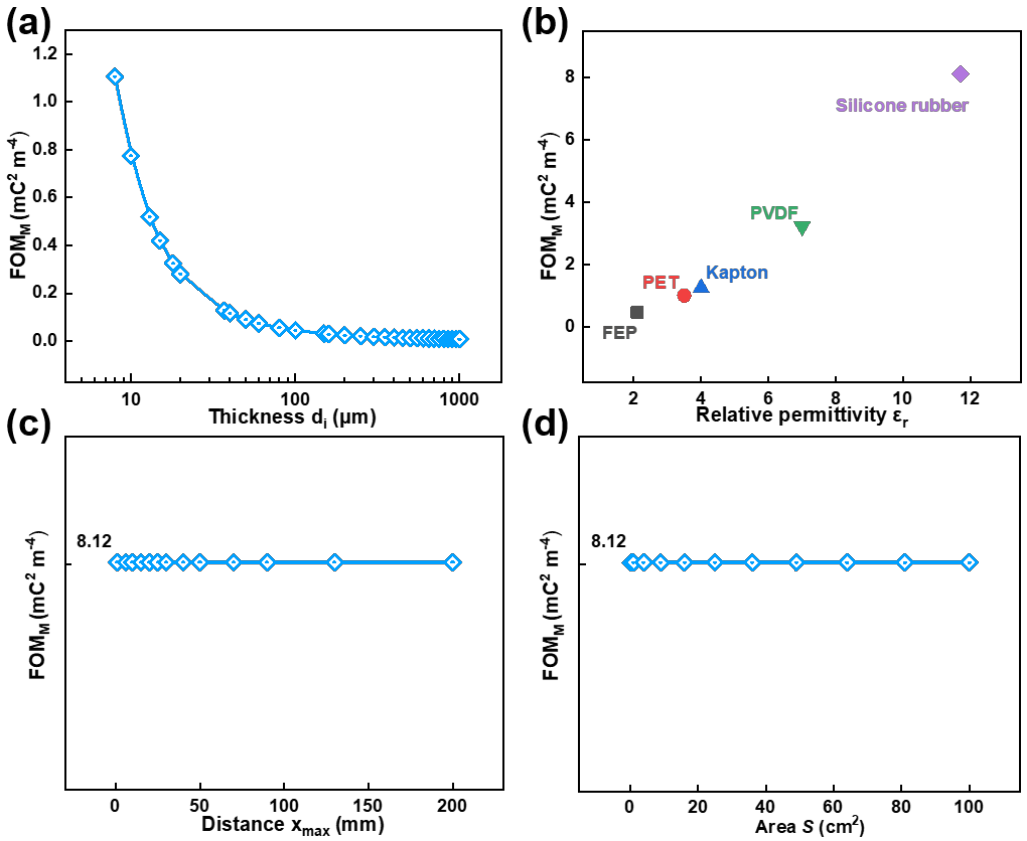


**Figure 4.9** Theoretical analysis of the material figure of merit $FOM_M$. The material figure of merit $FOM_M$ versus (a) thickness of dielectric layers, (b) relative permittivity of dielectric layers, (c) maximized separation distance, and (d) area size of the dielectric layers.

$FOM_M$ is proportional to the square of the surface charge density. Thus, the theoretical boundary of $FOM_M$ is determined by the $\sigma_m$ discussed above. From equation (4) and (5), the value of $\sigma_m$ is decided by the effective thickness constant $d_0$. Accordingly, the effects of thickness and relative permittivity on $FOM_M$ are consistent with $\sigma_m$ as illustrated in **Figure 4.9a** and b. Moreover, with the specific $d_0$, $FOM_M$ would not vary with the separation distance and size of devices, as presented in **Figure 4.9**c and d.

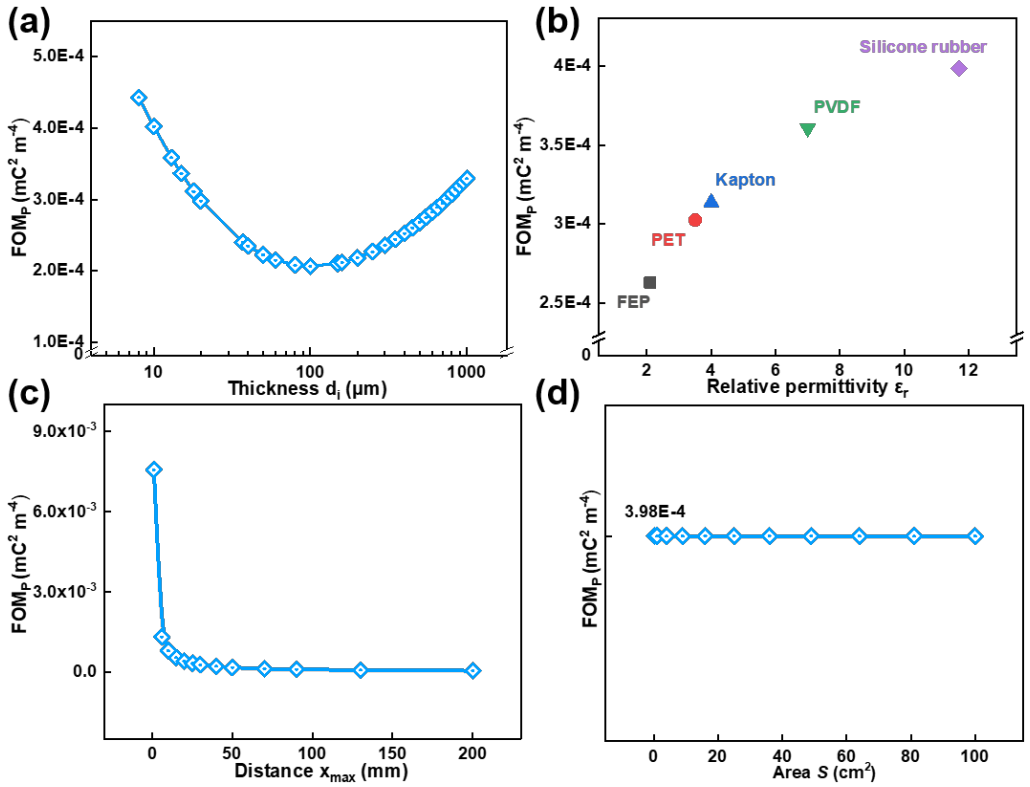


**Figure 4.10** Theoretical analysis of the performance figure of merit $FOM_P$. The performance figure of merit $FOM_P$ versus (a) thickness of dielectric layers, (b) relative permittivity of dielectric layers, (c) maximized separation distance, and (d) area size of the dielectric layers.

Based on the $FOM_S$ and $FOM_M$, the performance figure of merit $FOM_P$ is given as:[49]

$$FOM_P = FOM_S * FOM_M = 2\varepsilon_0 \frac{E_{em}}{Sx_{max}} \tag{4-23}$$

**Figure 4.10a** reveals the first decreasing and then increasing theoretical tendency of the performance figure of merit $FOM_P$ by varying the thickness $d_i$ from 8 to 1000 μm. This tendency remains the same as $E_{em} - d_i$'s as the $FOM_P$ is primarily dominated by the $E_{em}$. Still, **Figure 4.10**b demonstrates a positive correlation between $FOM_P$ and relative permittivity of dielectric layers, which is same as the tendency of $E_{em} - \varepsilon_i$ as the relative permittivity is only included inside the $E_{em}$. **Figure 4.10**c reveals that

larger maximized separation distance will contribute to a dramatical drop of $FOM_S$, and the size of dielectric's contact area still have no effect on the $FOM_P$ based on the result in **Figure 4.10**d. Therefore, to acquire a desirable highest achievable output performance, the relative permittivity of dielectric layers is supposed to be larger and maximized separation distance should be designed to be as small as possible.[48] Moreover, the thickness of dielectric layers can be fabricated lower for a more stable working system and the contact area size can be designed without limitation.

## 4.4 Conclusion

In summary, the limitation equations for the output performance of contact-separation TENGs were constructed under the restriction of air breakdown. Through the mathematical derivation and analysis of the limitation equations, evaluation approaches to the theoretical boundary of surface charge density and energy output were developed. From the deduced equation (4-10), the maximum surface charge density of TENGs drops with the increasing separation distance until reaching the critical point where air breakdown occurs. After air breakdown, the surface charge density would arrive at the saturated constant value regardless of the separation distance. The mathematical relationship between the maximum surface charge density $\sigma_m$ and the effective thickness constant $d_0$ reveals that thinner dielectric layers with higher relative permittivity could create the superior $\sigma_m$. Moreover, according to the redistricting of *V-Q* curves, a mathematical calculation method for maximized effective energy output $E_{em}$ was determined. Furthermore, structural parameters (separation distance, device

size) and material parameters (dielectric layer thickness, relative permittivity) were discussed about the impact of TENG's evaluation metrics including maximum surface charge density $\sigma_m$, maximized effective energy output $E_{em}$ and figure of merits. From these, optimization methodologies were proposed that in atmosphere, the effective strategies for achieving higher $\sigma_m$ are micro-nano separation distance and effective thickness constant reduction. For the former, the separation distance at micro-nano level could also decrease the external mechanical energy drives, improving the energy conversion efficiency. For the latter, thinner films with higher relative permittivity should be fabricated to reduce the effective thickness constant in further experiments. The simulation outcomes indicate $\sigma_m$ and $E_{em}$ of TENG provided with 10 μm silicone rubber as the dielectric layer could reach 2.85 mC/m$^2$ and 1.12 mJ, respectively. This work provides the calculation methods for theoretical boundary, which could predict the maximum values of surface charge density and energy output, displaying its potential in the design and optimization of TENG devices for ranking performance.

# CHAPTER 5 An Integrated Self-powered Real-time Pedometer System

## 5.1 Background

With the continuous improvement of people's living standards and economic income, self-care awareness has gradually been awakened.[113-114] The pedometer, a quantitative indicator, helps understand the number of exercised steps and consumed calories daily by obtaining steps, distance, time, speed, etc.[115] It is helpful and meaningful for people, especially athletes, to get knowledge of the amount of exercise and regulate their exercise plan.[116] The majority of merchandized products are mobile phone pedometer APP and pedometer bracelets, which are generally enabled by accelerometers/ gyroscopes[117] and battery-powered. However, these accelerometer/ gyroscope sensors suffer from some drawbacks. First of all, large movements of the human body will cause the accelerometer/ gyroscope to vibrate, resulting in data fluctuations and erroneous results.[118] Secondly, an external power supply is demanded to continuously power the accelerometer/ gyroscope sensor which brings energy loss. Additionally, even if the pedometer products contain built-in batteries as the power source, they may run out of electricity any time and would require regular charging. Consequently, developing novel technologies for step counting with accurate, energy-saving, self-sustained and self-powered characteristics becomes imperative.

As a portable step counting device, a pedometer has to satisfy the following criteria: (i) imperceptible to users; (ii) not load the user; (iii) long term lifetime; and (iv) cost-effective.[119] With the emerging development of TENG, it is feasible to harvest the

mechanical energy of human walking and analyze human walking gait.[7, 59, 120-121] Utilizing the characteristics of converting stepping mechanical energy into electrical signals, signals synchronized with users' footstep could be obtained.[122-124] It provides a new approach of sensors for the construction of a self-powered wearable pedometer system. There have been some researches in which TENGs were utilized as pressure sensors for gait monitoring, step counting and plantar pressure analysis.[66, 125-141] In most of the existing research outcomes, the signals generated by TENGs are directly used as sensing signals, which could bring about several problems. TENG-based sensors have a relatively low signal-to-noise ratio because they would be affected by the surroundings, which makes them unstable and uncertain for the back-end processing circuit. Secondly, the response time and recovery time could be further reduced to realize faster response.[142-143] Thirdly, more discussion within the walking weight range of the human body should be considered since they are applications concerning human movement.[128, 139] Apart from those, as a self-powered system, the power supply of the DAQP module and Bluetooth transmission needs to be considered.

In this chapter, a self-powered real-time pedometer with ultrafast response and high accuracy is put forward. The highly integrated system mainly consists of three parts: a TENG, a DAQP module and a mobile phone APP. Through human walking, the TENG converts the mechanical energy of human walking into electrical signals, which are acquired by the DAQP module. Therein, an analogue front-end (AFE) circuit was designed to regulate the TENG's signals for triggering step counting regardless of the

frequency and weight with an ultrafast response time of 8 ms. Then the step signals could be transmitted to the mobile phone APP in real-time. A press type EMG and a 5.5 V 5.0 F supercapacitor were integrated to provide electricity for the DAQP module to construct a sustainable self-powered system without an external power supply.

## 5.2 Experiments and Methods

### 5.2.1 Fabrication of the P-TENG

**Figure 5.1** shows a simple, scalable and low-cost engraving mold fabrication process of the porous silicone rubber layer. The liquid silicone rubber was pre-prepared by mixing two components (1:1 volume ratio) in a beaker. After being mixed uniformly, the mixture was poured into a pre-fabricated acrylic mold. Initially, the liquid silicone rubber mixture was poured into an acrylic mold which was cut by the laser cutter and assembled with Kapton tapes (step I). After solidifying for 4 h at room temperature, the silicone rubber formed a thin and uniform layer of substrate (step II). Continuing to pour the silicone rubber mixture on the substrate into the acrylic mold, a mixture of solid and liquid phases was formed after the silicone rubber spreading out evenly for few minutes (steps III and IV). Uniformly sized glass balls were arrayed evenly and neatly on the silicone rubber, and the glass balls sank into the silicone rubber owing to gravity until touched the solid-liquid interface (step V). Finally, the solidified silicone rubber was peeled off from the acrylic mold and the glass balls after naturally curing for another 4 h (step VI). Two copper lead wires were attached to each copper foil by silver glue respectively.

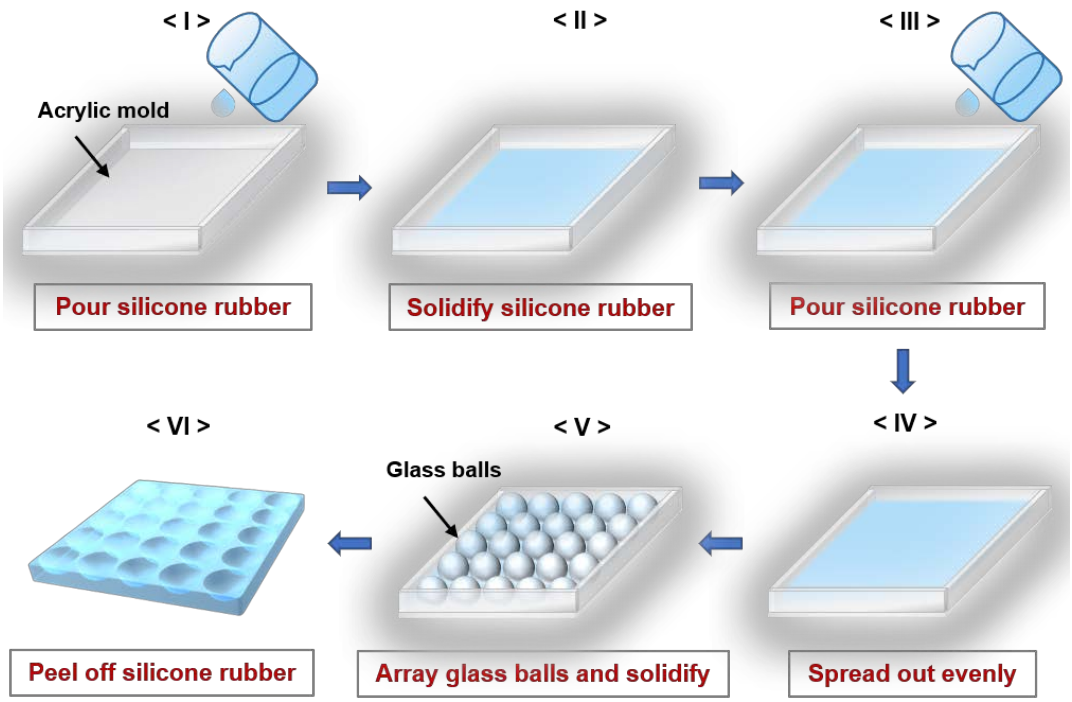


**Figure 5.1** Schematic illustration of the porous silicone rubber layer fabrication process.

### 5.2.2 Fabrication of the AFE and DAQP

The schematic of the AFE was designed and simulated for functionality using PSPICE. Multiple sets of values of the current limiting resistors ($R_1$, $R_2$ and $R_3$) were applied in PSPICE with a 1 kΩ step to find a combination with relatively higher gain (step I). After settling the circuit parameters, the schematic of the AFE was drawn along with the DAQP using the PADS 9.5 software. The Bluetooth device design took reference from the reference design manual provided by manufacturer. With schematics verified, PCB layouts and routings were finished in PADS (step II). Then a third-party factory manufactured the designed PCBs (step III). All the components used in the design were manually soldered to the final PCBs (step IV).

### 5.2.3 Electrical Measurement

A linear motor (Winnemotor, WMUC512075-06-X) was used to provide the contact

and separation process with variable frequencies. A vertical single-axis motor (HC14-10) was used to apply variable vertical force, which was measured by a pressure sensor (DS2-2000N-XD). A programmable electrometer (Keithley 6514) was adopted to test the output performance, including $V_{oc}$, $I_{sc}$ and $Q_{sc}$. The software platform constructed by LabVIEW is utilized to obtain real-time data.

## 5.3 Results and Discussion

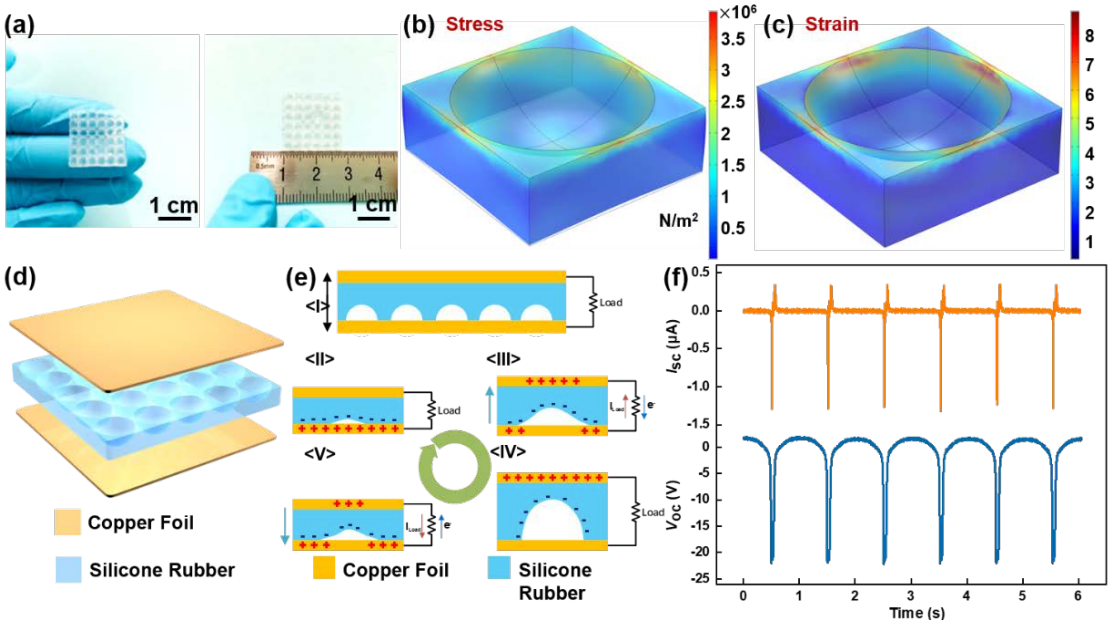


**Figure 5.2** General characterization of porous triboelectric nanogenerator (P-TENG). (a) Photograph of the porous silicone rubber layer (scale bar, 1 cm). COMSOL Multiphysics simulation results of (b) stress distribution diagram and (c) strain distribution diagram. (d) Schematic illustration of P-TENG. (e) Schematic illustration of the electricity generating mechanism. (f) The raw electrical output of P-TENG, including open-circuit voltage ($V_{oc}$) and short-circuit current ($I_{sc}$).

The general characterization of the P-TENG components is depicted in **Figure 5.2**. To achieve the contact-separation mode while walking, a porous structure was designed. Silicone rubber, a material with good biocompatibility, stretchability, moldability and

superhydrophobicity with a contact angle of 116.5° (**Figure 5.3**a), was employed as the elastic support.[60, 144] The as-obtained silicone rubber layer exhibits a good porous structure and flexible property as the photograph shown in **Figure 5.3**b and c.

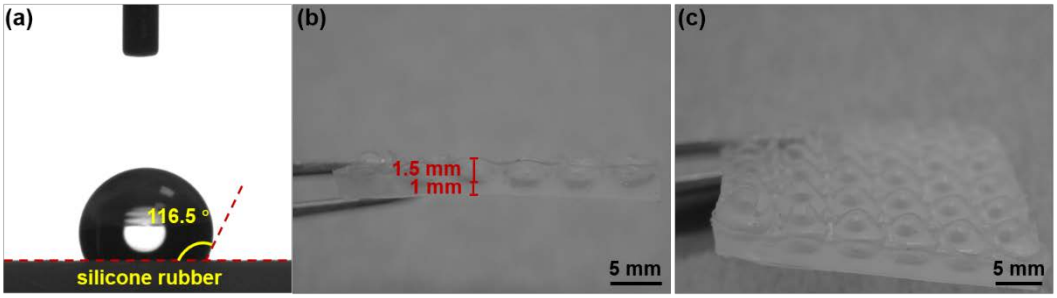


**Figure 5.3** (a) Contact angle of a water droplet on the silicone rubber surface, (b) Cross-sectional photograph of the porous silicone rubber layer, (c) Surface photograph of the porous silicone rubber layer.

**Figure 5.2**b and c demonstrate the stress and strain distribution diagram by COMSOL Multiphysics simulation, respectively. In this COMSOL Multiphysics simulation, the bottom surface was set as a fixed constraint according to the practical situation. To imitate the human body to press down, the upper surface was given a boundary load. **Figure 5.2**b illustrates the stress distribution of one unit with a pressure range from 0 to $4*10^6$ N/m$^2$. The strain distribution of the unit was displayed in **Figure 5.2**c. It can be seen that the center of the upper surface shows a certain degree of strain, while the periphery of the bottom presents a greater strain. Two pieces of copper foil with a conducting copper lead wire were attached on both sides of the porous silicone rubber layer to form the P-TENG as **Figure 5.2**d, which was encapsulated by Kapton tapes. As the application and withdrawal of external force, the porous structure could collapse and recover, which constitutes the contact and separation states between the silicone

rubber and copper foil. Based on the coupling effect of contact triboelectrification and electrostatic induction, the P-TENG could convert mechanical energy into electrical energy.[69] **Figure 5.2**e explains the working mechanism of the P-TENG. As the initial state, the porous structure is complete and the interstitial gap parts of silicone rubber touch the copper foil (state I). When the user walks and steps on the ground, an external force is applied to the P-TENG and makes the porous structure sink. The negative charges would remain on the surface of the silicone rubber and the positive charges form on the copper foil because of the difference in electronegativity (state II). As one's feet leave off the ground, the porous structure would gradually recover and a certain potential difference between the two copper foils is produced. The positive charges would be induced on the upper copper foil which drives the free electrons to flow from the upper to the lower copper foil to form an electrical signal (state III). When the porous structure recovers to the original state, the negative charges on the surface of silicone rubber would be equal to the induced positive charges on the copper foil to make up an equilibrium, where no electrical signal is observed (state IV). When one's feet return to the ground, the potential difference induces the free electrons to flow from the lower to the upper copper foil, causing a reverse electrical signal (state V). With the trampling and leaving cycles of one's feet, an alternating current is generated.

To evaluate the output performance of the P-TENG, a linear motor was employed to simulate the cyclic motion of human walking. The short-circuit current ($I_{sc}$) of a P-TENG (1.8×1.8 $cm^2$) reaches 1.3 μA and the open-circuit voltage ($V_{oc}$) reaches 25 V at

a certain frequency of 1 Hz, which revealed in **Figure 5.2**f. Considering $I_{sc}$ and $V_{oc}$ are in line with human motion indeed, the electrical signals of P-TENG could work as the sensing parameters to present people's pace situation. Besides, a DAQP will be utilized to identify, acquire and count the electrical signals. However, the current $I_{sc}$ provided by TENG is below sufficient level to be detected by back-end circuits. In addition, the voltage $V_{oc}$ provided is always higher than the breakdown voltage of back-end electronic components. Both of the consequences damage the system. As a result, the raw electrical signal of P-TENG is not suitable to be directly regarded as the sensing parameter, signal level clamping and signal buffering circuits are added.

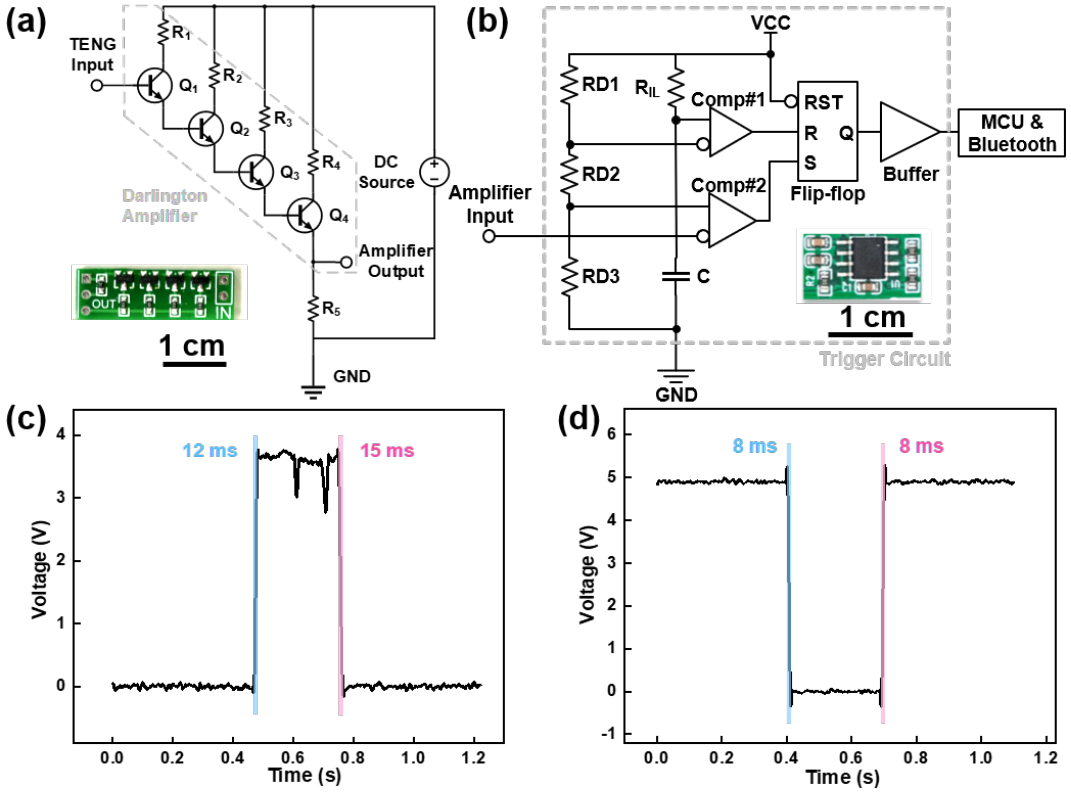


**Figure 5.4** Analogue front-end (AFE) circuit design and characterization for processing the signals generated by the P-TENG. (a) Circuit diagram of the amplifier circuit (inserted: photograph of the amplifier PCB), (b) trigger circuit (inserted: photograph of

the trigger PCB). Response-recovery curve and edge width of (c) the amplifier circuit, (d) trigger circuit outputs.

A complete AFE (analogue front-end) circuit was designed as shown in **Figure 5.4**. An amplifier circuit was utilized to boost the stepping signal to a mA level and clamp the signal voltage level to be sufficient for signal detection by the trigger circuit. The bipolar junction transistors (BJTs), $Q_1$, $Q_2$, $Q_3$ and $Q_4$, consist of two PN junctions and are in Darlington connection, which cascades a few simple common-emitter amplifiers in a manner that connects the base of the next stage to the emitter of the previous stage, as shown in **Figure 5.4**a. The four stages are all biased at stabilized DC power source via current limiting resistors $R_1$, $R_2$, $R_3$ and $R_4$. $R_4$ and $R_5$ are used as voltage divider resistors to ensure a high electric level at the output terminal when the BJTs are conductive. One terminal of the TENG is connected to the base of $Q_1$. Electrons from excited TENG forms base-emitter current $I_{be}$ from base to emitter, which pushes carriers in the PN junction of $Q_1$ to improve its conductivity and thus control the collector-emitter current $I_{ce}$.

With the amplifier circuit, the current gain and voltage limit are achieved. The gain of a basic amplifier with one BJT is given by:

$$\beta = \frac{I_e}{I_b}, \tag{5-1}$$

where $I_e$ is emitter current and $I_b$ is base current. In the Darlington connection, the output of $Q_1$ is the input of $Q_2$, the output of $Q_2$ is the input of $Q_3$ and the output of $Q_3$ is the input of $Q_4$. If the gains of $Q_1$, $Q_2$, $Q_3$ and $Q_4$ are assumed as $\beta_1$, $\beta_2$, $\beta_3$ and $\beta_4$, then

ideally the total gain will be each stage's gains of the amplifier:[145]

$$\beta_{total} = \beta_1 \cdot \beta_2 \cdot \beta_3 \cdot \beta_4. \quad (5\text{-}2)$$

Open circuit and short circuit tests of the Darlington amplifier could provide current amplitude up to 24 mA. This yields a gain of 2400, while the high electric level stays stable at around 3.98 V (**Figure 5.4**c).

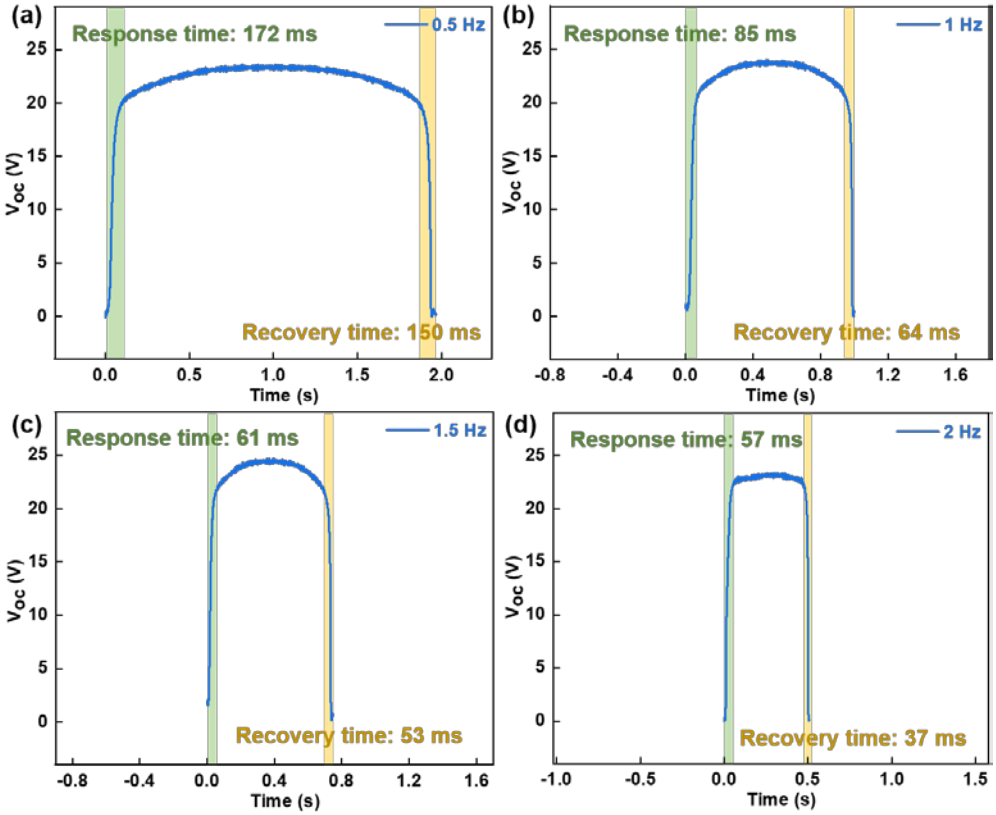


**Figure 5.5** Voltage response-recovery curve of the P-TENG raw data at (a) 0.5 Hz, (b) 1 Hz, (c) 1.5 Hz, (d) 2 Hz.

In addition to this, the response and recovery time are significantly reduced with the utilization of the amplifier circuit. $Q_1$-$Q_4$ are characterized with delay time 35 ns, rise time 35 ns and fall time 50 ns. As long as TENG current reaches the level where $Q_1$ is on, the emitter of $Q_1$ could be at a high electric level at the fastest speed as 70 ns. The circuit connection decides that $Q_1$, $Q_2$, $Q_3$ and $Q_4$ are turned on sequentially, hence the

shortest time taken to set the whole amplifier from high to low is theoretically 340 ns. Practically tested in **Figure 5.4**c, the amplifier yielded 12 ms response time and 15 ms recovery time, which is respectively 14.33 times and 15 times faster than the intrinsic signals of TENG at 0.5 Hz (**Figure 5.5**a).

After being clamped by the amplifier circuit, there still exist some ripples in the high state of amplifier output. A trigger and buffer circuit as shown in **Figure 5.4**b was added to stabilize the voltage level of the signal fed to the Bluetooth device. The output voltage level Q of Flip-flop is reversed when either input R or S is set high. Since the reset port RST is reversed and connected to $V_{CC}$, Q is automatically set low at power-up. Buffer is a non-inverting buffer whose input and output are in phase. Both of the comparators Comp#1 and Comp#2 have positive and negative inputs, with their voltage levels $V^+$'s and $V^-$'s, respectively. The positive inputs are connected to middle points of a 3-in-series chain of resistors with the same resistance, and negative inputs are marked with a small circle. Hence the voltage levels on $V^+_1$ and $V^+_2$ are:

$$V^+_1 = V_{CC} \cdot \frac{R_{12}+R_{13}}{R_{11}+R_{12}+R_{13}} = \frac{2}{3}V_{CC} \tag{5-3}$$

$$V^+_2 = V_{CC} \cdot \frac{R_{11}}{R_{11}+R_{12}+R_{13}} = \frac{1}{3}V_{CC}. \tag{5-4}$$

The output $V_{out}$ of a comparator is high when $V^+ > V^-$, and reversed, otherwise.[146] As in **Figure 5.4**b, Port $V^+$ of Comp#1 is pulled up via a 1 MΩ resistor $R_{14}$ and then $V_{out1}$ is set high after power-up. Consequently, the output Q of Flip-flop is set to be high, which results in the output $V_{trig}$ of trigger circuit being set high most of the time after power-up. When the amplifier feeds a high voltage level to a negative input of Comp#2, $V^-_2$ is

set high. The high level appears at input S of Flip-flop, which flips the output Q to be low. Therefore, the input and output of the trigger circuit are inverted, as proved by test results in **Figure 5.4**c and d. In monostable operation, the time of level alteration in the trigger circuit signals are determined by values of $R_{14}$ and $C_1$:

$$t_a = 1.1 \cdot R_{14} \cdot C_1, \tag{5-5}$$

where $R_{14}$=1 MΩ, $C_1$=10 nF. So by calculations, the minimal $t_a$ is 11 ms.

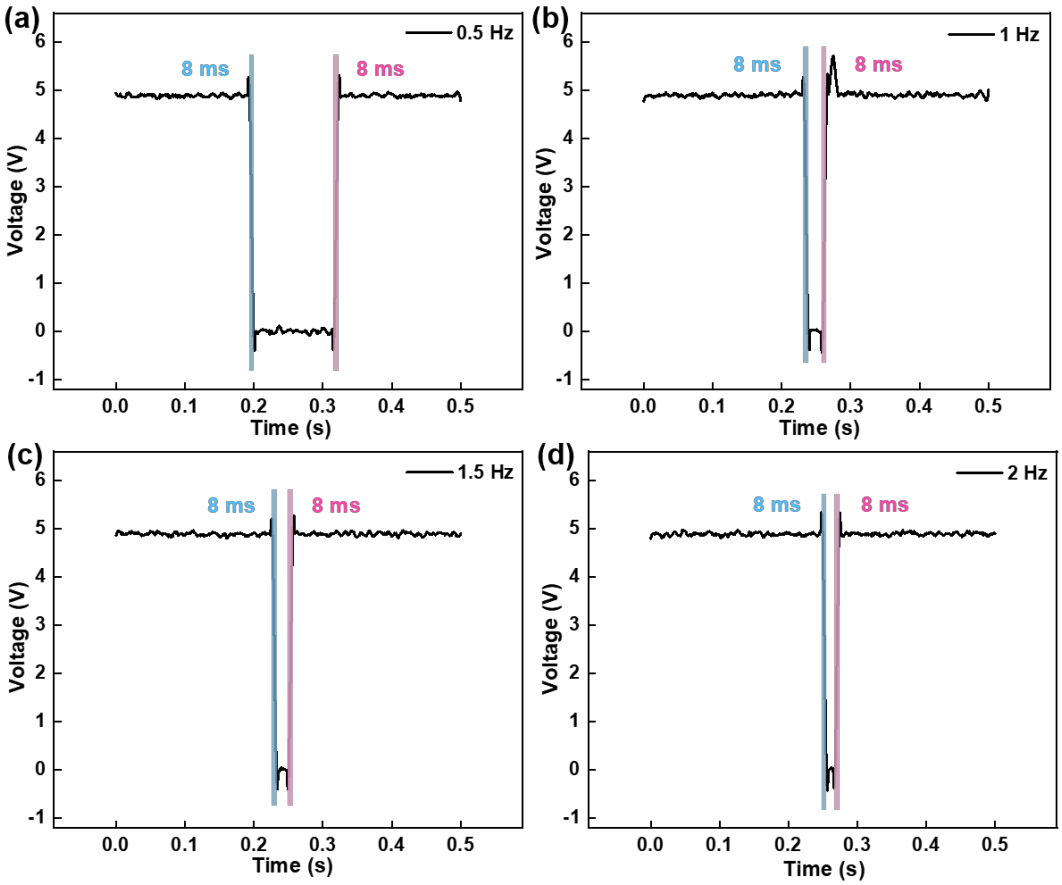


**Figure 5.6** Voltage response-recovery curve of the analogue front-end (AFE) circuit at (a) 0.5 Hz, (b) 1 Hz, (c) 1.5 Hz, (d) 2 Hz.

In theory, the P-TENG acts as a charge source that provides charges to form current so as to drive the amplifier and triggering the BJTs to turn on. Due to the existence of depletion area in a PN junction, there exists intrinsic input and output capacitances in

BJTs. Compared to the capacitance of the P-TENG (hundreds of pF),[147] the typical input capacitance of the transistors used is 8 pF, which is decades smaller. Hence, the voltage level on the input terminal of the BJT amplifier needs a much smaller amount of charge to alter, compared to the P-TENG. Due to the manufacturing tolerance in resistors, capacitors and the trigger circuit, however, the actual value of $t_a$ is 8 ms, as in **Figure 5.4**d and **Figure 5.6**, which is 21.5 times and 28.13 times faster than the intrinsic response time of the P-TENG (**Figure 5.5**). The response time of 8 ms regardless of the external frequency is superior to most previous human-machine interface work by virtue of the ultrafast response.

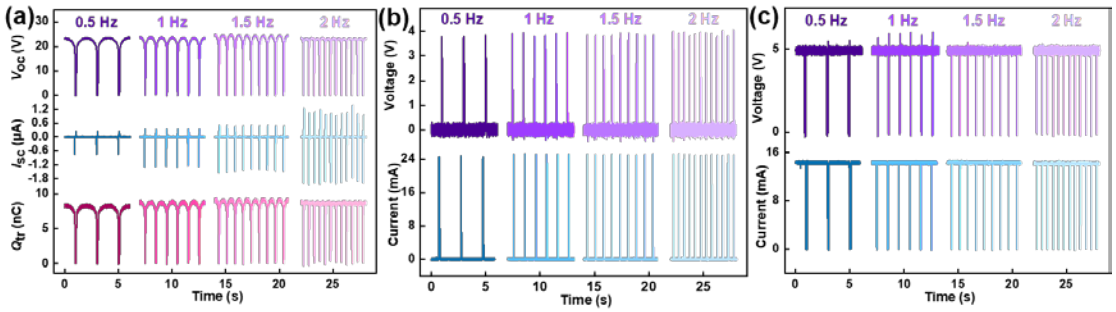


**Figure 5.7** Working conditions at different frequencies. (a) Electrical output under various motion frequencies ranging from 0.5 to 2 Hz, including open-circuit voltage ($V_{oc}$), short-circuit current ($I_{sc}$), and transferred charge ($Q_{tr}$). (b) Electrical output after the amplifier circuit. (c) Electrical output after the trigger circuit.

As people walk or run, the paces are different, such as slow walking, jogging and running. To ensure the stability of the step counting system under all situations, it is necessary to consider the walking frequency, as presented in Figure 5.7. Figure 5.7a displays the electrical output of P-TENG under various human motion frequencies ranging from 0.5 to 2 Hz. The $V_{oc}$ and $Q_{tr}$ remain almost 25 V and 9 nC, respectively.

Meanwhile, the $I_{sc}$ increases from 0.76 to 2.01 μA with the addition of the motion frequency, which indicates $I_{sc}$ is positively related to the frequency.

**Figure 5.7**b and c show the measured current and voltage at output terminals of the amplifier circuit and the trigger circuit under different motion frequencies. For the amplifier, the voltage is clamped at 3.98 V while the current maintains at approximately 24 mA instead of changing with the motion frequency. For the trigger circuit, since the comparators and the flip-flop are all internally biased to 5 V, their output voltage level count not exceed 5 V.

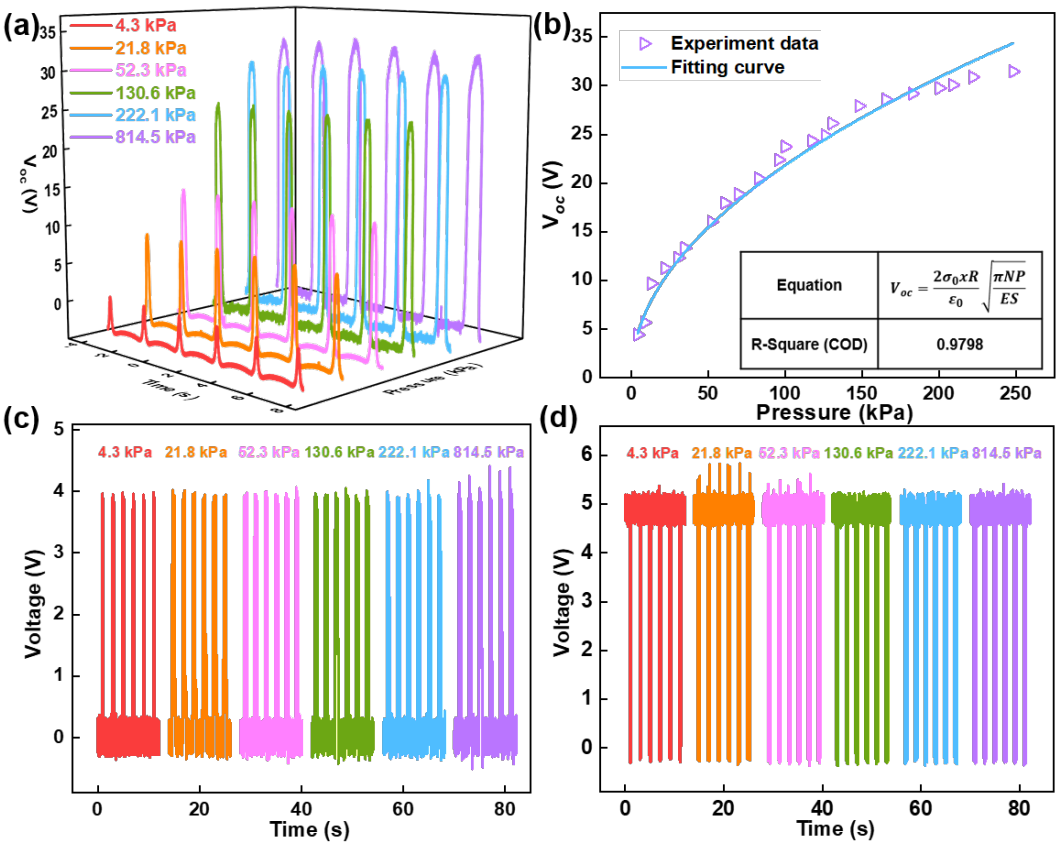


**Figure 5.8** Working conditions under different pressure. (a) Open-circuit voltage output under various applied pressure ranging from 4.3 to 814.5 kPa. (b) The summarized relationship and theoretical fitting between the relative variations ($V_{oc}$) and the pressure applied on P-TENG. (c) Electrical output after the amplifier circuit. (d) Electrical output

after the trigger circuit.

In addition to the effect of the motion frequency, the body weight of user is the other factor that is worth discussion. The raw $V_{oc}$ of the P-TENG and voltage output from the amplifier/ trigger circuit is demonstrated in **Figure 5.8**. **Figure 5.8**a indicates that the $V_{oc}$ increases from 4.6 to 33.8 V as the applied weight rising from 4.3 to 814.5 kPa. As deformable nano/microstructure, the effective contact area would change under different deformation conditions with increasing applied pressure. A theoretical model was built to explain why the $V_{oc}$ gradually improves with the increasing pressure. To simplify the model, it is assumed that all the porous structures are hemispheres and each arch is regarded as a unit block, with a total of $N$. Another assumption is only the porous structure is deformed from the periphery while the upper and gap blocks keep initial when applying an external force (**Figure 5.2**d). The silicone rubber porous structure, as a high elastomer, would generate an inherent elastic force which causes the deformation to counter the applied force. Until the elastic force and applied force are equal ($F_{elastic}$=$F_{applied}$), the porous structure reaches equilibrium and no longer deforms.[148]

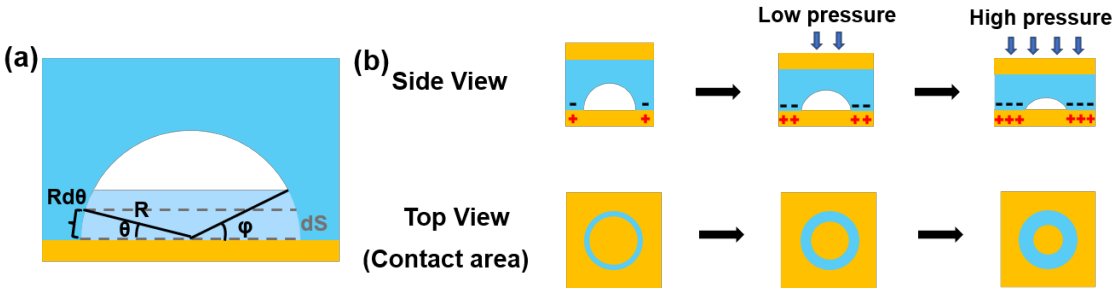


**Figure 5.9** (a) A schematic cross-sectional view of one arch. (b) Deformation process of one arch with increasing applied pressure.

The deformation process is theoretically simulated in **Figure 5.9** to analyze the effect

of applied pressure on the $V_{oc}$ of P-TENG. **Figure 5.9**a demonstrates the cross-sectional schematic diagram of one unit, in which R represents the radius of the arch. φ is the deformation angle when reaching the equilibrium, and is from 0 to $\frac{\pi}{2}$. $\theta$ represents an integral angle with a range from 0 to φ. In the first case, with the applied pressure increasing gradually, the deformation area would become larger as illustrated in **Figure 5.9**b. The contact area could be regarded as the deformation strip and the deformation angle φ is less than $\frac{\pi}{2}$. Herein, the length of the arc corresponding to angle $\theta$ could be denoted as $R\,d\theta$, and the deformation area could be expressed as:

$$dS = 2\pi R\cos\theta \cdot R\,\mathrm{d}\theta \tag{5-6}$$

Then, the total deformation area could be deduced as

$$A_{total} = N\int_0^{\varphi} 2\pi R\cos\theta \cdot R\,\mathrm{d}\theta = N2\pi R^2\sin\varphi \tag{5-7}$$

Based on Young's modulus, the differential elastic force could be inferred as

$$\mathrm{d}f_{elastic} = E2\pi R^2\cos\theta\,\mathrm{d}\theta\cdot(\sin\varphi - \sin\theta), \tag{5-8}$$

where $E$ is effective Young's modulus of the porous structure silicone rubber.

Thus the elastic force formed on the deformation strip is

$$f_{elastic} = \int_0^{\varphi} E2\pi R^2\cos\theta(\sin\varphi - \sin\theta)\,\mathrm{d}\theta = E\pi R^2\sin^2\varphi. \tag{5-9}$$

The total elastic force of the P-TENG is obtained as

$$F_{elastic} = N\cdot f_{elastic} = NE\pi R^2\sin^2\varphi. \tag{5-10}$$

According to Equations (5-7) and (5-10), the relation could be obtained as

$$A_{total} = 2R\sqrt{\frac{\pi NF_{elastic}}{E}} \tag{5-11}$$

From Equation (5-10), with larger applied pressure, more area of the porous structure

is deformed to generate larger elastic force to balance the applied force, which results in more triboelectric surface charges on the triboelectric layer. $Q$ is used to represent the total amount of the transferred charges, expressed as

$$Q = \sigma_0 \cdot A_{total} = 2\sigma_0 R\sqrt{\frac{\pi N F_{elastic}}{E}}, \quad (5\text{-}12)$$

where $\sigma_0$ means the surface charge density.

According to the contact-separation mode, the $V_{oc}$ could be deduced as

$$V_{oc} = \frac{Qx}{\varepsilon_0 S}, \quad (13)$$

in which $\varepsilon_0$ is the permittivity of vacuum, $x$ is the separation distance between two triboelectric layers and $S$ is the device area.[24]

At the equilibrium state, the elastic force and applied force are equal. Therefore, the relation between the applied pressure and $V_{oc}$ could be obtained as

$$V_{oc} = \frac{Qx}{\varepsilon_0 S} = \frac{2\sigma_0 xR}{\varepsilon_0 S}\sqrt{\frac{\pi N F_{elastic}}{E}} = \frac{2\sigma_0 xR}{\varepsilon_0}\sqrt{\frac{\pi NP}{ES}} \quad (5\text{-}14)$$

This equation indicates the direct relationship between the external pressure and the $V_{oc}$ of P-TENGs at the low pressure range. However, if the applied pressure is high enough, the deformation area is the total surface area of the hemisphere. In this case, φ equals to $\frac{\pi}{2}$. Herein, the total deformation area could be deduced as:

$$A_{total} = N2\pi R^2 \quad (5\text{-}15)$$

Then the total amount of the transferred charges is:

$$Q = \sigma_0 \cdot A_{total} = 2\pi N\sigma_0 R^2 \quad (5\text{-}16)$$

Thus the $V_{oc}$ of P-TENGs is regarded as a constant value as:

$$V_{oc} = \frac{Qx}{\varepsilon_0 S} = \frac{2\pi N\sigma_0 R^2 x}{\varepsilon_0 S} \quad (5\text{-}17)$$

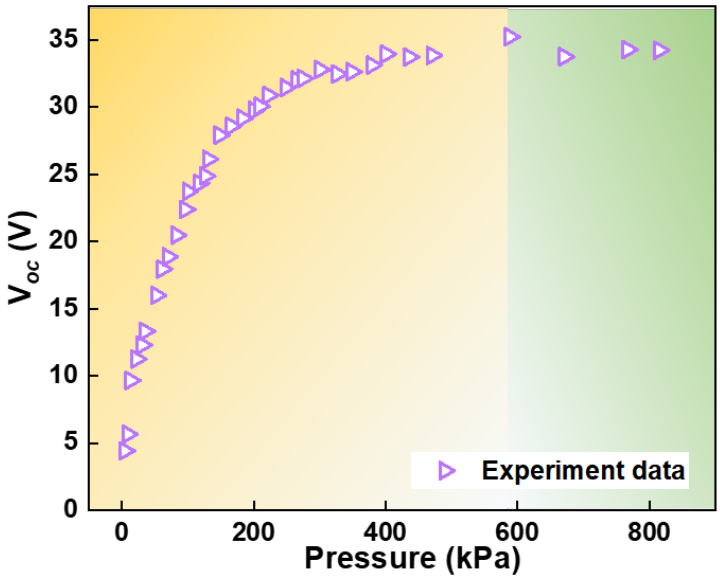


**Figure 5.10** The summarized relationship between the relative variations ($V_{oc}$) and the pressure applied on P-TENG ranging from 4.3 to 814.5 kPa.

**Figure 5.10** summarizes experimental data in the pressure range from 0.1 to 18.7 kg on a 1.5*1.5 $cm^2$ P-TENG, presenting rising and saturated regions, as deduced in equations (5-14) and (5-17). The fitting line shows great consistency with the experiment data with fitting linearity of 97.98%. From both theoretical and experimental results, it reveals that the $V_{oc}$ of P-TENG would improve with the increasing external pressure and reach a constant value, which is unfavourable to gain a stable voltage for the identification and capture of the back-end circuit.

With the as-obtained amplifier circuit, all the voltages are controlled to maintain 3.98 V under the variable pressure, as shown in **Figure 5.8**c. It helps exclude the influence of users' weights and keep the counting system stable. Compared with the 100 MΩ impedance of P-TENG, the input impedance between base and emitter of $Q_1$ is relatively small (~10 kΩ). The P-TENG could be seen as short-circuited by $Q_1$ and

voltage between the P-TENG terminals is nearly 0 V. Because the relatively low voltage and current level fed to the amplifier are insufficient to cause voltage disturbance in bias voltage, electrons could only flow single direction from base to emitter. The P-TENG output does not affect the output of $Q_1$, therefore the output of the Darlington amplifier is irrelevant to the input voltage generated by the P-TENG.

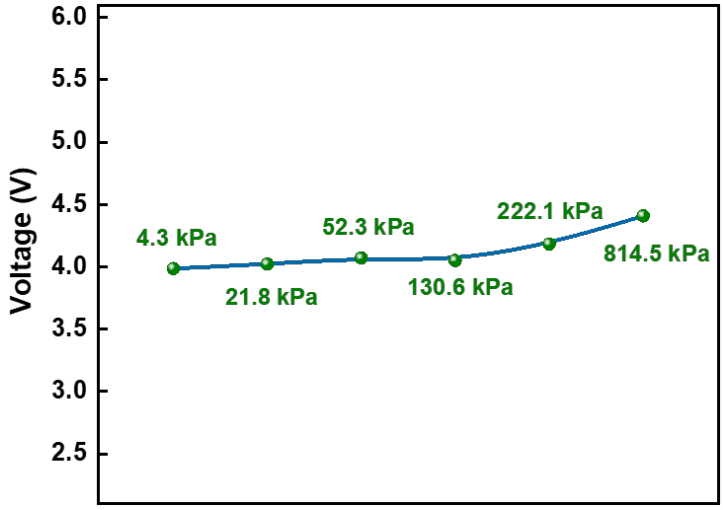


**Figure 5.11** Peak voltage output of the amplifier circuit with increasing $V_{oc}$ input owing to the enlarged applied force.

In addition, the variance of around 810 kPa of weight during the pressure test only causes less than 0.5 V of voltage deviance in amplifier output, as shown in **Figure 5.11**. This proves our amplifier could neglect the effects of P-TENG voltage and current whilst providing stable outputs. Then, the output voltage of the trigger circuit is controlled to stabilize at 5 V or 0 V (**Figure 5.8**d), but not affected by the applied pressure.

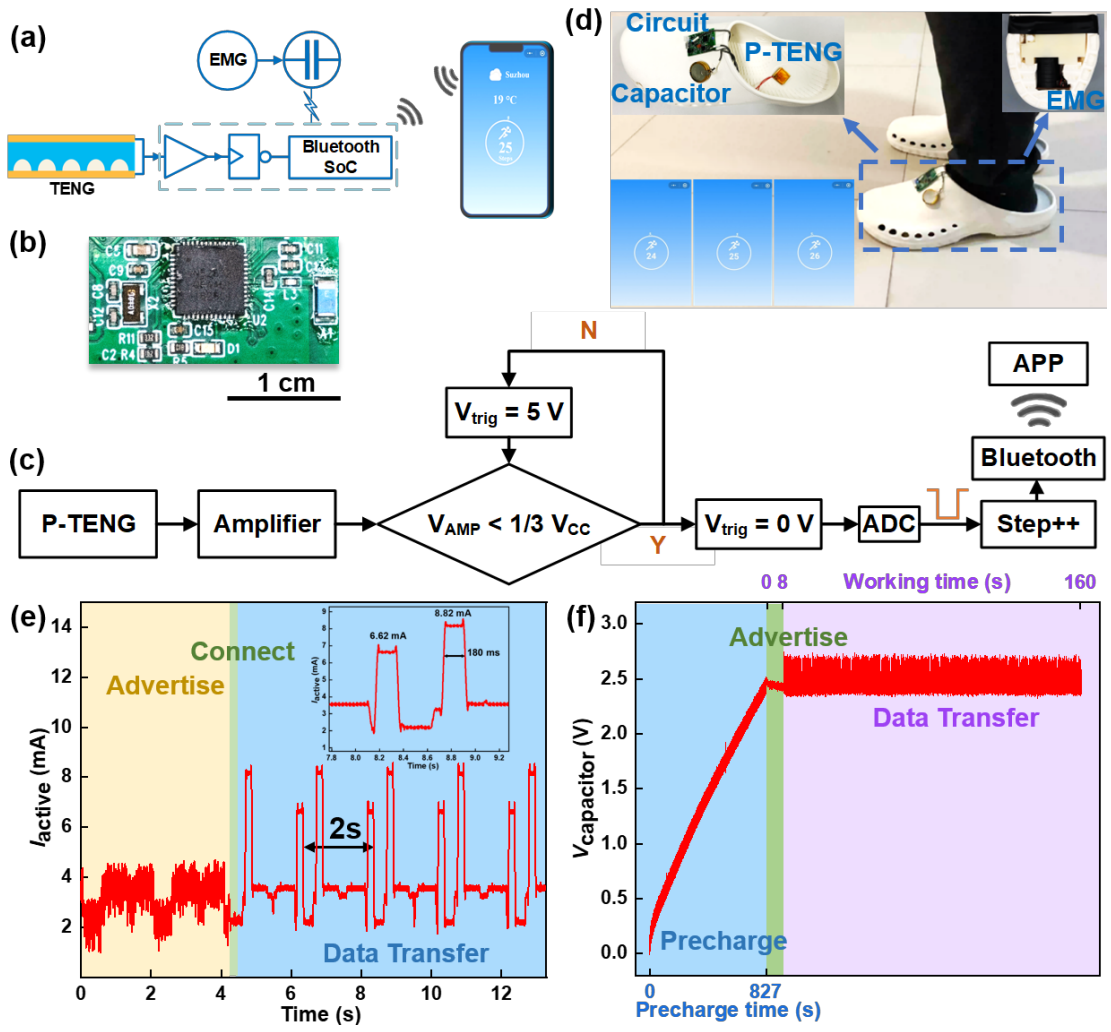


**Figure 5.12** Demonstration of the self-powered step counting system. (a) System overview of the pedometer. (b) The PCB assembly of the Bluetooth SoC modules. (c) System-level block diagram of the complete pedometer showing the signal generation, transduction, processing, wireless transmission. (d) Photograph of the pedometer stuck to the experimental shoes (inset up shows the step counting interface on mobile APP by three consecutive steps). (e) Working current changes with the timing sequence of data acquisition, including advertising, connecting, and data transferring period, which are highlighted by yellow, green, and blue, respectively. The inset demonstrates the peak current during the data transferring period. (f) The self-powered real-time step counting of the integrated pedometer system.

**Figure 5.12** demonstrates the pedometer system mounted on shoes for practical step

counting and power consumption evaluation. The integrated pedometer system consists of six components schematically shown in **Figure 5.12**a, including a P-TENG, an amplifier, a trigger unit, a Bluetooth SoC (System on Chip) with a microprocessor core and a Bluetooth device (photographed in **Figure 5.12**b), an EMG and a supercapacitor. **Figure 5.12**c gives a hint of the systematic logic flow of the complete pedometer containing processes of signal generation, transduction, processing and wireless transmission. Synced with user's walking pace, the P-TENG generates electrical signals which will be regulated by the AFE circuit to alter the changeable and mismatched nature of the P-TENG signals. The stabilized signal from the AFE circuit is then fed to the input terminal of the analogue to digital converter (ADC) of the Bluetooth SoC and be digitalized. Inside the Bluetooth SoC, the digitalized signal looks like a square wave. Each positive and negative edge correspond to contact and separation process respectively. In order to count the steps walked by two feet with one P-TENG, the Bluetooth SoC was programmed to add 1 to a step counter at every positive and negative edge detected in the digitalized signal. Detailed logic is shown in **Figure 5.13**.

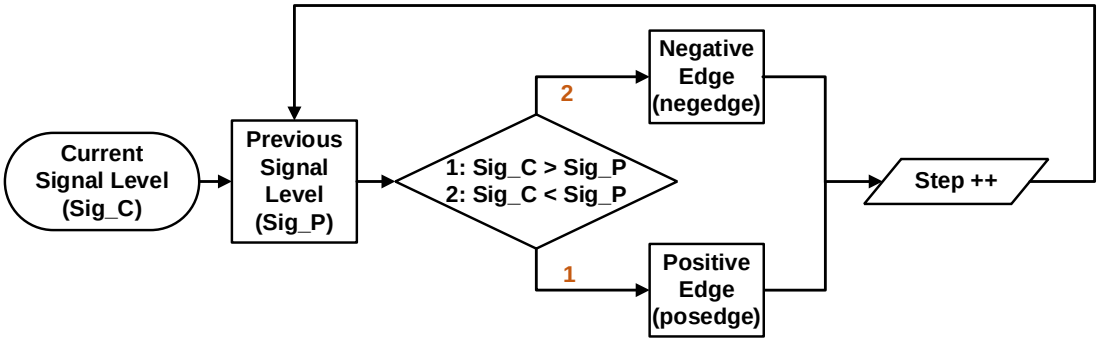


**Figure 5.13** Step counting logic programmed in the Bluetooth SoC enabling the feature of counting two steps with one cycle of P-TENG signal.

This contributes to the phenomenon that step count increases by every walking cycle. The value of the counter will be transmitted to a smartphone paired with the Bluetooth device once it is altered. In the smartphone, this counter value is displayed as a step number. To verify the potential in step counting applications on the human body, the pedometer is made wearable and attached to people's shoes. As illustrated in **Figure 5.12**d, the P-TENG is placed on the heel of the shoe while the DAQP module and supercapacitor are attached to the surface of the shoe, the EMG used to support self-power operation is mounted inside the heel and could be seen from the bottom of the shoe. Inset shows three screenshots of continuous step counting from 24 to 26 steps. As people walking, the pedometer could realize real-time continuous counting along with the user's pace.

Since this pedometer system is based on P-TENG, continuous usage strikes challenges to durability of both the P-TENG and the integrated system. To assess reliability systematically, a testing system was set up with the P-TENG wired to the DAQP module and connected to a smartphone via Bluetooth, where the P-TENG was driven by a linear motor at a frequency of 2 Hz under 300 kPa (higher than the plantar pressure of a normal man). It can be seen in **Figure 5.14** that $V_{trig}$ stably keep jumping between 0 and 5 V. The first few peaks and around 100,000$^{th}$ few peaks were magnified respectively in **Figure 5.14**a-b, which shows high consistency from beginning to end of the stability test. The physical morphology of the P-TENG was recorded as the optical images at the beginning and 100,000$^{th}$ of the testing cycles, as shown in **Figure 5.14**c-d. Over

100,000 continuous strikes did not introduce obvious mechanical deformations and structural deteriorations to the porous dielectric layer in the P-TENG. 100,000 continuous strikes, namely, 200,000 counts prove the integrated pedometer system including the P-TENG, DAQP module and corresponding smartphone APP provides nobly high reliability and satisfying robustness.

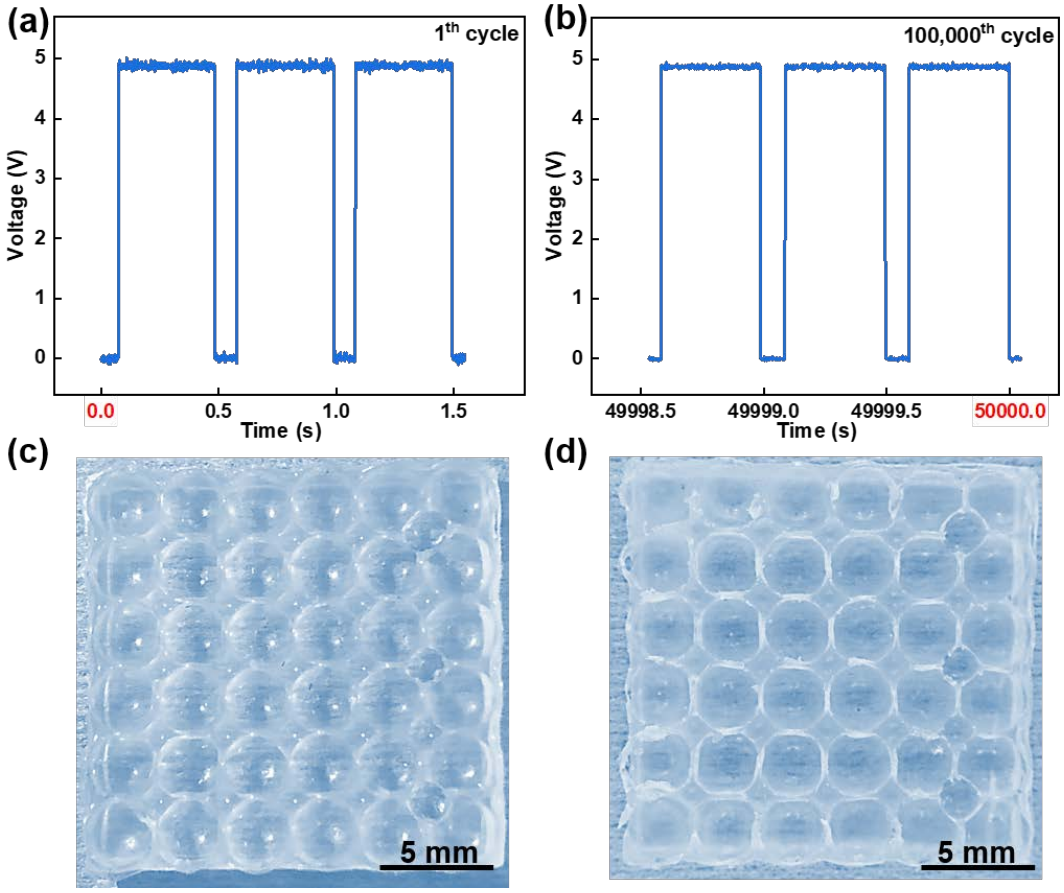


**Figure 5.14** Voltage output of AFE circuit over (a) the first few cycles, (b) the 100,000$^{th}$ few cycles. Photographs (c) before and (d) after the 100,000$^{th}$ cycle (scale bar, 5 mm).

With the on-demand connection design of the system, **Figure 5.12**e points out the working current during three working conditions, which includes the advertising period, connecting period and data transferring period, highlighted by yellow, green and blue, respectively. The DAQP module is in a low-power state with a current of 4 mA during

the advertising period, when requesting a connection with external Bluetooth devices. After a quick interval of connection establishment, transfer of the counting steps to one's smartphone could start. During the data transferring period, the Bluetooth data is converted with the frequency of people's movement, producing an average current of 3.5 mA and a peak current consumption of 6.62 and 8.82 mA for 180 ms.

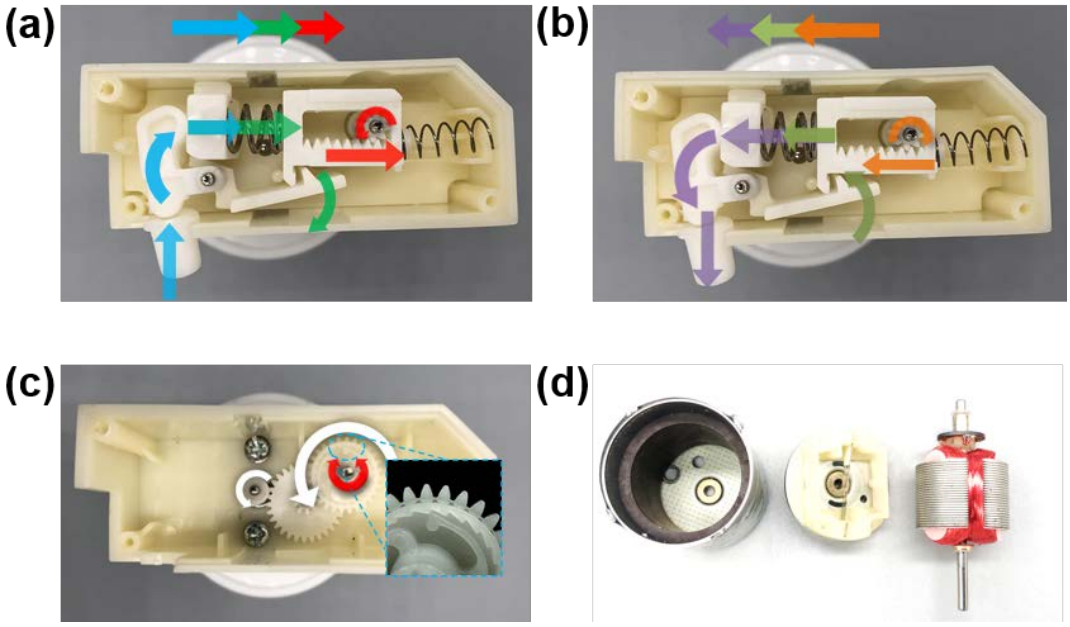


**Figure 5.15** The internal structure of the electromagnetic generator (EMG) with a linear-to-spinning gear mechanism and working principle of (a) triggering rotation, (b) mechanism reset and (c) mono-orientation rotation. (d) Internal structure of the EMG.

To implement a self-powered pedometer system, a press-to-spin type EMG with a linear-to-spinning gear mechanism could harvest mechanical energy from people's walking.[126, 149] **Figure 5.15** presents the internal structure of the EMG with a linear-to-spinning gear mechanism. The peak voltage of EMG could reach 3.5 V under one press. With an intrinsic resistance of 115 Ω, the EMG assemble could hold a peak power of $1.06*10^5$ μW as summarized in **Table 5.1**.

**Table 5.1** Parameters for EMG.

| Parameter | Value |
|---|---|
| Weight | 49.311 g |
| Volume | 9.5 $cm^3$ |
| Intrinsic resistance | 115 Ω |
| Peak voltage | 3.5 V |
| Peak power | $1.06*10^5$ μW |
| Peak power density/volume | $1.12*10^4$ μW/$cm^3$ |
| Peak power density/weight | $2.15*10^3$ μW/g |

The DAQP and Bluetooth device starts to maintain normal working status when power source voltage reaches around 2.37 V, which could be achieved by 2295 steps from the EMG (**Figure 5.16**).

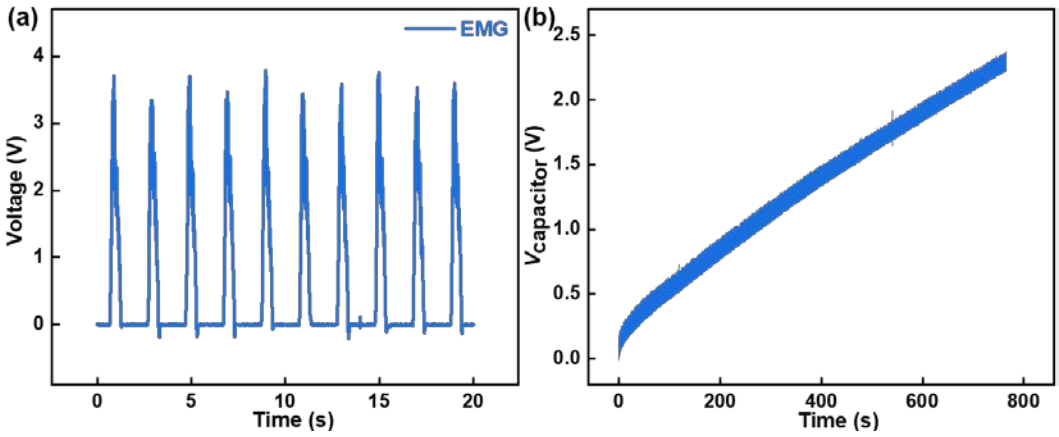


**Figure 5.16** (a) the voltage output of the electromagnetic generator (EMG), (b) Threshold voltage reached by the EMG for Bluetooth connection at 3 Hz.

In the systematic tests, the supercapacitor was pre-charged to 2.37 V where the pedometer system could exactly start counting and data transmission. Then both the

EMG and the P-TENG were driven with a linear motor at 2 Hz. The corresponding waveform is shown in **Figure 5.12**f, where it is obvious that the voltage on the supercapacitor was kept stably at around 2.4 V and the system could fulfill self-powered and self-sustained operation. The counts displayed on the smartphone alters in real-time when the whole system working at 2 Hz approximately equals to the pace of jogging. Namely, the systematic integrated pedometer system could be confirmed to achieve the power balance of supply and demand without an external power source.

## 5.4 Conclusion

In summary, an integrated self-powered real-time pedometer system with ultrafast response and high accuracy was built and demonstrated based on TENG. The P-TENGs were manufactured cost-effectively and fit well to the under-foot pedometer application with high stretchability because of the porous design and use of silicon rubber as a dielectric layer. Considering the P-TENGs' outputs varied in voltage according to the force applied and changed in current with frequencies, the amplifier circuit was designed to clamp the voltage at 3.98 V as well as amplifying the current of P-TENG for signal detection. Utilizing a monostable trigger circuit, stable signal with only high (logic 1, approximately 5 V) and low (logic 0, approximately 0 V) level outputs are acquired, neglecting the deviations in P-TENG due to changes in the excitation source. In addition to these, the AFE circuits dramatically decrease response and recovery time to 8 ms of the sensor signal and solving the painful problem of TENG impedance matching in step counting application. More attractively, the pedometer possesses low

power consumption due to the characteristic of on-demand connection. Provided that an auxiliary EMG is utilized to charge the supercapacitor, the integrated pedometer system could continuously work at 2 Hz without any other external power supply. Thus, a complete self-powered real-time pedometer system consisting of signal generation, transduction, processing, wireless transmission was achieved by the hybrid integration of TENG and EMG. This work demonstrates an example to regulate the TENG signals by electronic circuit design for more stable, accurate and repeatable applications, enlightening upgraded appliances such as sports biological data acquisition and sports goods design.

# CHAPTER 6 Conclusion and Perspective

## 6.1 Main Conclusion

Due to existing problems such as low charge density, poor stability, high-voltage and low-current characteristics, TENG needs to be continuously refined in theoretical framework and engineering manufacturing. In the thesis, the theoretical framework of a CS-TENG in Cartesian coordinate system was reconstructed to describe the distance-dependent electric field. The quantitative mathematical relationships between fundamental output performance and individual parameters were derived to reveal influence patterns. Among all the previous work, the output of the QETD model shows the best consistency with experimental data, providing a more accurate forecast of TENG's output performance.

Afterwards, to avoid surface charge decay, a MXene/$TiO_2$ hybrid layer was prepared as an intermediate layer to improve the stability of TENG. Surface terminals in MXene nanosheets and oxygen vacancies in $TiO_2$ nanoparticles provide abundant electron trap sites to trap electrons. $TiO_2$ nanoparticles could also enhance polarization to create more induced charges in electrodes. The optimized MT-TENG possesses the electric outputs of 128 $\mu C/m^2$ in charge density, 73.78 $\mu W/cm^3$ and 63.78 $\mu W/g$ in average power density with an energy conversion efficiency of 34.81%. According to the charge recombination model, the MT-TENG with an intermediate layer maintains a charge dynamic equilibrium with a charge density of 80 $\mu C/m^2$. It paves a new approach to reduce charge recombination, providing a promising way to maintain the surface charge

density of TENG.

Furthermore, limit equations under the restriction of air breakdown were constructed to answer the theoretical boundary of CS-TENG's surface charge density. The maximum surface charge density of TENGs drops with the increasing separation distance before air breakdown, and reaches a saturated constant value once air breakdown occurs. Thinner dielectric layers with higher relative permittivity help achieve superior surface charge density. After modelling and simulation, $\sigma_m$ and $E_{em}$ of TENG with 10 μm silicone rubber reach 2.85 mC/m$^2$ and 1.12 mJ, respectively.

Eventually, TENG's high-voltage and low-current outputs were regulated by an analogue front-end (AFE) circuit to work as the sensor for pedometers. TENG converts the mechanical energy of the human walking into electrical signals. Then, the electrical signals were controlled by the AFE circuit to 5 V regardless of the frequency and weight, with an ultrafast response time of 8 ms for triggering. Due to the on-demand connection in this system, a sustainable real-time pedometer was completed for step counting.

## 6.2 Future Work and Outlook

TENG has become a multidisciplinary research direction and has caught the attention of lots of researchers. According to the findings and shortcomings of the thesis, I propose some future work as follows:

First of all, although the working mechanism of TENG starts from triboelectrification, the reason for charge generation remains a mystery. This greatly affects the value of triboelectric charges accumulated after each contact electrification. In our test,

transferred charges can be easily obtained, but it is hard to obtain the amount of triboelectric charges directly. Until now, there has been no way to calculate the triboelectric charges on the dielectric layer surface. Therefore, more test methods and calculations need to be developed to discuss TENG's charge generation process.

Moreover, almost all the electrical measurement systems of TENG are based on the electrometer 6514 or oscilloscopes. Consequently, there must be an impedance mismatch between the TENG and test system. In addition, triboelectric discharge would happen during the separation movement, causing a rapid reduction in surface charge density. For these reasons, TENG's tested electrical output greatly differs from theoretical simulations. Therefore, more accurate and appropriate test methods need to be built to take into account the output characteristics of the TENG.

In addition, parameter-specific simulations for TENGs are equally important. In experiments, trial and error methods are often used to select suitable materials and conditions. Controlled variable methods are utilized to investigate the effects of different variables on the output performance of TENG. These require a significant investment of time and costs, and result in a waste of experimental resources. If we carry out simulations prior to the experiments, the whole process could be observed and optimal structure and parameters could be sought. Therefore, the finite element calculation modules for multi-physics field coupling and field-circuit coupling should be developed. Using models to reproduce the essential processes occurring in the actual environment has become an effective method for accurately predicting the output

performance of the TENG.

In conclusion, TENG is regarded as a new energy source that brings us great surprises and hope, but it also faces many challenges and problems in its practical application. As it evolved, multiple disciplines were utilized, including physical modelling, mathematical optimization, material engineering and electronic circuit design. Refining the theoretical framework and excavating optimization approaches are worthy of ongoing work to promote TENG's efficient development and use. The rapid advance of TENG will build a foundation for self-powered systems and promote the future development of energy harvesting and sensing technologies.

## LIST OF PUBLICATIONS

(1) **Chen, X.**; Zhang, F; Han, C.; Liu, Y; Chen, G; Sun, X.; Wen, Z. Quasi-electrostatic three-dimensional charge model for contact-separation triboelectric nanogenerator. Nano Energy 2023, 111, 108435, DOI: 10.1016/j.nanoen.2023.108435.

(2) **Chen, X.**; Han, C.; Wen, Z.; Liu, Y. Theoretical Boundary and Optimization Methodology of Contact-separation Triboelectric Nanogenerator. Applied Materials Today 2022, 29, DOI: 10.1016/j.apmt.2022.101685.

(3) **Chen, X.**; Liu, Y.; Sun, Y.; Zhao, T.; Zhao, C.; Khattab, T. A.; Lim, E. G.; Sun, X.; Wen, Z. Electron Trapping & blocking Effect Enabled by MXene/TiO2 Intermediate Layer for Charge Regulation of Triboelectric Nanogenerators. Nano Energy 2022, 98, 107236, DOI: 10.1016/j.nanoen.2022.107236.

(4) **Chen, X.**; Li, J.; Liu, Y.; Jiang, J.; Zhao, C.; Zhao, C.; Lim, E. G.; Sun, X.; Wen, Z. An Integrated Self-Powered Real-Time Pedometer System with Ultrafast Response and High Accuracy. ACS Appl Mater Interfaces 2021, 13 (51), 61789-61798, DOI: 10.1021/acsami.1c19734.

(5) **Chen, X.**; Xie, X.; Liu, Y.; Zhao, C.; Wen, M.; Wen, Z. Advances in Healthcare Electronics Enabled by Triboelectric Nanogenerators. Adv. Funct. Mater. 2020, 30 (43), DOI: 10.1002/adfm.202004673.

(6) Xie, X.; **Chen, X.**; Zhao, C.; Liu, Y.; Sun, X.; Zhao, C..; Wen, Z. Intermediate Layer for Enhanced Triboelectric Nanogenerator. Nano Energy 2021, 79, 105439, DOI: 10.1016/j.nanoen.2020.105439.

(7) Zhai, N.; Wen, Z.; **Chen, X.**; Wei, A.; Sha, M.; Fu, J.; Liu, Y.; Zhong, J.; Sun, X. Blue Energy Collection toward All-Hours Self-Powered Chemical Energy Conversion. Adv Energy Mater 2020, 10 (33), DOI: 10.1002/aenm.202001041.

(8) Xie, X.; Zhang, Y.; Chen, C.; **Chen, X.**; Yao, T.; Peng, M.; Chen, X.; Nie, B.; Wen, Z.; Sun, X. Frequency-independent Self-powered Sensing Based on Capacitive Impedance Matching Effect of Triboelectric Nanogenerator. Nano Energy 2019, 65, DOI:10.1016/j.nanoen.2019.103984.

(9) Xie, L.; **Chen, X.**; Wen, Z.; Yang, Y.; Shi, J.; Chen, C.; Peng, M.; Liu, Y.; Sun, X. Spiral Steel Wire Based Fiber-Shaped Stretchable and Tailorable Triboelectric Nanogenerator for Wearable Power Source and Active Gesture Sensor. Nano Micro Lett 2019, 11 (1), 39, DOI: 10.1007/s40820-019-0271-3.

(10) Shi, J.; **Chen, X.**; Li, G.; Sun, N.; Jiang, H.; Bao, D.; Xie, L.; Peng, M.; Liu, Y.; Wen, Z.; Sun, X. A Liquid PEDOT:PSS Electrode-based Stretchable Triboelectric Nanogenerator for a Portable Self-charging Power Source. Nanoscale 2019, 11 (15), 7513-7519, DOI: 10.1039/c9nr01271k.

(11) Zhou, C.; Yang, Y.; Sun, N.; Wen, Z.; Cheng, P.; Xie, X.; Shao, H.; Shen, Q.; **Chen, X.**; Liu, Y.; Wang, Z.; Sun, X. Flexible Self-charging Power Units for Portable Electronics Based on Folded Carbon Paper. Nano Res 2018, 11 (8), 4313-4322, DOI: 10.1007/s12274-018-2018-8.

(12) Xie, X.; Wen, Z.; Shen, Q.; Chen, C.; Peng, M.; Yang, Y.; Sun, N.; Cheng, P.; Shao, H.; Zhang, Y.; Zhu, Q.; **Chen, X.**; Sun, X. Impedance Matching Effect between a

Triboelectric Nanogenerator and a Piezoresistive Pressure Sensor Induced Self-Powered Weighing. Advanced Materials Technologies 2018, 3 (6), 1800054, DOI: 10.1002/admt.201800054.

(13) Shao, H.; Cheng, P.; Chen, R.; Xie, L.; Sun, N.; Shen, Q.; **Chen, X.**; Zhu, Q.; Zhang, Y.; Liu, Y.; Wen, Z.; Sun, X. Triboelectric-Electromagnetic Hybrid Generator for Harvesting Blue Energy. Nano Micro Lett 2018, 10 (3), 54, DOI: 10.1007/s40820-018-0207-3.

## REFERENCE

(1) Kaspar, C.; Ravoo, B. J.; van der Wiel, W. G.; Wegner, S. V.; Pernice, W. H. P. The rise of intelligent matter. *Nature* **2021,** *594* (7863), 345-355, DOI: 10.1038/s41586-021-03453-y.

(2) Wang, Z. H.; Jin, Y. C.; Lu, C. Y.; Wang, J. Y.; Song, Z. W.; Yang, X.; Cao, Y. D.; Zi, Y. L.; Wang, Z. L.; Ding, W. B. Triboelectric-nanogenerator-enabled mechanical modulation for infrared wireless communications. *Energy & Environmental Science* **2022,** *15* (7), 2983-2991, DOI: 10.1039/d2ee00900e.

(3) Zi, Y.; Guo, H.; Wen, Z.; Yeh, M. H.; Hu, C.; Wang, Z. L. Harvesting Low-Frequency (<5 Hz) Irregular Mechanical Energy: A Possible Killer Application of Triboelectric Nanogenerator. *ACS Nano* **2016,** *10* (4), 4797-805, DOI: 10.1021/acsnano.6b01569.

(4) Fan, F. R.; Tian, Z. Q.; Wang, Z. L. Flexible triboelectric generator! *Nano Energy* **2012,** *1* (2), 328-334, DOI: 10.1016/j.nanoen.2012.01.004.

(5) Zhang, H.; Marty, F.; Xia, X.; Zi, Y.; Bourouina, T.; Galayko, D.; Basset, P. Employing a MEMS plasma switch for conditioning high-voltage kinetic energy harvesters. *Nat Commun* **2020,** *11* (1), 3221, DOI: 10.1038/s41467-020-17019-5.

(6) Xiong, J.; Cui, P.; Chen, X.; Wang, J.; Parida, K.; Lin, M. F.; Lee, P. S. Skin-touch-actuated textile-based triboelectric nanogenerator with black phosphorus for durable biomechanical energy harvesting. *Nat Commun* **2018,** *9* (1), 4280, DOI: 10.1038/s41467-018-06759-0.

(7) Zhai, N. N.; Wen, Z.; Chen, X. P.; Wei, A. M.; Sha, M.; Fu, J. J.; Liu, Y. N.; Zhong, J.; Sun, X. H. Blue Energy Collection toward All-Hours Self-Powered Chemical Energy Conversion. *Adv Energy Mater* **2020,** *10* (33), DOI: 10.1002/aenm.202001041.

(8) Zhao, Y.; Gao, W.; Dai, K.; Wang, S.; Yuan, Z.; Li, J.; Zhai, W.; Zheng, G.; Pan, C.; Liu, C.; Shen, C. Bioinspired Multifunctional Photonic-Electronic Smart Skin for Ultrasensitive Health Monitoring, for Visual and Self-Powered Sensing. *Adv. Mater.*

**2021,** *33* (45), e2102332, DOI: 10.1002/adma.202102332.

(9) Lee, Y.; Lim, S.; Song, W. J.; Lee, S.; Yoon, S. J.; Park, J. M.; Lee, M. G.; Park, Y. L.; Sun, J. Y. Triboresistive Touch Sensing: Grid-Free Touch-Point Recognition Based on Monolayered Ionic Power Generators. *Adv. Mater.* **2022,** *34* (19), e2108586, DOI: 10.1002/adma.202108586.

(10) Shi, Q.; Sun, Z.; Zhang, Z.; Lee, C. Triboelectric Nanogenerators and Hybridized Systems for Enabling Next-Generation IoT Applications. *Research (Wash D C)* **2021,** *2021*, 6849171, DOI: 10.34133/2021/6849171.

(11) Zi, Y. L.; Wang, Z. L. Nanogenerators: An emerging technology towards nanoenergy. *Apl Materials* **2017,** *5* (7), DOI: 10.1063/1.4977208.

(12) Pan, S.; Zhang, Z. Fundamental theories and basic principles of triboelectric effect: A review. *Friction* **2018,** *7* (1), 2-17, DOI: 10.1007/s40544-018-0217-7.

(13) Kim, S.; Seol, D.; Lu, X.; Alexe, M.; Kim, Y. Electrostatic-free piezoresponse force microscopy. *Sci Rep* **2017,** *7*, 41657, DOI: 10.1038/srep41657.

(14) Matsusaka, S.; Maruyama, H.; Matsuyama, T.; Ghadiri, M. Triboelectric charging of powders: A review. *Chem. Eng. Sci.* **2010,** *65* (22), 5781-5807, DOI: 10.1016/j.ces.2010.07.005.

(15) Xu, C.; Zi, Y.; Wang, A. C.; Zou, H.; Dai, Y.; He, X.; Wang, P.; Wang, Y. C.; Feng, P.; Li, D.; Wang, Z. L. On the Electron-Transfer Mechanism in the Contact-Electrification Effect. *Adv. Mater.* **2018,** *30* (15), e1706790, DOI: 10.1002/adma.201706790.

(16) Ko, H.; Lim, Y. W.; Han, S.; Jeong, C. K.; Cho, S. B. Triboelectrification: Backflow and Stuck Charges Are Key. *Acs Energy Letters* **2021,** *6* (8), 2792-2799, DOI: 10.1021/acsenergylett.1c01019.

(17) Wang, Z. L. On Maxwell's displacement current for energy and sensors: the origin of nanogenerators. *Mater. Today* **2017,** *20* (2), 74-82, DOI: 10.1016/j.mattod.2016.12.001.

(18) Shao, J. J.; Willatzen, M.; Wang, Z. L. Theoretical modeling of triboelectric

nanogenerators (TENGs). *J. Appl. Phys.* **2020,** *128* (11), 111101, DOI: Artn 111101 10.1063/5.0020961.

(19) Shao, J. J.; Willatzen, M.; Shi, Y. J.; Wang, Z. L. 3D mathematical model of contact-separation and single-electrode mode triboelectric nanogenerators. *Nano Energy* **2019,** *60*, 630-640, DOI: 10.1016/j.nanoen.2019.03.072.

(20) Shao, J. J.; Liu, D.; Willatzen, M.; Wang, Z. L. Three-dimensional modeling of alternating current triboelectric nanogenerator in the linear sliding mode. *Applied Physics Reviews* **2020,** *7* (1), DOI: 10.1063/1.5133023.

(21) Zhang, H.; Quan, L.; Chen, J.; Xu, C.; Zhang, C.; Dong, S.; Lü, C.; Luo, J. A general optimization approach for contact-separation triboelectric nanogenerator. *Nano Energy* **2019,** *56*, 700-707, DOI: 10.1016/j.nanoen.2018.11.062.

(22) Dharmasena, R. D. I. G.; Jayawardena, K. D. G. I.; Mills, C. A.; Deane, J. H. B.; Anguita, J. V.; Dorey, R. A.; Silva, S. R. P. Triboelectric nanogenerators: providing a fundamental framework. *Energy & Environmental Science* **2017,** *10* (8), 1801-1811, DOI: 10.1039/c7ee01139c.

(23) Dharmasena, R. D. I. G.; Jayawardena, K. D. G. I.; Mills, C. A.; Dorey, R. A.; Silva, S. R. P. A unified theoretical model for Triboelectric Nanogenerators. *Nano Energy* **2018,** *48*, 391-400, DOI: 10.1016/j.nanoen.2018.03.073.

(24) Niu, S. M.; Wang, S. H.; Lin, L.; Liu, Y.; Zhou, Y. S.; Hu, Y. F.; Wang, Z. L. Theoretical study of contact-mode triboelectric nanogenerators as an effective power source. *Energy & Environmental Science* **2013,** *6* (12), 3576-3583, DOI: 10.1039/c3ee42571a.

(25) Niu, S.; Liu, Y.; Wang, S.; Lin, L.; Zhou, Y. S.; Hu, Y.; Wang, Z. L. Theoretical Investigation and Structural Optimization of Single-Electrode Triboelectric Nanogenerators. *Adv. Funct. Mater.* **2014,** *24* (22), 3332-3340, DOI: 10.1002/adfm.201303799.

(26) Niu, S.; Wang, S.; Liu, Y.; Zhou, Y. S.; Lin, L.; Hu, Y.; Pradel, K. C.; Wang, Z. L. A theoretical study of grating structured triboelectric nanogenerators. *Energy Environ.*

*Sci.* **2014,** *7* (7), 2339-2349, DOI: 10.1039/c4ee00498a.

(27) Niu, S. M.; Wang, Z. L. Theoretical systems of triboelectric nanogenerators. *Nano Energy* **2015,** *14*, 161-192, DOI: 10.1016/j.nanoen.2014.11.034.

(28) Li, X. Y.; Lau, T. H.; Guan, D.; Zi, Y. L. A universal method for quantitative analysis of triboelectric nanogenerators. *Journal of Materials Chemistry A* **2019,** *7* (33), 19485-19494, DOI: 10.1039/c9ta06525c.

(29) Dharmasena, R. D. I. G.; Deane, J. H. B.; Silva, S. R. P. Nature of Power Generation and Output Optimization Criteria for Triboelectric Nanogenerators. *Adv Energy Mater* **2018,** *8* (31), DOI: 10.1002/aenm.201802190.

(30) Wang, Z. L. On the first principle theory of nanogenerators from Maxwell's equations. *Nano Energy* **2020,** *68*, DOI: 10.1016/j.nanoen.2019.104272.

(31) Shao, J. J.; Willatzen, M.; Jiang, T.; Tang, W.; Chen, X. Y.; Wang, J.; Wang, Z. L. Quantifying the power output and structural figure-of-merits of triboelectric nanogenerators in a charging system starting from the Maxwell's displacement current. *Nano Energy* **2019,** *59*, 380-389, DOI: 10.1016/j.nanoen.2019.02.051.

(32) Zhao, H.; Xu, M.; Shu, M.; An, J.; Ding, W.; Liu, X.; Wang, S.; Zhao, C.; Yu, H.; Wang, H.; Wang, C.; Fu, X.; Pan, X.; Xie, G.; Wang, Z. L. Underwater wireless communication via TENG-generated Maxwell's displacement current. *Nat Commun* **2022,** *13* (1), 3325, DOI: 10.1038/s41467-022-31042-8.

(33) Zhang, C. L.; Zhou, L. L.; Cheng, P.; Yin, X.; Liu, D.; Li, X. Y.; Guo, H. Y.; Wang, Z. L.; Wang, J. Surface charge density of triboelectric nanogenerators: Theoretical boundary and optimization methodology. *Applied Materials Today* **2020,** *18*, 100496, DOI: 10.1016/j.apmt.2019.100496.

(34) Choi, Y. S.; Kim, S. W.; Kar-Narayan, S. Materials-Related Strategies for Highly Efficient Triboelectric Energy Generators. *Adv Energy Mater* **2021,** *11* (7), 2003802, DOI: 10.1002/aenm.202003802.

(35) Zou, H.; Guo, L.; Xue, H.; Zhang, Y.; Shen, X.; Liu, X.; Wang, P.; He, X.; Dai, G.; Jiang, P.; Zheng, H.; Zhang, B.; Xu, C.; Wang, Z. L. Quantifying and understanding the

triboelectric series of inorganic non-metallic materials. *Nat Commun* **2020,** *11* (1), 2093, DOI: 10.1038/s41467-020-15926-1.

(36) Li, Z. H.; Xu, B. G.; Han, J.; Huang, J. X.; Chung, K. Y. Interfacial Polarization and Dual Charge Transfer Induced High Permittivity of Carbon Dots-Based Composite as Humidity-Resistant Tribomaterial for Efficient Biomechanical Energy Harvesting. *Adv Energy Mater* **2021,** *11* (30), 2101294, DOI: 10.1002/aenm.202101294.

(37) Lee, J. W.; Jung, S.; Jo, J.; Han, G. H.; Lee, D.-M.; Oh, J.; Hwang, H. J.; Choi, D.; Kim, S.-W.; Lee, J. H.; Yang, C.; Baik, J. M. Sustainable highly charged C60-functionalized polyimide in a non-contact mode triboelectric nanogenerator. *Energy & Environmental Science* **2021,** *14* (2), 1004-1015, DOI: 10.1039/d0ee03057k.

(38) Chen, J.; Guo, H.; He, X.; Liu, G.; Xi, Y.; Shi, H.; Hu, C. Enhancing Performance of Triboelectric Nanogenerator by Filling High Dielectric Nanoparticles into Sponge PDMS Film. *ACS Appl Mater Interfaces* **2016,** *8* (1), 736-44, DOI: 10.1021/acsami.5b09907.

(39) Xie, X. K.; Chen, X. P.; Zhao, C.; Liu, Y. N.; Sun, X. H.; Zhao, C. Z.; Wen, Z. Intermediate layer for enhanced triboelectric nanogenerator. *Nano Energy* **2021,** *79*, 105439, DOI: 10.1016/j.nanoen.2020.105439.

(40) Chen, X.; Liu, Y.; Sun, Y.; Zhao, T.; Zhao, C.; Khattab, T. A.; Lim, E. G.; Sun, X.; Wen, Z. Electron trapping & blocking effect enabled by MXene/TiO2 intermediate layer for charge regulation of triboelectric nanogenerators. *Nano Energy* **2022,** *98*, 107236, DOI: 10.1016/j.nanoen.2022.107236.

(41) Wang, S.; Xie, Y.; Niu, S.; Lin, L.; Liu, C.; Zhou, Y. S.; Wang, Z. L. Maximum surface charge density for triboelectric nanogenerators achieved by ionized-air injection: methodology and theoretical understanding. *Adv. Mater.* **2014,** *26* (39), 6720-8, DOI: 10.1002/adma.201402491.

(42) He, W. C.; Shan, C. C.; Wu, H. Y.; Fu, S. K.; Li, Q. Y.; Li, G.; Zhang, X. M.; Du, Y.; Wang, J.; Wang, X.; Hu, C. G. Capturing Dissipation Charge in Charge Space Accumulation Area for Enhancing Output Performance of Sliding Triboelectric

Nanogenerator. *Adv Energy Mater* **2022,** *12* (31), 2201454, DOI: 10.1002/aenm.202201454.

(43) Liu, Z.; Huang, Y.; Shi, Y.; Tao, X.; He, H.; Chen, F.; Huang, Z. X.; Wang, Z. L.; Chen, X.; Qu, J. P. Fabrication of triboelectric polymer films via repeated rheological forging for ultrahigh surface charge density. *Nat Commun* **2022,** *13* (1), 4083, DOI: 10.1038/s41467-022-31822-2.

(44) Fu, J.; Xu, G.; Li, C.; Xia, X.; Guan, D.; Li, J.; Huang, Z.; Zi, Y. Achieving Ultrahigh Output Energy Density of Triboelectric Nanogenerators in High-Pressure Gas Environment. *Adv Sci (Weinh)* **2020,** *7* (24), 2001757, DOI: 10.1002/advs.202001757.

(45) Liu, D.; Zhou, L.; Cui, S.; Gao, Y.; Li, S.; Zhao, Z.; Yi, Z.; Zou, H.; Fan, Y.; Wang, J.; Wang, Z. L. Standardized measurement of dielectric materials' intrinsic triboelectric charge density through the suppression of air breakdown. *Nat Commun* **2022,** *13* (1), 6019, DOI: 10.1038/s41467-022-33766-z.

(46) Cui, N.; Gu, L.; Lei, Y.; Liu, J.; Qin, Y.; Ma, X.; Hao, Y.; Wang, Z. L. Dynamic Behavior of the Triboelectric Charges and Structural Optimization of the Friction Layer for a Triboelectric Nanogenerator. *ACS Nano* **2016,** *10* (6), 6131-8, DOI: 10.1021/acsnano.6b02076.

(47) Wu, H.; He, W.; Shan, C.; Wang, Z.; Fu, S.; Tang, Q.; Guo, H.; Du, Y.; Liu, W.; Hu, C. Achieving Remarkable Charge Density via Self-Polarization of Polar High-k Material in a Charge-Excitation Triboelectric Nanogenerator. *Adv. Mater.* **2022,** *34* (13), e2109918, DOI: 10.1002/adma.202109918.

(48) Zi, Y.; Niu, S.; Wang, J.; Wen, Z.; Tang, W.; Wang, Z. L. Standards and figure-of-merits for quantifying the performance of triboelectric nanogenerators. *Nat Commun* **2015,** *6*, 8376, DOI: 10.1038/ncomms9376.

(49) Xia, X.; Fu, J.; Zi, Y. A universal standardized method for output capability assessment of nanogenerators. *Nat Commun* **2019,** *10* (1), 4428, DOI: 10.1038/s41467-019-12465-2.

(50) Wang, S.; Xie, Y.; Niu, S.; Lin, L.; Liu, C.; Zhou, Y. S.; Wang, Z. L. Maximum Surface Charge Density for Triboelectric Nanogenerators Achieved by Ionized-Air Injection: Methodology and Theoretical Understanding. *Adv. Mater.* **2014,** *26* (39), 6720-6728, DOI: 10.1002/adma.201402491.

(51) Zhang, C.; Zhou, L.; Cheng, P.; Yin, X.; Liu, D.; Li, X.; Guo, H.; Wang, Z. L.; Wang, J. Surface charge density of triboelectric nanogenerators: Theoretical boundary and optimization methodology. *Appl. Mater. Today* **2020,** *18*, 100496, DOI: 10.1016/j.apmt.2019.100496.

(52) Maystre, D. Maxwell: A new vision of the world. *Comptes Rendus Physique* **2014,** *15* (5), 387-392, DOI: 10.1016/j.crhy.2014.02.004.

(53) Wang, Z. L. From contact electrification to triboelectric nanogenerators. *Rep. Prog. Phys.* **2021,** *84* (9), 096502, DOI: 10.1088/1361-6633/ac0a50.

(54) Wang, S.; Lin, L.; Wang, Z. L. Nanoscale triboelectric-effect-enabled energy conversion for sustainably powering portable electronics. *Nano Lett.* **2012,** *12* (12), 6339-46, DOI: 10.1021/nl303573d.

(55) Hinchet, R.; Yoon, H. J.; Ryu, H.; Kim, M. K.; Choi, E. K.; Kim, D. S.; Kim, S. W. Transcutaneous ultrasound energy harvesting using capacitive triboelectric technology. *Science* **2019,** *365* (6452), 491-494, DOI: 10.1126/science.aan3997.

(56) Zhou, Y. S.; Wang, S.; Yang, Y.; Zhu, G.; Niu, S.; Lin, Z. H.; Liu, Y.; Wang, Z. L. Manipulating nanoscale contact electrification by an applied electric field. *Nano Lett.* **2014,** *14* (3), 1567-72, DOI: 10.1021/nl404819w.

(57) Shao, J. J.; Jiang, T.; Wang, Z. L. Theoretical foundations of triboelectric nanogenerators (TENGs). *Science China-Technological Sciences* **2020,** *63* (7), 1087-1109, DOI: 10.1007/s11431-020-1604-9.

(58) Shao, J. J.; Jiang, T.; Tang, W.; Chen, X. Y.; Xu, L.; Wang, Z. L. Structural figure-of-merits of triboelectric nanogenerators at powering loads. *Nano Energy* **2018,** *51*, 688-697, DOI: 10.1016/j.nanoen.2018.07.032.

(59) Chen, C.; Wen, Z.; Shi, J.; Jian, X.; Li, P.; Yeow, J. T. W.; Sun, X. Micro

triboelectric ultrasonic device for acoustic energy transfer and signal communication. *Nat Commun* **2020,** *11* (1), 4143, DOI: 10.1038/s41467-020-17842-w.

(60) Yang, Y.; Sun, N.; Wen, Z.; Cheng, P.; Zheng, H.; Shao, H.; Xia, Y.; Chen, C.; Lan, H.; Xie, X.; Zhou, C.; Zhong, J.; Sun, X.; Lee, S. T. Liquid-Metal-Based Super-Stretchable and Structure-Designable Triboelectric Nanogenerator for Wearable Electronics. *ACS Nano* **2018,** *12* (2), 2027-2034, DOI: 10.1021/acsnano.8b00147.

(61) Guo, H.; Pu, X.; Chen, J.; Meng, Y.; Yeh, M. H.; Liu, G.; Tang, Q.; Chen, B.; Liu, D.; Qi, S.; Wu, C.; Hu, C.; Wang, J.; Wang, Z. L. A highly sensitive, self-powered triboelectric auditory sensor for social robotics and hearing aids. *Sci Robot* **2018,** *3* (20), DOI: 10.1126/scirobotics.aat2516.

(62) Lai, Y. C.; Deng, J.; Liu, R.; Hsiao, Y. C.; Zhang, S. L.; Peng, W.; Wu, H. M.; Wang, X.; Wang, Z. L. Actively Perceiving and Responsive Soft Robots Enabled by Self-Powered, Highly Extensible, and Highly Sensitive Triboelectric Proximity- and Pressure-Sensing Skins. *Adv. Mater.* **2018,** *30* (28), e1801114, DOI: 10.1002/adma.201801114.

(63) Chen, C. Y.; Chen, L. J.; Wu, Z. Y.; Guo, H. Y.; Yu, W. D.; Du, Z. Q.; Wang, Z. L. 3D double-faced interlock fabric triboelectric nanogenerator for bio-motion energy harvesting and as self-powered stretching and 3D tactile sensors. *Mater. Today* **2020,** *32*, 84-93, DOI: 10.1016/j.mattod.2019.10.025.

(64) Yao, G.; Xu, L.; Cheng, X. W.; Li, Y. Y.; Huang, X.; Guo, W.; Liu, S. Y.; Wang, Z. L.; Wu, H. Bioinspired Triboelectric Nanogenerators as Self-Powered Electronic Skin for Robotic Tactile Sensing. *Adv. Funct. Mater.* **2020,** *30* (6), DOI: 10.1002/adfm.201907312.

(65) Miao, L.; Wan, J.; Song, Y.; Guo, H.; Chen, H.; Cheng, X.; Zhang, H. Skin-Inspired Humidity and Pressure Sensor with a Wrinkle-on-Sponge Structure. *ACS Appl Mater Interfaces* **2019,** *11* (42), 39219-39227, DOI: 10.1021/acsami.9b13383.

(66) Tao, J.; Bao, R.; Wang, X.; Peng, Y.; Li, J.; Fu, S.; Pan, C.; Wang, Z. L. Self-Powered Tactile Sensor Array Systems Based on the Triboelectric Effect. *Adv. Funct.*

*Mater.* **2018,** *29* (41), 1806379, DOI: 10.1002/adfm.201806379.

(67) Chen, X.; Li, J.; Liu, Y.; Jiang, J.; Zhao, C.; Zhao, C.; Lim, E. G.; Sun, X.; Wen, Z. An Integrated Self-Powered Real-Time Pedometer System with Ultrafast Response and High Accuracy. *ACS Appl Mater Interfaces* **2021,** *13* (51), 61789-61798, DOI: 10.1021/acsami.1c19734.

(68) Li, X. Y.; Xu, G. Q.; Xia, X.; Fu, J. J.; Huang, L. B.; Zi, Y. L. Standardization of triboelectric nanogenerators: Progress and perspectives. *Nano Energy* **2019,** *56*, 40-55, DOI: 10.1016/j.nanoen.2018.11.029.

(69) Wang, Z. L.; Wang, A. C. On the origin of contact-electrification. *Mater. Today* **2019,** *30*, 34-51, DOI: 10.1016/j.mattod.2019.05.016.

(70) Kim, M.; Park, D.; Alam, M. M.; Lee, S.; Park, P.; Nah, J. Remarkable Output Power Density Enhancement of Triboelectric Nanogenerators via Polarized Ferroelectric Polymers and Bulk MoS2 Composites. *ACS Nano* **2019,** *13* (4), 4640-4646, DOI: 10.1021/acsnano.9b00750.

(71) Seung, W.; Yoon, H. J.; Kim, T. Y.; Ryu, H.; Kim, J.; Lee, J. H.; Lee, J. H.; Kim, S.; Park, Y. K.; Park, Y. J.; Kim, S. W. Boosting Power-Generating Performance of Triboelectric Nanogenerators via Artificial Control of Ferroelectric Polarization and Dielectric Properties. *Adv Energy Mater* **2017,** *7* (2), 1600988, DOI: 10.1002/aenm.201600988.

(72) Lee, K. Y.; Kim, S. K.; Lee, J. H.; Seol, D.; Gupta, M. K.; Kim, Y.; Kim, S. W. Controllable Charge Transfer by Ferroelectric Polarization Mediated Triboelectricity. *Adv. Funct. Mater.* **2016,** *26* (18), 3067-3073, DOI: 10.1002/adfm.201505088.

(73) Bai, P.; Zhu, G.; Zhou, Y. S.; Wang, S. H.; Ma, J. S.; Zhang, G.; Wang, Z. L. Dipole-moment-induced effect on contact electrification for triboelectric nanogenerators. *Nano Res* **2014,** *7* (7), 990-997, DOI: 10.1007/s12274-014-0461-8.

(74) Han, S. A.; Seung, W.; Kim, J. H.; Kim, S. W. Ultrathin Noncontact-Mode Triboelectric Nanogenerator Triggered by Giant Dielectric Material Adaption. *Acs Energy Letters* **2021,** *6* (4), 1189-1197, DOI: 10.1021/acsenergylett.0c02434.

(75) Xia, X.; Wang, H. Y.; Guo, H. Y.; Xu, C.; Zi, Y. L. On the material-dependent charge transfer mechanism of the contact electrification. *Nano Energy* **2020,** *78*, DOI: 10.1016/j.nanoen.2020.105343.

(76) Kim, D. W.; Lee, J. H.; You, I.; Kim, J. K.; Jeong, U. Adding a stretchable deep-trap interlayer for high-performance stretchable triboelectric nanogenerators. *Nano Energy* **2018,** *50*, 192-200, DOI: 10.1016/j.nanoen.2018.05.041.

(77) Park, H. W.; Huynh, N. D.; Kim, W.; Lee, C.; Nam, Y.; Lee, S.; Chung, K. B.; Choi, D. Electron blocking layer-based interfacial design for highly-enhanced triboelectric nanogenerators. *Nano Energy* **2018,** *50*, 9-15, DOI: 10.1016/j.nanoen.2018.05.024.

(78) Naguib, M.; Kurtoglu, M.; Presser, V.; Lu, J.; Niu, J.; Heon, M.; Hultman, L.; Gogotsi, Y.; Barsoum, M. W. Two-dimensional nanocrystals produced by exfoliation of Ti3 AlC2. *Adv. Mater.* **2011,** *23* (37), 4248-53, DOI: 10.1002/adma.201102306.

(79) Yang, L.; Kan, D. X.; Dall'Agnese, C.; Dall'Agnese, Y.; Wang, B. N.; Jena, A. K.; Wei, Y. J.; Chen, G.; Wang, X. F.; Gogotsi, Y.; Miyasaka, T. Performance improvement of MXene-based perovskite solar cells upon property transition from metallic to semiconductive by oxidation of Ti3C2Tx in air. *Journal of Materials Chemistry A* **2021,** *9* (8), 5016-5025, DOI: 10.1039/d0ta11397b.

(80) Li, Z.; Wang, P.; Ma, C.; Igbari, F.; Kang, Y.; Wang, K. L.; Song, W.; Dong, C.; Li, Y.; Yao, J.; Meng, D.; Wang, Z. K.; Yang, Y. Single-Layered MXene Nanosheets Doping TiO2 for Efficient and Stable Double Perovskite Solar Cells. *J. Am. Chem. Soc.* **2021,** *143* (6), 2593-2600, DOI: 10.1021/jacs.0c12739.

(81) Jiao, L.; Zhang, C.; Geng, C. N.; Wu, S. C.; Li, H.; Lv, W.; Tao, Y.; Chen, Z. J.; Zhou, G. M.; Li, J.; Ling, G. W.; Wan, Y.; Yang, Q. H. Capture and Catalytic Conversion of Polysulfides by In Situ Built TiO2-MXene Heterostructures for Lithium-Sulfur Batteries. *Adv Energy Mater* **2019,** *9* (19), DOI: 10.1002/aenm.201900219.

(82) Halim, J.; Cook, K. M.; Naguib, M.; Eklund, P.; Gogotsi, Y.; Rosen, J.; Barsoum, M. W. X-ray photoelectron spectroscopy of select multi-layered transition metal carbides (MXenes). *Appl. Surf. Sci.* **2016,** *362*, 406-417, DOI:

10.1016/j.apsusc.2015.11.089.

(83) Zhang, C. F. J.; Pinilla, S.; McEyoy, N.; Cullen, C. P.; Anasori, B.; Long, E.; Park, S. H.; Seral-Ascaso, A.; Shmeliov, A.; Krishnan, D.; Morant, C.; Liu, X. H.; Duesberg, G. S.; Gogotsi, Y.; Nicolosi, V. Oxidation Stability of Colloidal Two-Dimensional Titanium Carbides (MXenes). *Chem. Mater.* **2017,** *29* (11), 4848-4856, DOI: 10.1021/acs.chemmater.7b00745.

(84) Wang, F.; Yang, C.; Duan, M.; Tang, Y.; Zhu, J. TiO2 nanoparticle modified organ-like Ti3C2 MXene nanocomposite encapsulating hemoglobin for a mediator-free biosensor with excellent performances. *Biosens. Bioelectron.* **2015,** *74*, 1022-8, DOI: 10.1016/j.bios.2015.08.004.

(85) Li, Z. Y.; Wang, L. B.; Sun, D. D.; Zhang, Y. D.; Liu, B. Z.; Hu, Q. K.; Zhou, A. G. Synthesis and thermal stability of two-dimensional carbide MXene Ti3C2. *Materials Science and Engineering B-Advanced Functional Solid-State Materials* **2015,** *191*, 33-40, DOI: 10.1016/j.mseb.2014.10.009.

(86) He, W.; Sohn, M.; Ma, R. J.; Kang, D. J. Flexible single-electrode triboelectric nanogenerators with MXene/PDMS composite film for biomechanical motion sensors. *Nano Energy* **2020,** *78*, DOI: 10.1016/j.nanoen.2020.105383.

(87) Lipatov, A.; Alhabeb, M.; Lukatskaya, M. R.; Boson, A.; Gogotsi, Y.; Sinitskii, A. Effect of Synthesis on Quality, Electronic Properties and Environmental Stability of Individual Monolayer Ti3C2MXene Flakes. *Advanced Electronic Materials* **2016,** *2* (12), DOI: 10.1002/aelm.201600255.

(88) Ghassemi, H.; Harlow, W.; Mashtalir, O.; Beidaghi, M.; Lukatskaya, M. R.; Gogotsi, Y.; Taheri, M. L. In situ environmental transmission electron microscopy study of oxidation of two-dimensional Ti3C2and formation of carbon-supported TiO2. *Journal of Materials Chemistry A* **2014,** *2* (35), DOI: 10.1039/c4ta02583k.

(89) Jiang, H. X.; Lei, H.; Wen, Z.; Shi, J. H.; Bao, D. Q.; Chen, C.; Jiang, J. X.; Guan, Q. B.; Sun, X. H.; Lee, S. T. Charge-trapping-blocking layer for enhanced triboelectric nanogenerators. *Nano Energy* **2020,** *75*, 105011, DOI: 10.1016/j.nanoen.2020.105011.

(90) Mashtalir, O.; Naguib, M.; Mochalin, V. N.; Dall'Agnese, Y.; Heon, M.; Barsoum, M. W.; Gogotsi, Y. Intercalation and delamination of layered carbides and carbonitrides. *Nat Commun* **2013,** *4*, 1716, DOI: 10.1038/ncomms2664.

(91) Agresti, A.; Pazniak, A.; Pescetelli, S.; Di Vito, A.; Rossi, D.; Pecchia, A.; Auf der Maur, M.; Liedl, A.; Larciprete, R.; Kuznetsov, D. V.; Saranin, D.; Di Carlo, A. Titanium-carbide MXenes for work function and interface engineering in perovskite solar cells. *Nat Mater* **2019,** *18* (11), 1228-1234, DOI: 10.1038/s41563-019-0478-1.

(92) Melitz, W.; Shen, J.; Kummel, A. C.; Lee, S. Kelvin probe force microscopy and its application. *Surf. Sci. Rep.* **2011,** *66* (1), 1-27, DOI: 10.1016/j.surfrep.2010.10.001.

(93) Xu, X.; Wu, H.; He, X.; Hota, M. K.; Liu, Z.; Zhuo, S.; Kim, H.; Zhang, X.; Alshareef, H. N. Iontronics Using V2CTx MXene-Derived Metal-Organic Framework Solid Electrolytes. *ACS Nano* **2020,** *14* (8), 9840-9847, DOI: 10.1021/acsnano.0c02497.

(94) Tang, B.; Hussain, S.; Xu, R.; Cheng, Z.; Liao, J.; Chen, Q. Novel Type of Synaptic Transistors Based on a Ferroelectric Semiconductor Channel. *ACS Appl Mater Interfaces* **2020,** *12* (22), 24920-24928, DOI: 10.1021/acsami.9b23595.

(95) Kim, M. K.; Lee, J. S. Ferroelectric Analog Synaptic Transistors. *Nano Lett.* **2019,** *19* (3), 2044-2050, DOI: 10.1021/acs.nanolett.9b00180.

(96) Zhao, T.; Zhao, C.; Xu, W.; Liu, Y.; Gao, H.; Mitrovic, I. Z.; Lim, E. G.; Yang, L.; Zhao, C. Z. Bio-Inspired Photoelectric Artificial Synapse based on Two-Dimensional $Ti_3C_2T_x$ MXenes Floating Gate. *Adv. Funct. Mater.* **2021,** *31* (45), DOI: 10.1002/adfm.202106000.

(97) Chertopalov, S.; Mochalin, V. N. Environment-Sensitive Photoresponse of Spontaneously Partially Oxidized Ti3C2 MXene Thin Films. *ACS Nano* **2018,** *12* (6), 6109-6116, DOI: 10.1021/acsnano.8b02379.

(98) Xu, W.; Zheng, H.; Liu, Y.; Zhou, X.; Zhang, C.; Song, Y.; Deng, X.; Leung, M.; Yang, Z.; Xu, R. X.; Wang, Z. L.; Zeng, X. C.; Wang, Z. A droplet-based electricity generator with high instantaneous power density. *Nature* **2020,** *578* (7795), 392-396, DOI: 10.1038/s41586-020-1985-6.

(99) Shi, Q.; Zhang, Z.; He, T.; Sun, Z.; Wang, B.; Feng, Y.; Shan, X.; Salam, B.; Lee, C. Deep learning enabled smart mats as a scalable floor monitoring system. *Nat Commun* **2020,** *11* (1), 4609, DOI: 10.1038/s41467-020-18471-z.

(100) Park, S.; Parida, K.; Lee, P. S. Deformable and Transparent Ionic and Electronic Conductors for Soft Energy Devices. *Adv Energy Mater* **2017,** *7* (22), 1701369, DOI: 10.1002/aenm.201701369.

(101) Yang, Z.; Yang, Y.; Liu, F.; Wang, Z.; Li, Y.; Qiu, J.; Xiao, X.; Li, Z.; Lu, Y.; Ji, L.; Wang, Z. L.; Cheng, J. Power Backpack for Energy Harvesting and Reduced Load Impact. *ACS Nano* **2021,** *15* (2), 2611-2623, DOI: 10.1021/acsnano.0c07498.

(102) Wu, H.; Wang, S.; Wang, Z.; Zi, Y. Achieving ultrahigh instantaneous power density of 10 MW/m(2) by leveraging the opposite-charge-enhanced transistor-like triboelectric nanogenerator (OCT-TENG). *Nat Commun* **2021,** *12* (1), 5470, DOI: 10.1038/s41467-021-25753-7.

(103) Jacobs, H. O.; Whitesides, G. M. Submicrometer patterning of charge in thin-film electrets. *Science* **2001,** *291* (5509), 1763-6, DOI: 10.1126/science.1057061.

(104) Sakane, Y.; Suzuki, Y.; Kasagi, N. The development of a high-performance perfluorinated polymer electret and its application to micro power generation. *Journal of Micromechanics and Microengineering* **2008,** *18* (10), 104011, DOI: 10.1088/0960-1317/18/10/104011.

(105) Liu, Y.; Liu, W.; Wang, Z.; He, W.; Tang, Q.; Xi, Y.; Wang, X.; Guo, H.; Hu, C. Quantifying contact status and the air-breakdown model of charge-excitation triboelectric nanogenerators to maximize charge density. *Nat Commun* **2020,** *11* (1), 1599, DOI: 10.1038/s41467-020-15368-9.

(106) Liu, W.; Wang, Z.; Wang, G.; Liu, G.; Chen, J.; Pu, X.; Xi, Y.; Wang, X.; Guo, H.; Hu, C.; Wang, Z. L. Integrated charge excitation triboelectric nanogenerator. *Nat Commun* **2019,** *10* (1), 1426, DOI: 10.1038/s41467-019-09464-8.

(107) Wang, J.; Wu, H. Y.; Wang, Z.; He, W. C.; Shan, C. C.; Fu, S. K.; Du, Y.; Liu, H.; Hu, C. G. An Ultrafast Self-Polarization Effect in Barium Titanate Filled

Poly(Vinylidene Fluoride) Composite Film Enabled by Self-Charge Excitation Triboelectric Nanogenerator. *Adv. Funct. Mater.* **2022,** *32* (35), 2204322, DOI: 10.1002/adfm.202204322.

(108) Zi, Y.; Wu, C.; Ding, W.; Wang, Z. L. Maximized Effective Energy Output of Contact-Separation-Triggered Triboelectric Nanogenerators as Limited by Air Breakdown. *Adv. Funct. Mater.* **2017,** *27* (24), 1700049, DOI: 10.1002/adfm.201700049.

(109) Zhou, Y. S.; Liu, Y.; Zhu, G.; Lin, Z. H.; Pan, C.; Jing, Q.; Wang, Z. L. In situ quantitative study of nanoscale triboelectrification and patterning. *Nano Lett.* **2013,** *13* (6), 2771-6, DOI: 10.1021/nl401006x.

(110) Wu, C.; Kim, T. W.; Choi, H. Y. Reduced graphene-oxide acting as electron-trapping sites in the friction layer for giant triboelectric enhancement. *Nano Energy* **2017,** *32*, 542-550, DOI: 10.1016/j.nanoen.2016.12.035.

(111) Husain, E.; Nema, R. S. Analysis of Paschen Curves for air, N2 and SF6 Using the Townsend Breakdown Equation. *IEEE Transactions on Electrical Insulation* **1982,** *EI-17* (4), 350-353, DOI: 10.1109/tei.1982.298506.

(112) Burm, K. T. A. L. Calculation of the townsend discharge coefficients and the Paschen curve coefficients. *Contributions to Plasma Physics* **2007,** *47* (3), 177-182, DOI: 10.1002/ctpp.200710025.

(113) Walsh, R. Lifestyle and mental health. *Am Psychol* **2011,** *66* (7), 579-92, DOI: 10.1037/a0021769.

(114) Crimmins, E. M. Lifespan and Healthspan: Past, Present, and Promise. *Gerontologist* **2015,** *55* (6), 901-11, DOI: 10.1093/geront/gnv130.

(115) Tudor-Locke, C.; Bassett, D. R., Jr. How many steps/day are enough? Preliminary pedometer indices for public health. *Sports Med* **2004,** *34* (1), 1-8, DOI: 10.2165/00007256-200434010-00001.

(116) Bravata, D. M.; Smith-Spangler, C.; Sundaram, V.; Gienger, A. L.; Lin, N.; Lewis, R.; Stave, C. D.; Olkin, I.; Sirard, J. R. Using pedometers to increase physical activity

and improve health: a systematic review. *JAMA* **2007,** *298* (19), 2296-304, DOI: 10.1001/jama.298.19.2296.

(117) Crouter, S. E.; Schneider, P. L.; Karabulut, M.; Bassett, D. R., Jr. Validity of 10 electronic pedometers for measuring steps, distance, and energy cost. *Med Sci Sports Exerc* **2003,** *35* (8), 1455-60, DOI: 10.1249/01.MSS.0000078932.61440.A2.

(118) Moore, C. C.; McCullough, A. K.; Aguiar, E. J.; Ducharme, S. W.; Tudor-Locke, C. Toward Harmonized Treadmill-Based Validation of Step-Counting Wearable Technologies: A Scoping Review. *J Phys Act Health* **2020,** *17* (8), 1-13, DOI: 10.1123/jpah.2019-0205.

(119) Fan, F. R.; Tang, W.; Wang, Z. L. Flexible Nanogenerators for Energy Harvesting and Self-Powered Electronics. *Adv. Mater.* **2016,** *28* (22), 4283-305, DOI: 10.1002/adma.201504299.

(120) Zhang, Y.; Peng, M.; Liu, Y.; Zhang, T.; Zhu, Q.; Lei, H.; Liu, S.; Tao, Y.; Li, L.; Wen, Z.; Sun, X. Flexible Self-Powered Real-Time Ultraviolet Photodetector by Coupling Triboelectric and Photoelectric Effects. *ACS Appl Mater Interfaces* **2020,** *12* (17), 19384-19392, DOI: 10.1021/acsami.9b22572.

(121) Cheng, P.; Liu, Y. N.; Wen, Z.; Shao, H. Y.; Wei, A. M.; Xie, X. K.; Chen, C.; Yang, Y. Q.; Peng, M. F.; Zhuo, Q. Q.; Sun, X. H. Atmospheric pressure difference driven triboelectric nanogenerator for efficiently harvesting ocean wave energy. *Nano Energy* **2018,** *54*, 156-162, DOI: 10.1016/j.nanoen.2018.10.007.

(122) Zhu, X. X.; Meng, X. S.; Kuang, S. Y.; Di Wang, X.; Pan, C. F.; Zhu, G.; Wang, Z. L. Triboelectrification-enabled touch sensing for self-powered position mapping and dynamic tracking by a flexible and area-scalable sensor array. *Nano Energy* **2017,** *41*, 387-393, DOI: 10.1016/j.nanoen.2017.09.025.

(123) Song, W.; Gan, B.; Jiang, T.; Zhang, Y.; Yu, A.; Yuan, H.; Chen, N.; Sun, C.; Wang, Z. L. Nanopillar Arrayed Triboelectric Nanogenerator as a Self-Powered Sensitive Sensor for a Sleep Monitoring System. *ACS Nano* **2016,** *10* (8), 8097-103, DOI: 10.1021/acsnano.6b04344.

(124) Dong, K.; Deng, J.; Zi, Y.; Wang, Y. C.; Xu, C.; Zou, H.; Ding, W.; Dai, Y.; Gu, B.; Sun, B.; Wang, Z. L. 3D Orthogonal Woven Triboelectric Nanogenerator for Effective Biomechanical Energy Harvesting and as Self-Powered Active Motion Sensors. *Adv. Mater.* **2017,** *29* (38), DOI: 10.1002/adma.201702648.

(125) Lin, Z. M.; Wu, Z. Y.; Zhang, B. B.; Wang, Y. C.; Guo, H. Y.; Liu, G. L.; Chen, C. Y.; Chen, Y. L.; Yang, J.; Wang, Z. L. A Triboelectric Nanogenerator-Based Smart Insole for Multifunctional Gait Monitoring. *Advanced Materials Technologies* **2019,** *4* (2), DOI: 10.1002/admt.201800360.

(126) Deng, C. R.; Tang, W.; Liu, L.; Chen, B. D.; Li, M. C.; Wang, Z. L. Self -Powered Insole Plantar Pressure Mapping System. *Adv. Funct. Mater.* **2018,** *28* (29), 1801606, DOI: 10.1002/adfm.201801606.

(127) Zhu, M.; Shi, Q.; He, T.; Yi, Z.; Ma, Y.; Yang, B.; Chen, T.; Lee, C. Self-Powered and Self-Functional Cotton Sock Using Piezoelectric and Triboelectric Hybrid Mechanism for Healthcare and Sports Monitoring. *ACS Nano* **2019,** *13* (2), 1940-1952, DOI: 10.1021/acsnano.8b08329.

(128) Zeng, W.; Tao, X. M.; Chen, S.; Shang, S. M.; Chan, H. L. W.; Choy, S. H. Highly durable all-fiber nanogenerator for mechanical energy harvesting. *Energy & Environmental Science* **2013,** *6* (9), 2631-2638, DOI: 10.1039/c3ee41063c.

(129) Lee, K. Y.; Yoon, H. J.; Jiang, T.; Wen, X. N.; Seung, W.; Kim, S. W.; Wang, Z. L. Fully Packaged Self-Powered Triboelectric Pressure Sensor Using Hemispheres-Array. *Adv Energy Mater* **2016,** *6* (11), DOI: 10.1002/aenm.201502566.

(130) Rasel, M. S.; Maharjan, P.; Salauddin, M.; Rahman, M. T.; Cho, H. O.; Kim, J. W.; Park, J. Y. An impedance tunable and highly efficient triboelectric nanogenerator for large-scale, ultra-sensitive pressure sensing applications. *Nano Energy* **2018,** *49*, 603-613, DOI: 10.1016/j.nanoen.2018.04.060.

(131) Yang, Y.; Zhang, H.; Lin, Z. H.; Zhou, Y. S.; Jing, Q.; Su, Y.; Yang, J.; Chen, J.; Hu, C.; Wang, Z. L. Human skin based triboelectric nanogenerators for harvesting biomechanical energy and as self-powered active tactile sensor system. *ACS Nano* **2013,**

*7* (10), 9213-22, DOI: 10.1021/nn403838y.

(132) Guo, H.; Li, T.; Cao, X.; Xiong, J.; Jie, Y.; Willander, M.; Cao, X.; Wang, N.; Wang, Z. L. Self-Sterilized Flexible Single-Electrode Triboelectric Nanogenerator for Energy Harvesting and Dynamic Force Sensing. *ACS Nano* **2017,** *11* (1), 856-864, DOI: 10.1021/acsnano.6b07389.

(133) Chen, S. W.; Cao, X.; Wang, N.; Ma, L.; Zhu, H. R.; Willander, M.; Jie, Y.; Wang, Z. L. An Ultrathin Flexible Single-Electrode Triboelectric-Nanogenerator for Mechanical Energy Harvesting and Instantaneous Force Sensing. *Adv Energy Mater* **2017,** *7* (1), DOI: 10.1002/aenm.201601255.

(134) Wang, X.; Que, M.; Chen, M.; Han, X.; Li, X.; Pan, C.; Wang, Z. L. Full Dynamic-Range Pressure Sensor Matrix Based on Optical and Electrical Dual-Mode Sensing. *Adv. Mater.* **2017,** *29* (15), DOI: 10.1002/adma.201605817.

(135) Lin, Z. M.; Yang, J.; Li, X. S.; Wu, Y. F.; Wei, W.; Liu, J.; Chen, J.; Yang, J. Large-Scale and Washable Smart Textiles Based on Triboelectric Nanogenerator Arrays for Self-Powered Sleeping Monitoring. *Adv. Funct. Mater.* **2018,** *28* (1), DOI: 10.1002/adfm.201704112.

(136) Ha, M.; Lim, S.; Cho, S.; Lee, Y.; Na, S.; Baig, C.; Ko, H. Skin-Inspired Hierarchical Polymer Architectures with Gradient Stiffness for Spacer-Free, Ultrathin, and Highly Sensitive Triboelectric Sensors. *ACS Nano* **2018,** *12* (4), 3964-3974, DOI: 10.1021/acsnano.8b01557.

(137) Chen, S.; Wu, N.; Ma, L.; Lin, S.; Yuan, F.; Xu, Z.; Li, W.; Wang, B.; Zhou, J. Noncontact Heartbeat and Respiration Monitoring Based on a Hollow Microstructured Self-Powered Pressure Sensor. *ACS Appl Mater Interfaces* **2018,** *10* (4), 3660-3667, DOI: 10.1021/acsami.7b17723.

(138) Chen, S.; Zhuo, B.; Guo, X. Large Area One-Step Facile Processing of Microstructured Elastomeric Dielectric Film for High Sensitivity and Durable Sensing over Wide Pressure Range. *ACS Appl Mater Interfaces* **2016,** *8* (31), 20364-70, DOI: 10.1021/acsami.6b05177.

(139) Soin, N.; Shah, T. H.; Anand, S. C.; Geng, J. F.; Pornwannachai, W.; Mandal, P.; Reid, D.; Sharma, S.; Hadimani, R. L.; Bayramol, D. V.; Siores, E. Novel "3-D spacer" all fibre piezoelectric textiles for energy harvesting applications. *Energy & Environmental Science* **2014,** *7* (5), 1670-1679, DOI: 10.1039/c3ee43987a.

(140) Lai, Y. C.; Deng, J.; Zhang, S. L.; Niu, S.; Guo, H.; Wang, Z. L. Single-Thread-Based Wearable and Highly Stretchable Triboelectric Nanogenerators and Their Applications in Cloth-Based Self-Powered Human-Interactive and Biomedical Sensing. *Adv. Funct. Mater.* **2017,** *27* (1), 1604462, DOI: 10.1002/adfm.201604462.

(141) Wu, W.; Wen, X.; Wang, Z. L. Taxel-addressable matrix of vertical-nanowire piezotronic transistors for active and adaptive tactile imaging. *Science* **2013,** *340* (6135), 952-7, DOI: 10.1126/science.1234855.

(142) Zhang, Q.; Zhang, Z.; Liang, Q.; Shi, Q.; Zhu, M.; Lee, C. All in One, Self-Powered Bionic Artificial Nerve Based on a Triboelectric Nanogenerator. *Adv Sci (Weinh)* **2021,** *8* (12), 2004727, DOI: 10.1002/advs.202004727.

(143) Liu, M.; Pu, X.; Jiang, C.; Liu, T.; Huang, X.; Chen, L.; Du, C.; Sun, J.; Hu, W.; Wang, Z. L. Large-Area All-Textile Pressure Sensors for Monitoring Human Motion and Physiological Signals. *Adv. Mater.* **2017,** *29* (41), DOI: 10.1002/adma.201703700.

(144) Xie, L.; Chen, X.; Wen, Z.; Yang, Y.; Shi, J.; Chen, C.; Peng, M.; Liu, Y.; Sun, X. Spiral Steel Wire Based Fiber-Shaped Stretchable and Tailorable Triboelectric Nanogenerator for Wearable Power Source and Active Gesture Sensor. *Nanomicro Lett* **2019,** *11* (1), 39, DOI: 10.1007/s40820-019-0271-3.

(145) Singh, R.; Mehra, R. Qualitative Analysis of Darlington Feedback Amplifier at 45nm Technology. *Bulletin of Electrical Engineering and Informatics* **2018,** *7* (1), 21-27, DOI: 10.11591/eei.v7i1.750.

(146) Li, A.; Cui, M.; Shen, Y.; Li, Z. Q.; Liu, W.; Mitrovic, I. Z.; Wen, H. Q.; Zhao, C. Z. Monolithic Comparator and Sawtooth Generator of AlGaN/GaN MIS-HEMTs With Threshold Voltage Modulation for High-Temperature Applications. *Ieee Transactions on Electron Devices* **2021,** *68* (6), 2673-2679, DOI: 10.1109/Ted.2021.3075425.

(147) Xie, X. K.; Zhang, Y.; Chen, C.; Chen, X. P.; Yao, T.; Peng, M. F.; Chen, X. J.; Nie, B. Q.; Wen, Z.; Sun, X. H. Frequency-independent self-powered sensing based on capacitive impedance matching effect of triboelectric nanogenerator. *Nano Energy* **2019,** *65*, DOI: 10.1016/j.nanoen.2019.103984.

(148) Liu, Z. X.; Zhao, Z. Z.; Zeng, X. W.; Fu, X. L.; Hu, Y. Expandable microsphere-based triboelectric nanogenerators as ultrasensitive pressure sensors for respiratory and pulse monitoring. *Nano Energy* **2019,** *59*, 295-301, DOI: 10.1016/j.nanoen.2019.02.057.

(149) Liu, L.; Tang, W.; Deng, C. R.; Chen, B. D.; Han, K.; Zhong, W.; Wang, Z. L. Self-powered versatile shoes based on hybrid nanogenerators. *Nano Res* **2018,** *11* (8), 3972-3978, DOI: 10.1007/s12274-018-1978-z.